DISS. ETH NO. 28735

Low-temperature magneto-transport and X-ray metrology of ultra-thin group V doping layers in silicon: platforms for quantum science and technology

A thesis submitted to attain the degree of
DOCTOR OF SCIENCES of ETH ZURICH
(Dr. sc. ETH Zürich)

presented by
NICOLO D'ANNA
MSc ETH in Physics, ETH Zürich
born on 28.04.1992

accepted on the recommendation of
Prof. Dr. Gabriel A. Aeppli, examiner
Prof. Dr. Aharon Kapitulnik, co-examiner
Dr Giordano Scappucci, co-examiner
Dr Markus Müller, co-examiner

2022

Abstract

In 1947 the first field-effect-transistor was invented, since then the miniaturisation of semiconductor electronics has enabled the sustained exponential growth in the density of transistors in integrated circuits, know as Moore's law. The advent and refinement of the transistor is arguably one of, if not the most, important inventions of the past century. So far the challenges in reducing transistors' dimensions were mostly related to fabrication techniques, rather than fundamental physics. However, as the industrial transistors approach the atomic limit, with industrial designs at the 5 nm scale, quantum physical effects become dominant, making conventional electronics inadequate. Thus, it becomes indispensable to understand and take advantage of the quantum effects governing nano-scale electronics. This considerable task encompasses a wide variety of research directions, from developing quantum computing to discovering and understanding quantum effects in new low-dimensional materials (i.e. materials that are confined to less than three-dimensions). A central long-standing problem in the field of low-dimensional conductors is the metal-to-insulator transition (MIT). It was observed in a wide variety of materials, that are conductive at high carrier densities and insulating at low carrier densities (in the limit of 0 K). The existence and the understanding of such a transition in two-dimensional materials is the focus of many research centres and remains an open question.

The main focus of this work was on low-temperature magneto-transport experiments on novel two-dimensional (2D) arsenic-doped silicon δ-layers, which are proposed as a platform for silicon-based quantum technologies. The doping density was controlled to create a series of samples ranging from metallic to almost insulating, allowing for studies of the two-dimensional MIT in a highly disordered half-filling Hubbard model. Owing to the unprecedented thinness and low density of our arsenic δ-layers, we had access to an unexplored regime of strong electron-electron interaction in a highly disordered 2D electron liquid. We showed that the enhanced interaction strength reduces the weak-localisation effects typically observed in doped silicon δ-layers, and causes the Zeeman effect to become dominant in the low temperature magneto-transport. In light of these effects, we developed a procedure to distinguish the two effects, and to extract the relevant electron characteristics. Furthermore, we found that the low temperature phase in dilute dopant layers is that of an inhomogeneous conductor. This phase manifests anomalous transverse voltages V_{xy} with an even response to the applied magnetic field, and hysteresis in the longitudinal and transverse magneto-resistance. We argue that the inhomogeneous phase is characterised by percolation of insulating and conducting regions that can be tuned by a magnetic field, in which the current is forced into meandering conduction channels resulting in the observed anomalous transverse voltages V_{xy}. Moreover, we argue that the electron localisation length, responsible for the conductivity's temperature dependence, is cut-off by inelastic scattering in the insulating regions causing the conductivity to saturate at low temperatures; offering an explanation to the general inability to thermalise disordered 2D electron layers at low temperatures.

In order to confirm the structure of our samples we developed X-ray imaging methods and showed that they are non-destructive. Specifically, we used X-ray fluorescence to detect the position and element-species of the atoms in our samples, and verified with magneto-transport that the dopants' position remained unmoved within 0.2 Angstroms. To obtain the depth distribution and thickness of the buried dopant atom layers in silicon, we showed that resonant X-ray reflectometry measurement can be used for atom specific nanometer resolution depth measurements.

The findings of this research should stimulate further investigation of dilute-doping layers near the MIT in semiconductors to elucidate the exact mechanisms driving the inhomogeneous phase and its associated anomalous Hall effect and hysteresis.

Résumé

En 1947, le premier transistor à effet de champ a été inventé. Depuis lors, la miniaturisation de l'électronique a permis une croissance exponentielle de la densité des transistors dans les circuits intégrés, connue sous le nom de la loi de Moores. L'avènement et le perfectionnement du transistor peuvent être considérés comme l'une des inventions les plus importantes, voir la plus importante, du siècle dernier. Jusqu'à présent, les défis posés par la réduction de la taille des transistors étaient principalement liés aux techniques de fabrication, plutôt qu'à la physique fondamentale. Cependant, comme la taille des transistors industriels actuels se rapproche de la limite atomique, avec des transistor à l'échelle de 5 nm, les effets physiques quantiques deviennent dominants, rendant l'électronique conventionnelle inadéquate. Il devient donc indispensable de comprendre et de tirer parti des effets quantiques qui régissent l'électronique à l'échelle nanométrique. Cette tâche considérable englobe une grande variété de directions de recherche, allant du développement des technologies quantiques à la découverte et à la compréhension des effets quantiques dans les nouveaux matériaux de basse dimensionnalité (c'est-à-dire des matériaux qui sont confinés à moins de trois dimensions). Un problème central de longue date pour les conducteurs de basse dimensionnalité est la transition métal-isolant (TMI). Elle a été observée dans une grande variété de matériaux, qui sont conducteurs à des densités de porteurs de charge élevées et isolants à de faibles densités de porteurs de charges (dans la limite de 0 K). L'existence et la compréhension d'une telle transition dans les matériaux bidimensionnels sont un sujet de recherche principal dans de nombreux centres et restent une question ouverte.

L'objectif principal de ce travail est de réaliser des expériences de magnéto-transport à basse température sur de nouvelles couches bidimensionnelles (2D) de silicium dopé à l'arsenic, qui sont considérées comme une plateforme prometteuse pour les technologies quantiques dans les semi-conducteurs. La densité de dopage a été contrôlée pour créer une série d'échantillons allant de métallique à presque isolant, ce qui a permis d'étudier la TIM à deux dimensions dans un modèle de Hubbard bidimensionnel à demi-remplissage et désordonné. Grâce à la minceur et à la basse densité sans précédent de nos couches d'arsenic, nous avons eu accès à un régime inexploré de forte interaction électron-électron dans un liquide de Fermi 2D hautement désordonné. Nous avons montré que la force d'interaction accrue réduit les effets de localisation faible typiquement observés dans les couches de silicium dopées et que l'effet Zeeman devient dominant dans le magnéto-transport à basse température. À la lumière de ces effets, nous avons développé une procédure permettant de distinguer les deux effets et d'extraire les caractéristiques électroniques pertinentes. En outre, nous avons découvert que la phase à basse température associée aux couches de dopants à basse densitée est celle d'un conducteur inhomogène. Cette phase manifeste des tensions transversales V_{xy} anomales avec une réponse isotrope au champ magnétique appliqué, et une hystérèse dans la magnétorésistance longitudinale et transversale. Nous soutenons que la phase inhomogène est celle d'une percolation de régions

isolantes et conductrices qui peuvent être contrôlées par un champ magnétique, dans laquelle le courant est forcé dans des canaux de conduction sinueux, ce qui cause les tensions transversales V_{xy} anomales observées. De plus, nous soutenons que la longueur de localisation des électrons, qui est responsable de la dépendance de la conductivité vis-à-vis de la température, est limitée par les chocs inélastique sur les régions isolantes, ce qui entraîne la saturation de la conductivité à basse température. Cet effet explique l'incapacité générale à thermaliser les couches électroniques 2D désordonnées à basse température.

Afin de confirmer les dimensions structurelles de nos échantillons, nous avons développé des méthodes d'imagerie par rayons X et montré qu'elles sont non destructives. En particulier, nous avons utilisé la spectrométrie de fluorescence des rayons X pour détecter la position et l'espèce chimique atomique des atomes dans nos échantillons, et nous avons vérifié par magnéto-transport que la position des dopants n'a pas bougé de plus que 0.2 Angström. Afin d'obtenir la distribution et l'épaisseur des couches d'atomes de dopants dans le silicium, nous avons en outre montré que la réflectométrie résonnante des rayons X peut être utilisée afin de mesurer la distribution verticale d'une espèce chimique atomique choisit avec une résolution nanométrique.

Les résultats de cette travail devraient stimuler la poursuite de la recherche sur les couches à basse densité de dopage proche de la TIM dans les semi-conducteurs, afin d'élucider les mécanismes exacts à l'origine de la phase inhomogène et de l'effet Hall anomal et de l'hystérèse qui lui sont associés.

Contents

1 Introduction

The main objective of this PhD thesis is to study two-dimensional dopants layers in silicon and particularly to study the consequences of replacing the commonly used phosphorus dopant by arsenic. Greater precision is obtained in the fabrication of donor devices with arsenic, as explained in section 3, motivating the project to use arsenic donors to define quantum devices in silicon. Additionally, the two-dimensional arsenic layers used in this work are thinner than their phosphorus counterparts and more dilute than previously fabricated dopant layers in silicon, motivating the study of the two-dimensional metal-to-insulator transition in our arsenic layers. It is natural to start by fabricating and characterising two-dimensional arsenic δ-doped layers in silicon and compare their low-temperature electronic characteristics to phosphorus δ-layers. As a consequence of having access to the thinner and more dilute dopant layers, we observed unexpected physics near the MIT in an otherwise well-studied system.

The layout of this thesis is the following: we start with an introduction to the physics of two-dimensional conductors, followed by an introduction to silicon δ-doped samples in section 3, then by a section about X-ray imaging of the dopants in our samples in section 4, and finally by a section about the magneto-transport measurements of the electrons in the dopant layers in section 5.

2 Physics of two-dimensional disordered conductors

2.1 Localisation in two-dimensional disordered conductors

In the classical Drude model, when an electric field is applied on a disordered conductor, the electrons undergo diffusive motion. The assumption is that the electrons do not interact with each other and are only deviated on scattering centres, resulting in a random walk. The mean distance between scattering centres is noted as L and corresponds to the electron's mean free path. In this picture the mean displacement of the electrons under an electric field is given by the normalised sum of all the possible electron trajectories and results in the well know Drude formula for the conductivity:

$$\sigma_D = \frac{ne^2L}{vm} \tag{1}$$

Where n is the electron density, e is the electron charge, v is the velocity of the electrons and m is the electron mass. The assumptions of the Drude model are reasonable for Fermi gases at high temperatures. A Fermi gas is a system of non-interacting fermions, as can be the case for high density electron gases where interactions can be neglected due to the screening effect. The quantum physical treatment of the diffusive motion of the electrons requires to sum the quantum amplitudes of the electron paths rather than the probabilities. Because of the wave-like nature of the electrons, all different possible paths interfere with each other. In particular an electron's trajectory that forms a closed loop, as shown in figure 1, results in the constructive interference at the origin of the loop of the two counter-propagating paths around the loop, if the system has time reversal symmetry. Because the interference at the origin of a loop is constructive, the probability to find the electron there is increased: the electron is said to be localised. This localisation effect leads to a quantum correction to the classical Drude formula. Exact calculation of all the interferences in the random walk is not tractable making the localisation problem notoriously difficult.

In order for localisation effects to be visible two ingredients are necessary: the number of looped trajectories within all the possible trajectories must be large and the mean distance between inelastic scattering events L_ϕ (L_ϕ is the electron coherence length) must be at least as long as the loops. The first ingredient is an intrinsic property of the material, related to the disorder strength, however it can be greatly enhanced by making the conductor two-dimensional, because it reduces the number of possible trajectories but not the number of looped trajectories. The second ingredient, the electron coherence length L_ϕ, is strongly temperature dependent and enhanced at very low temperatures. For these reasons weak-

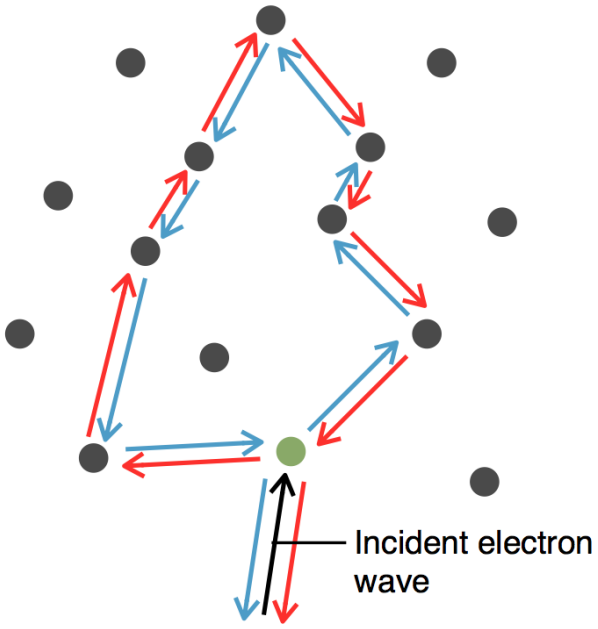

Figure 1: **Electron localisation.** Illustration of a single electron localisation in the diffusive regime. The arrows indicate possible paths taken by the electron and the dots are scattering centres. The red arrows show a clockwise looped trajectory originating on the scattering centre in green, the blue arrows show the same trajectory but with an anti-clockwise direction. Both path interfere constructively resulting in an increased probability for the electron to be at the green scattering centre.

localisation effects were first observed in the 70s in 2D conductive layers in silicon MOSFETs [2, 3]. The two main visible signatures of localisation in a conductor are the temperature dependence of the conductivity, through the temperature dependence of L_ϕ, and a strong response of the conductivity to magnetic fields. The presence of a magnetic field perpendicular to the loops's plane breaks the time reversal symmetry necessary for the constructive interferences to arise, thus delocalising the electrons. The exact description and mechanism governing the localisation of electrons in 2D conductive layers depends on various parameters, such as disorder strength, interaction strength, electron density, electron mobility and spin-orbit coupling.

In 1958, for the first time, Anderson proposed the concept of localisation [4], for which he later won the Nobel prize. He predicted that in the presence of strong disorder, large potential barriers form, and non-interacting electrons that can only tunnel between neighbouring local minima become completely localised, turning a conductor into an insulator. The effect is known as Anderson localisation. However, at non-zero temperatures, tunnelling between localised sites in a highly disordered system can be assisted via thermally excited lattice phonons [5], such

that the conductivity has a stretched exponential dependence on the temperature, known as the variable range hoping regime.

In intermediate disorder systems, the electrons are usually said to be weakly localised. Weak-localisation (WL) is considered to be the precursor to Anderson localisation and does not result in a total halt of the electrons. In this case, the interference effects are usually strong enough that they result in detectable temperature and magnetic field dependences, but weak enough that they can be described perturbatively as a quantum correction to the Drude model.

In 1980, Hikami, Larkin and Nagaoka (HLN) [6] derived the first successful equation to describe the effect of temperature and magnetic fields on 2D weakly localised electron systems. In their theory the effect of weak spin-orbit-interactions and magnetic scattering by impurity spins are described in random potential scattering in 2D, by the one-loop perturbation in $k_F L$ and the renormalisation group method (k_F is the fermi wave-vector and L the mean free path). The weak-localisation correction to the Drude conductivity calculated by HLN in a magnetic field $B_\perp$ perpendicular to the conduction layer and a temperature T is

$$\Delta\sigma_{WL}(B_\perp) = \left(\frac{e^2}{2\pi^2\hbar}\right)\left[\psi\left(\frac{1}{2}+\frac{\hbar}{4eL_\phi^2 B_\perp}\right) - \psi\left(\frac{1}{2}+\frac{\hbar}{2eL^2 B_\perp}\right) + \ln\left(\frac{2L_\phi^2}{L^2}\right)\right], \tag{2}$$

where $\hbar$ is the reduced Planck constant, e the electron charge, $\psi(x)$ is the digamma function, and L_ϕ is the coherence length. L_ϕ is the only temperature dependent parameter in the HLN model. If the main source of phase breaking processes is inelastic electron-electron interactions, as is the case in phosphorus δ-layers [7], it is expected to be a power law of the temperature, $L_\phi \propto T^\alpha$ with α = -0.5 [8].

The last term of the HLN equation (2) is field independent, and shows that in weakly-localised systems the temperature dependence of the conductivity is logarithmic. The HLN equation is accepted as being the correct physical description for many 2D systems, including 2D dopant δ-layers in silicon [9] and germanium [10], silicon MOSFETs [11], and silicon quantum wells [12]. However, it is only valid under the condition that $k_F L \ll 1$, *i.e.*, that the localisation is not strong. Note that in 2D, $k_F = \sqrt{2\pi n}$ which is close to the inverse of the average distance between donors $d_n = 1/\sqrt{n}$, such that $k_F L$ is a measure of the ratio between the electron mean free path and the mean distance between donors. If $d_n < L$ the electrons will be strongly localised on the donors.

There are a number of proposed localisation types, depending on sample characteristics. An example of a phase diagram for the 2D quantum wells in GaAs/ $In_xGa_{1-x}As$/ GaAs structures from [13] is shown in figure 2, where the coherence

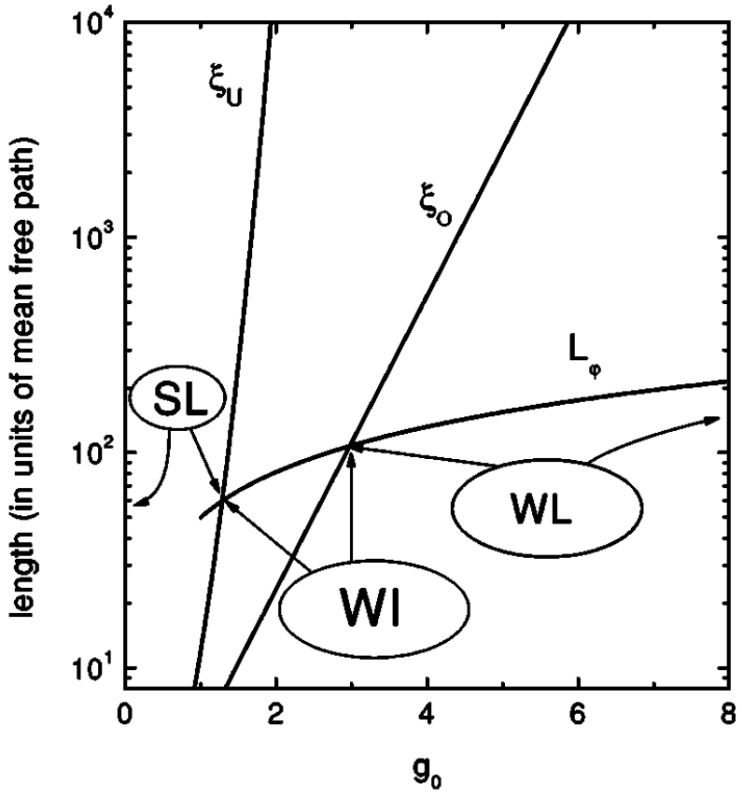

Figure 2: **Theoretical phase diagram of the 2D metallic phase.** Phase diagram for a 2D electron gas in GaAs/InxGa1-xAs/GaAs single quantum well structures from [13]. The electrons can be weakly localised (WL), weakly interacting (WI), or strongly localised (SL), depending on the dimensionless conductance $g_0 = k_F L$, where k_F is the Fermi wavevector and L the electron mean free path. The lines show the coherence length L_ϕ and the localisation length ξ_O and ξ_U of the disordered Hamiltonian in the orthogonal and unitary symmetry respectively.

length L_ϕ and the localisation length ξ (typical length of a looped trajectory) were calculated. The dimensionless conductance $g_0 = k_F L$ is tuning the type of electron transport (with $k_F \propto \sqrt{n}$ the Fermi wavevector, and L the electron mean free path). At low density (low g_0), the length ξ is much smaller than L_ϕ, such that all loops interfere constructively, the electrons are strongly localised (SL) and believed to be in the hopping regime. At high density (high g_0), ξ is larger than L_ϕ, such that only the smaller than average loops can interfere constructively, the electrons are in the weakly localised (WL) regime well described by HLN theory and equation (2). At intermediate density the electrons are weakly interacting (WI) and the transport is poorly understood. The example in figure 2 considers the quantum corrections to the conductivity due to electron self-interference and the mutual effect of WL and Coulomb interactions, it neglects other effects such as spin-orbit coupling and strong interactions that can be present in other materials.

Based on the HLN weak-localisation calculation, additional effects were taken into account. Notably, in the presence of strong spin-orbit coupling, the effect of closed loop trajectories can be reversed: as the electron travels around a loop, it can undergo spin-orbit scattering events which will rotate the spin by the same amount in the opposite direction for electrons traveling in opposite directions. Thus, it can happen that at the origin of a loop the interference is negative, such that the electron is delocalised, the effect is called weak-anti-localisation [6]. The effect always comes in combination with conventional weak-localisation, because only in large loops are there enough spin-orbit scattering events to create the negative interference, while the smaller loops still interfere constructively. Weak-anti-localisation can be observed as a small positive magneto-resistance in many materials, such as $In_xGa_{1-x}As$ quantum wells [14], InAs quantum structures [15], GaAs inversion layers [16], ultrathin topological insulators [17] and graphene [18], however it has never been observed in phosphorus δ-layers in silicon or germanium. In 2D layers, if the confinement potential is asymmetric, a net spin-orbit interaction ensues. The effect is known as the Rashba effect, it also results in weak-anti-localisation [19]. Similarly the lack of an inversion centre in the crystal structure also leads to spin-orbit interactions, through the Dresselhaus effect [20]. The effect of spin-orbit interactions stemming from both the Rashba effect and the Dresselhaus effect was taken into account by Iordanskii, Lyanda-Geller, and Pikus (ILP), who developed a successful extension of the HLN model [21]. The ILP model takes into account spin-orbit interactions through the spin-orbit length, L_{so}, representing the mean length for the spin to relax, and is given by

$$\Delta\sigma_{ILP}(B) = \frac{e^2}{4\pi^2\hbar}\left\{\frac{1}{a_0} + \frac{2a_0 + 1 + H_{so}/B}{a_1(a_0 + H_{so}/B) - 2H_{so}/B} + 2\ln\left(\frac{H_0}{B}\right) + \psi\left(\frac{1}{2} + \frac{H_\phi}{B}\right) + 3C - \sum_{n=1}^{\inf}\left[\frac{3}{n} - \frac{3a_n^2 + 2a_n(H_{so}/B) - 1 - 2(2n+1)(H_{so}/B)}{[a_n + H_{so}/B]a_{n-1}a_{n+1} - 2H_{so}/B[(2n+1)a_n - 1]}\right]\right\}, \quad (3)$$

where $a_n = n + \frac{1}{2} + \frac{H_\phi}{B} + \frac{H_{so}}{B}$ and H_ϕ, H_{so}, and H_0 are the characteristic fields of the coherence time, spin-orbit time, and the mean free time respectively. The ILP model is used for example to describe the magneto-resistance of InSb quantum wells [22], Oxide Interfaces [23], and silicon-germanium quantum wells [24].

The above mentioned HLN and ILP models are derived for weak electron-electron interactions, and as such they are well suited to describe dense 2D electron layers where electrons experience only a short-range screened Coulomb interaction.

2.2 Electron-electron interactions in two-dimensional conductors

The addition of electron-electron interactions to the 2D localisation problem can generally be described by the Hubbard model [25]. It is a general Hamiltonian describing interacting particles in a lattice. The particles can hop in-between lattice sites, experience Coulomb interaction on the sites, and if screening is weak they can experience electron-electron interactions with all (or only the n nearest neighbours) other electrons, as shown on figure 3. Thus, the Hamiltonian 4 has a kinetic hopping term t, an on-site interaction term U, and an electron-electron interaction term J. The inclusion of the interaction term J is considered as an extension to the 2D Hubbard model. The Hubbard Hamiltonian is given by

$$\hat{H} = -t \sum_{i,\sigma} \left(\hat{c}^{\dagger}_{i,\sigma} \hat{c}_{i+1,\sigma} + \hat{c}^{\dagger}_{i+1,\sigma} \hat{c}_{i,\sigma} \right) + U \sum_{i} \hat{n}_{i\uparrow} \hat{n}_{i\downarrow} + \sum_{i \neq j} J_{ij} \hat{n}_i \hat{n}_j, \tag{4}$$

where $\hat{n}_{i,\sigma} = \hat{c}^{\dagger}_{i,\sigma} \hat{c}_{i,\sigma}$ is the spin-density operator for a spin σ on the site i, and $\hat{n_i} = \hat{n_{i\uparrow}} + \hat{n_{i\downarrow}}$ is the density operator. For electrons U is the electron repulsion and it is positive.

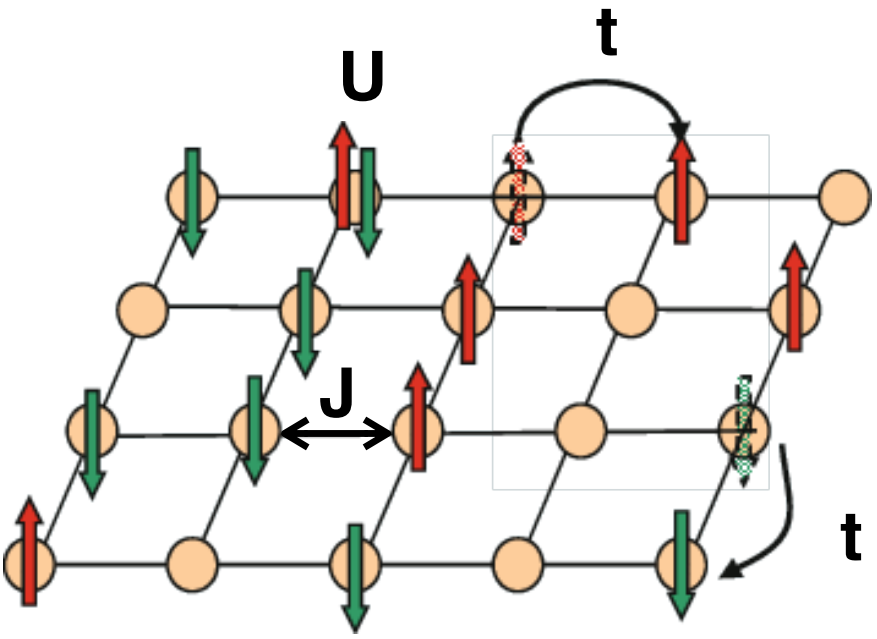

Figure 3: **2D Hubbard model.** Sketch from Wikipedia of the 2D Hubbard model. Electrons on the same site experience Coulomb repulsion U, and need an hopping energy t to tunnel to a neighbouring site. The interaction between neighbouring electrons is J.

The Hubbard model is used to describe any system of particles in a periodic potential. In the case that there is disorder, the hopping energy t will depend

on the site, as the tunnelling barriers will differ in size. If the model is considered for dimensions greater than 1, it cannot be efficiently simulated numerically. Many different calculation methods have been used and lead to contradicting results [26]. However, calculations agree that there is a rich phase diagram associated with the 2D Hubbard model, for example it can predict the Mott insulator transition, where at low electron density, strong repulsion between electrons leads to an insulating state [27, 28]. The Hubbard model is considered of particular interest, because it is believed to describe the physics of high temperature superconductivity of cuprates. A proposed solution to calculate the properties of the 2D Hubbard model is to use quantum simulation, where the idea is to obtain the phase diagram of a specific Hubbard Hamiltonian by precise engineering, control, and measurement of a 2D system. Such quantum simulation schemes are currently pursued with trapped atoms [29] and with donors in silicon [30].

In 1982 Lee and Ramakrishnan calculated the first order of the dynamically screened Coulomb interaction effect on the conductivity of a magnetic field coupling to electron spins in 2D [31]. In the presence of a magnetic field B, the spin-up and spin-down energy bands are split by $g\mu_B B$ by the Zeeman effect, where $g \approx 2$ is the g factor, μ_B is the Bohr magneton and B the magnetic field. The energy gap reduces the interaction between electrons of opposite spins, resulting in the change in conductivity calculated by Lee and Ramakrishnan:

$$\begin{aligned} \Delta\sigma_Z(h) &= -\frac{e^2}{\hbar}\frac{F}{4\pi^2}\ln\left(\frac{h}{1.3}\right), \text{ for } h \gg 1 \\ \Delta\sigma_Z(h) &= -\frac{e^2}{\hbar}\frac{F}{4\pi^2}0.084h^2, \text{ for } h \ll 1 \end{aligned} \tag{5}$$

where $h = \frac{g\mu_B B}{k_B T}$ is the reduced field and F is a constant between 0 and 1. The constant F is the averaged Coulomb interaction, which gives the strength of the Zeeman effect, as such it is large when the electron density and screening are low. The calculated effect scales as $\ln(B/T)$, meaning that it becomes strong for low temperatures. Such scaling with the reduced field $h \propto B/T$ of the magneto-conductance was seen in In-Ga-Zn oxide films [32], at surface of hydrogen-terminated diamond [33], and in high-mobility silicon MOSFETs [34], for a magnetic field parallel to the 2D layer. The Zeeman effect is isotropic in field in the limit that spin-orbit interaction is weak. Nonetheless, it is mostly observed in planar fields, because in perpendicular fields it tends to be dominated by the effect of localisation breaking.

Electron-electron interactions also lead to a logarithmic temperature dependent correction to the Drude conductivity in the absence of magnetic field [35], similarly to the weak localisation effect. In most systems with electron-electron interactions, the correction to the conductivity is due to both the interaction and the weak localisation effects, such that the temperature dependence in the

absence of magnetic field is given by [13]

$$\delta\sigma_0 = \frac{e^2}{2\pi^2\hbar}\ln\frac{\tau}{\tau_\phi} + \frac{e^2}{2\pi^2\hbar}\kappa_{ee}\ln T, \tag{6}$$

where τ is the mean free time, τ_ϕ the coherence time, and $\kappa_{ee} = 1 - F/2$ is the electron-electron interaction strength. The first term in equation (6) comes from the magnetic field independent term in the HLN weak-localisation correction in equation (2), and the second term is due to the electron-electron interactions. Both terms give a logarithmic temperature dependence of the conductivity. In the case that the coherence time has the temperature dependence T^{-1} as is the case in silicon δ-layers [36], equation (6) takes the from $\delta\sigma_0 = G_0(1 + \kappa_{ee})\ln T$, such that it is straightforward to extract the interaction parameter F from the conductivity's temperature dependence.

In addition, the interaction effect leads to a changed Hall factor [35, 37],

$$\delta R_H/R_H = 2\delta R_{ee}/R, \tag{7}$$

where δR_H and δR_{ee} are the change in the Hall factor and the longitudinal resistance from the high temperature value before localisation effects become important. In this case, δR_{ee} only includes the interaction part proportional to κ_{ee} of equation (6) and excludes the weak-localisation contribution. This effect was first observed in silicon inversion layers [38].

2.3 Two-dimensional metal-to-insulator transition

In 1979, Abrahams, Anderson, Licciardello, and Ramakrishnan, theoretically predicted that in the absence of electron-electron interactions, all two-dimensional systems with any amount of disorder necessarily had to be insulating because of localisation effects [39], *i.e.*, the resistivity of all 2D systems becomes infinitely large as the temperature goes to 0 K. This was commonly accepted until the mid 90s, when novel 2D systems were discovered that had a resistance that diminished with decreasing temperatures [40]. The systems were ultrahigh-mobility MOSFETs, with mobilities up 7.1×10^4 cm^2/Vs. Figure 4 shows the first evidence of a metallic phase in a 2D system, where the main plot is the scaled temperature dependence of the sample's resistivity, with the scaling parameter T_0 plotted in the inset. Such a scaling behaviour was argued to be indicative of a phase transition, in agreement with the zero field mobility edge predicted by Azbel [41]. In their work [40], samples with higher disorder (and lower mobility) never became conductive, already indicating the important role of order in the MIT. Since then it was found that 2D systems with strong correlations between carriers tend to be metallic when the free carrier density is high enough. These systems all exhibit a

similar metal-to-insulator transition (MIT) behaviour from high density metal to low density insulator. The MIT is observed in a wide range of materials, including graphene [42], Van der Walls heterostructures [43], SiGe heterostructures [44], GaAs/AlGaAs heterostructures [45], AlAs heterostructures [46], ZnO-related heterostructures [47], WTe_2 monolayers [48] and more. However the mechanisms that drive the transition and the respective phases remain poorly understood.

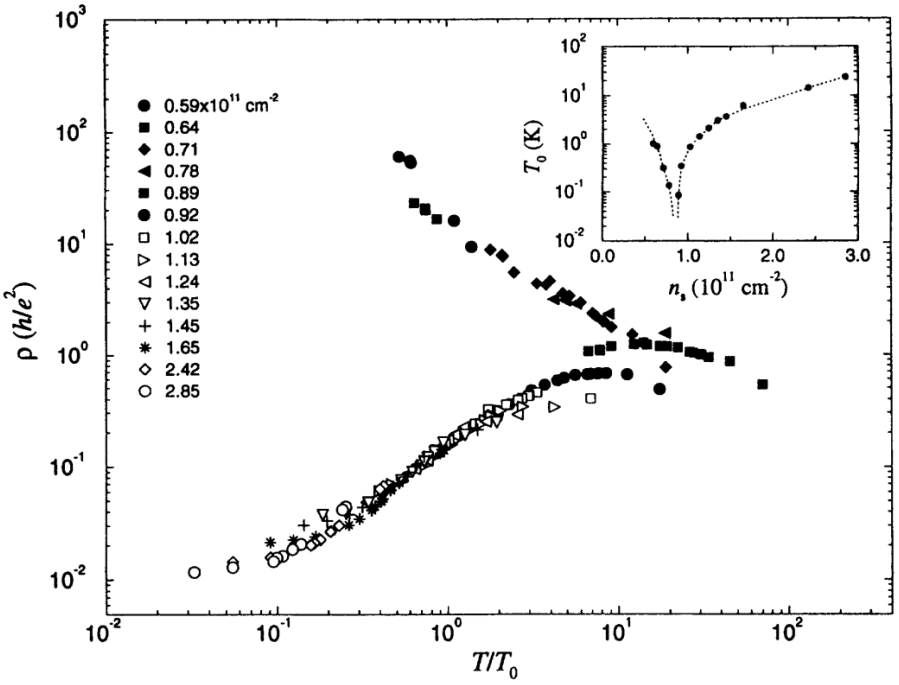

Figure 4: **First observation of the 2D MIT.** Data from [40] showing the 2D MIT in silicon MOSFET devices. The plot shows the temperature dependence of the resistivity in the absence of a magnetic field. For densities above 0.89×10^{11} cm^{-2} the samples are conducting. The resistivity for all densities scales as T/T_0 with T_0 shown in the inset.

In silicon there are multiple ways of creating 2D electron gases. Two systems that have been extensively studied are silicon MOSFETs and silicon quantum wells. In these systems many parameters are different, while the electron confinement is typically of the order of 10 nm in quantum wells and in MOSFETs, the disorder is lower and the electron mobility can be 100 times larger in quantum wells. Nonetheless, the MIT is observed under similar interaction parameter strength $r_s \approx 20$, defined as the ratio of the Coulomb energy and the Fermi energy ($r_s = g_v/(\pi n_s)^{1/2} a_B$, where n_s is the electron density, a_B the effective Bohr radius and g_v the valley degeneracy) [49]. The critical electron density n_c at which the system stops being metallic can differ by orders of magnitude depending on the system.

The critical density n_c associated with the MIT in a material can be increased

by applying an external magnetic field. A typical example of the effect of a magnetic field is shown in figure 5, where measurements of the temperature dependence of the resistivity for the same ultralow-disorder SiGe/Si/SiGe quantum well are shown in the absence of a magnetic field (5a), and in the presence of a spin polarising planar magnetic field B* (5b). In this example the disorder is very low and the change in conductivity between the insulator and conductor is more than six orders of magnitude. Polarising the electron spin with a field B^* shifts the critical transition density from $n_c(B=0) = 0.88\times10^{10}$ cm^{-2} to $n_c(B^*) = 1.11\times10^{10}$ cm^{-2}. It is argued that spins in a single-valley 2D system should become insulating when fully polarised by an external field, because the metallic phase is linked to the spin and valley degrees of freedom of the electrons [50,51]. In 2D silicon the electron energy spectrum has two degenerate valleys, such that the metallic state can exist for spinless electrons as is shown in figure 5b. However, if disorder is strong, strong inter-valley scattering results in an effective single valley at low temperatures. The effect of such inter-valley scattering can be seen in Si MOSFETs, where disorder is higher than in ultra-clean SiGe/Si/SiGe quantum well and polarising the electrons always results in an insulating state [52].

To determine the critical transition density n_c different criteria exist. The most directly visible criterion is to define n_c to be the density at which the derivative of the resistivity's temperature dependence $d\rho/dT$ changes sign. However the temperature derivative criterion can be ill defined because of non-monotonic dependences near the MIT, as is visible in figure 5a, and it can be argued that it is not certain that the dependence would remain monotonic to the limit of 0 K.

Alternatively, n_c can be determined by looking at the non-linear I-V characteristics on the insulating side of the transition: in the insulating phase a sufficiently high voltage allows electrons at the Fermi level to reach the mobility edge, resulting in the breakdown of the insulating phase, as is visible in figure 6 in the top inset. The breakdown threshold voltage V_{th} becomes smaller when the sample is less insulating and extrapolates to zero at n_c, as seen in the plotted red dots in figure 6. This criterion is temperature independent such that the value obtained for n_c should be valid at 0 K.

On the insulating side of the transition, the resistivity of ultra-clean quantum wells has an activated form, evidenced in an $1/T$ Arrhenius plot in the bottom inset of figure 6, in which the offset corresponds to the activation energy Δ. The activation energy has an electron density dependence shown on the main plot of figure 6, where the blue data are the activation energy Δ as a function of the density. At n_c Δ becomes zero, naturally leading to the metallic phase. Both criteria shown in figure 6 lead to the same critical density n_c and agree with the derivative criterion in the absence of magnetic field. This has been observed in ultra-clean SiGe/Si/SiGe quantum well and in more disordered silicon MOSFETs

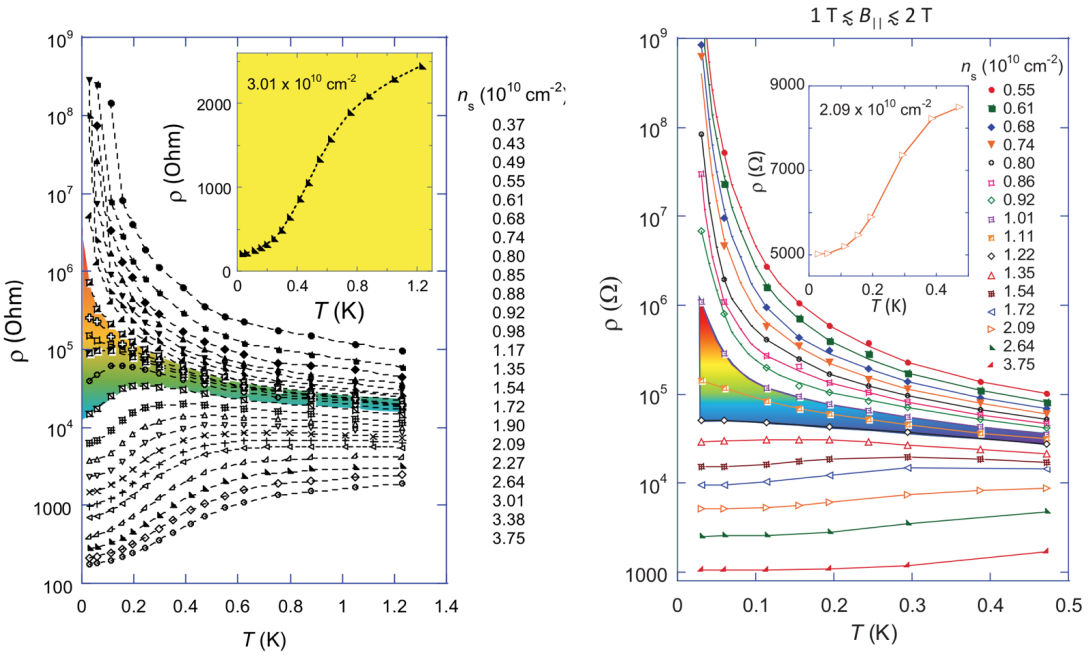

(a) (b)

Figure 5: **MIT in ultra-low disorder electron layers.** Temperature dependence of the resistivity of an ultra-low disorder SiGe/Si/SiGe quantum well from [53]. Each curve is at a different electron density n_s marked on the right. The coloured region indicates the region at the MIT where the temperature dependence is non-monotonic. The data in (a) is taken with no magnetic field and the inset is a close up of the curve at $n_s = 3.01 \times 10^{10}$ cm^{-2}, showing a resistivity drop of a factor 12. The critical density is n_c(B=0) = 0.88×10^{10} cm^{-2}. The data in (b) is taken with a field B^* sufficiently strong to polarise the electron spins and the insets is a close up of the curve at $n_s = 2.09 \times 10^{10}$ cm^{-2}, showing a resistivity drop of a factor 2. The critical density is n_c(B*) = 1.11×10^{10} cm^{-2}.

[52]. However in the case that the electrons in a silicon MOSFET are polarised by a magnetic field, the activation energy and the breakdown voltage give the same n_c and associated MIT, while the derivative criterion determines all densities to be insulating. Because of this discrepancy it is not clear whether 2D metals exist for spinless electrons in a single valley (high disorder). In dopant δ-layers in silicon, disorder is much larger and the derivative criterion always determines the samples to be insulating, and no activation energy can be determined because the weak-localisation effect gives a logarithmic temperature dependence to the resistivity. However, in sufficiently dense silicon δ-layers the I-V characteristics are found to be linear, an observation which is taken as an indication of the metallic phase.

There are good explanations for the temperature dependences of the metallic phase of various systems, depending on their disorder strength. The metallic be-

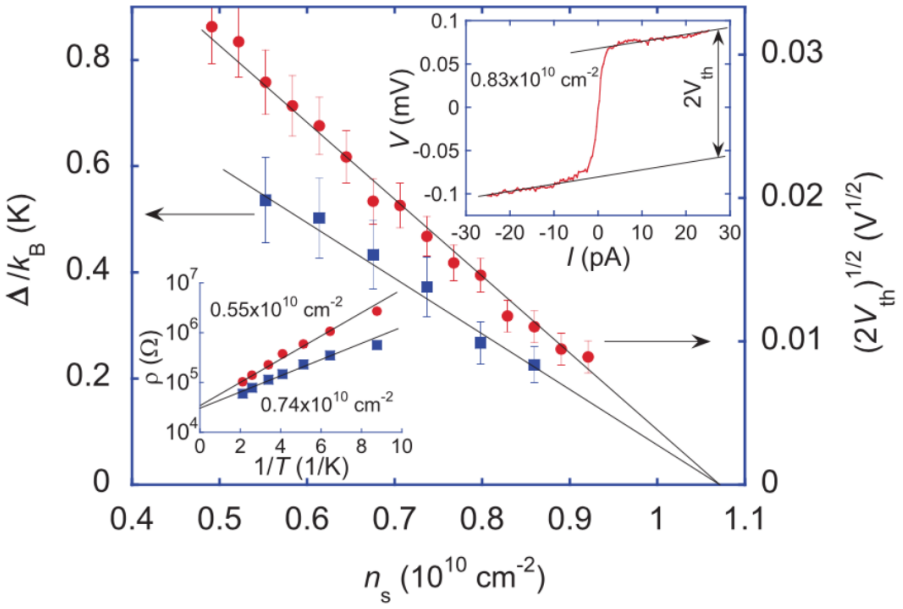

Figure 6: **Activation energy and non-linear I-V density dependence in an ultra-clean electron layer.** Data from the ultra-clean SiGe/Si/SiGe quantum wells in [49]. Determination of the critical density n_c by two methods. The red circles in the main panel are the threshold voltage V_{th} (shown in the top inset) as a function of density. The blue squares are the activation energy Δ as a function of the density, obtained from Arrhenius plots of the temperature dependence of the resistivity shown in the bottom inset. The extrapolation to zero activation energy and threshold voltage give n_c.

haviour in the clean systems can be described by coherent scattering of ballistic electrons by Friedel oscillations [54], while in the disordered systems the diffusive electrons are analysed by an interplay of strong interaction and disorder [50]. In both cases a spin-polarising magnetic field diminishes the interaction effect, resulting in an increased localisation and in a giant positive magneto-resistance. However there is no consensus on the MIT itself and whether it is driven by the same mechanism for clean and disordered systems [55]. There is a density range for which the phase is not well defined. It is shown for the ultra-clean case on figure 5 (coloured area): at high densities the sample is metallic and the resistivity drops monotonically with lowering temperature (a factor 12 drop for the highest density is seen in the inset), at low densities the sample is insulating and the resistivity increases monotonically, at intermediate densities the temperature dependence of the resistivity is non-monotonic indicating an ill defined phase in the MIT. In ultra-clean samples, it has recently been suggested that the cross-over phase is a quantum Wigner crystal [49], *i.e.*, the interaction between electrons forms a periodic crystal-like structure. However, such a Wigner crystal is not possible for high disorder systems and a number of hypotheses exist such

as Efros–Shklovskii variable range hopping [56], strong localisation crossover [57], or percolation [58].

Another problem that lacks an adequate explanation is the saturation of the conductivity at low temperatures. In most cases, there is an apparent "freezing" of the conduction parameters at hundreds of milli-kelvin temperatures [12,59–63]. The simplest explanation for the saturation would be that the system is not thermalising below the saturation temperature, *i.e.*, its temperature is not the same as measured on a nearby thermometer. However, if the systems are believed to be well thermalised, then there is no consensus on the physical effect leading to a conductivity saturation [64].

In order to understand the 2D MIT, extensive calculation of Hubbard models has been undertaken, with results highlighting the wealth of possible 2D phases around the transition.

2.4 Phase diagram at the 2D metal-to-insulator transition

In very low disorder 2D systems, it is likely that the insulating phase near the MIT is that of a lightly pinned electron crystal. In the case of the ultra-clean SiGe/Si/SiGe quantum wells from [49], the depinning of a Wigner crystal is deduced from the observation of two threshold voltages V_{th1} and V_{th2} in the V-I characteristics, visible in figure 7. Initially, a small voltage has no effect, the state is an insulator, then at the voltage V_{th1} the electron crystal starts unpinning at some pinning centres, resulting in a small noisy thermally activated current $I \propto \exp(-U(V)/k_B T)$, where $U(V)$ is the activation energy . At a higher voltage V_{th2}, all pinning centres of the crystal unpin, the crystal moves with friction and the current is a linear function of the voltage. Thus, the insulating phase near the MIT might be a Wigner crystal for ultra-clean systems. For systems with higher disorder an electron crystal would not be able to unpin, leaving the question of whether near the MIT there are different phases depending on disorder strength, or if another explanation is needed. Systems with only electronic repulsion might experience the Mott-Hubbard MIT, while disordered noninteracting systems might have a MIT driven by Anderson localisation, the phases related to both types of systems would most likely be different. While the Mott-Hubbard MIT is caused by electronic repulsion, the Anderson MIT is due to coherent backscattering of noninteracting particles from randomly distributed impurities.

The phase diagram at the MIT is considered to entail many quantum phases. Figure 8a shows a sketch of a proposed density-disorder phase diagram [65]. At very high disorder, electrons are strongly localised (Anderson localisation) such that the system is always an insulator. For low disorder, at high interaction

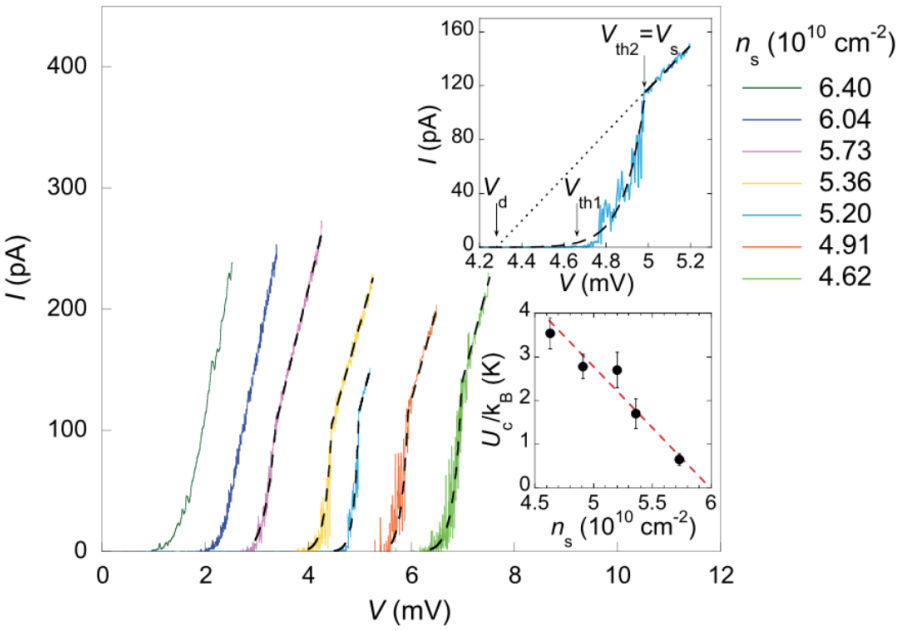

Figure 7: **Unpinning of a Wigner crystal in an ultra-clean 2D electron layer.** Data from the ultra-clean SiGe/Si/SiGe quantum wells in [49]. V-I characteristics in the insulating phase. Two threshold voltages are visible V_{th1} when a current appears and V_{th2} when the response becomes linear. The top inset shows a close up of a V-I curve. The bottom inset shows the density dependence of the activation energy.

strength $r_s \approx 35$ (low density) a Wigner crystal can be expected, as already predicted in 1989 for two-dimensional electron gases by Monte Carlo simulations [66]. At slightly lower r_s the electrons can form a strongly correlated ferromagnetic Fermi liquid (FFL) [67], before reaching a paramagnetic Fermi liquid phase at high densities (low r_s).

The phases of a 2D electron system are influenced by the temperature and external magnetic fields. Figure 8b shows the phase diagram in the density n_s and temperature T or magnetic field B plane for Si-MOSFETs [68]. The phase diagram is derived from measuring low-frequency resistance noise as a function of density, field, and temperature [69]. The measurements show that the electron dynamics is suddenly slowed down upon heating the electrons or polarising the electron spins with a planar magnetic field. The change happens at densities n_g slightly above the critical MIT density n_c, indicating an intermediate metallic glass phase or amorphous metal (yellow region in figure 8b) between the metallic (white region) and insulating (yellow region) phase. The width of the density interval in which the metallic glass phase exists is dependent on the disorder: in strongly disordered samples the density range can be large such that $(n_g - n_c)/n_c \approx 0.5$ [70], while in clean samples it can be as low as $(n_g - n_c)/n_c \approx 0.01$

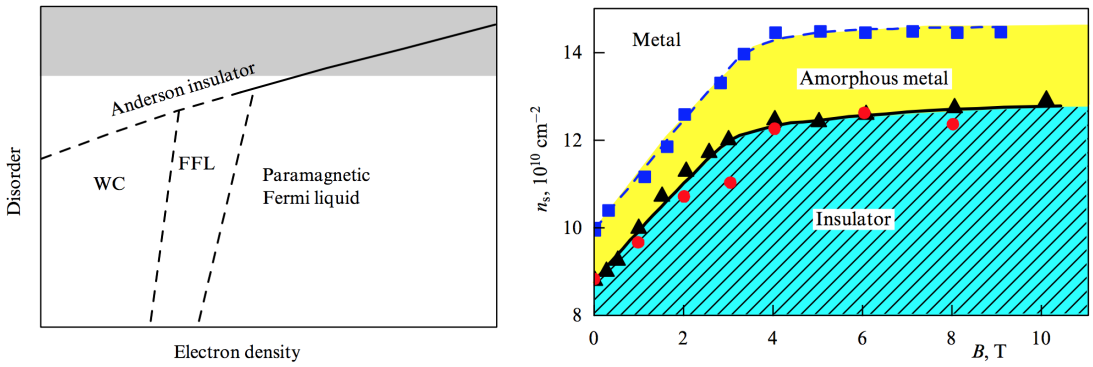

(a) (b)

Figure 8: **Examples of proposed MIT phase diagrams.** (a) Schematic disorder-vs-density phase diagram from [65] showing an Anderson insulator at high disorder, Wigner crystal (WC), ferromagnetic Fermi liquid (FFL) and paramagnetic Fermi liquid at lower disorder. The high-disorder region is shaded. (b) Density n_s-temperature T- magnetic field B phase diagram in Si-MOSFETs from [68]. The blue square are the measured boundary between the metallic (white region) and amorphous (yellow region) phase, the red dots and black triangles are the measured boundary between the amorphous and insulating (blue region) phase.

[71]. An important observation is that the amorphous metal is present in high and low magnetic fields, indicating that it is not due to the spins which are polarised, but to the electron-electron interactions.

Of particular interest to this work is the half-filled Hubbard model, because it describes the physics of group V substitutional dopants in silicon. As mentioned earlier, the model is intractable and different techniques to calculate the phase diagrams of the Hamiltonian lead to different and sometimes contradicting results [26]. The results of a dynamical mean-field theory calculation using geometrically averaged typical local density of states [72] are shown in figure 9a, in a $U - \Delta$ phase diagram, where U is the on-site interaction strength and Δ is a measure of the disorder strength. The calculations show a rich phase diagram. At low disorder Δ there is a transition from a metallic state to an interaction driven Mott insulator state (Mott-Hubbard MIT). The transition happens at a different U depending whether it is approached from the metallic side (circles in figure 9a) or from the insulating side (full dots): it is hysteretic and entails a coexistence regime. For large interactions U (low densities), increasing the disorder Δ changes continuously the Mott insulator into a strong disorder driven Anderson insulator, while for low interactions U the metallic state becomes strongly localised by increasing the disorder Δ (Anderson MIT). At intermediate interaction strength U and disorder Δ, the transition is less clear, in particular there can be a crossover

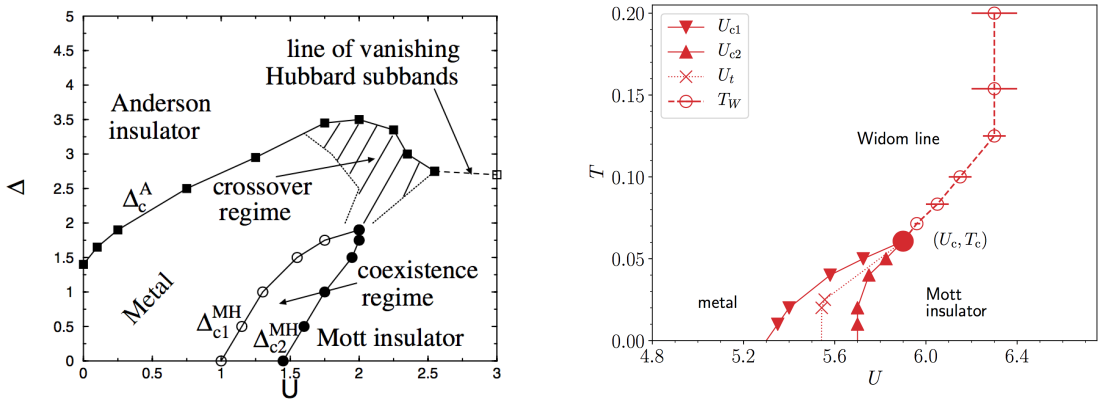

(a) (b)

Figure 9: **2D half-filled Hubbard models phase diagrams.** (a) Phase diagram from [72], calculated for a 2D half-filled Hubbard model with disorder strength Δ and interaction strength U. Squares indicate the Anderson MIT and circles indicate the Mott-Hubbard MIT for U increasing (open circles) and decreasing (full circles). (b) Thermodynamic phase diagram of the ordered 2D half-filled Hubbard model from [73]. Lines with full triangles mark the spinodal lines U_{c1} and U_{c2}, indicating the boundary of the insulating and metallic phase, respectively. The dotted line with crosses indicates the thermodynamic transition. The coexistence disappears at the Mott endpoint (full circle). The dashed line with open circles marks the Widom line, at which the phase changes continuously.

regime from metallic to insulating upon increasing U.

A study from 2019 derived the temperature interaction strength $T - U$ phase diagram for the half-filled 2D Hubbard model in the absence of disorder [73], based on thermodynamic calculations of the charge compressibility, entropy S, kinetic energy, potential energy, and free energy. The resulting phase diagram is shown in figure 9b. It qualitatively agrees with the phase diagram on figure 9a, in that a Mott-Hubbard MIT is predicted (though at a very different U). Close to the MIT the entropy of the metallic phase is found to be higher than that of the insulating phase, because in the Mott insulator there is less double occupancy of lattice sites. A higher entropy S results in a lower energy and thus a favourable state, as can be seen from the Helmholtz free energy $F = U - TS$ (where U is the internal energy). At low temperatures, the difference in entropy results in the hysteretic behaviour visible in figure 9b, where the downwards pointing triangle indicate the transition U_{c1} coming from high U and the upwards pointing triangles the transition U_{c2} coming from low U. The hysteresis shows that it is a first-order transition, with an increasingly small coexistence region as the temperature is increased. In fact, at high temperatures the entropy of both systems becomes dominated by thermal fluctuation rather than interaction effects. At a critical

temperature T_c there is an interaction strength U_c termed critical Mott endpoint (full circle), where the transition (triangles) becomes a crossover (open circles) following the Widom line (line of maximum correlation length starting at the Mott endpoint).

Altogether it can be said that, despite intense research and progress since the 50s, the 2D Hubbard model and the MIT in 2D materials remains one of the important questions of modern condensed matter physics. Progress in the field is made excruciatingly slow by the wealth of possible physical effects, the inability to perform their exact calculation, and the experimental difficulties linked to measuring 2D systems at extremely low temperatures: most studies are based on non-local conductivity measurements in electric and magnetic fields, giving a limited amount of information on the exact nature of the phases. In order to speed up the research on 2D materials, it will be important to create and utilise new experimental techniques, such as for example low temperature microwave-impedance microscopy (MIM) [74], and to develop quantum computing and simulation to solve the 2D Hubbard models. The motivations for tackling these difficult challenges go beyond curiosity for fundamental physics; the foreseen applications range from faster, more energy-efficient memory [75, 76], and computing [77], to enhanced sensitivity in sensing [78].

2D system	L [nm]	L_ϕ [nm]	$n_s \times 10^{14}$ [cm^{-2}]	d [nm]	r_s
Current work	3	70	0.12-1.9	0.4-1.5	0.8-3
Ge:P δ-layers [36]	20	400	0.3-1.4	1.49	0.2-0.6
Si MOSFET [11]	48	252	0.4-0.8$\times 10^{-4}$	10	10-20
QW 2DHG [65]	26	61	0.4-3.8$\times 10^{-4}$	0.5	10-20
Graphene [79]	50	900	0.005	0.5-1	$\sim$ 6-30

Table 1: **Characteristics of various 2D electron gases.** The systems in bold are half-filled. L is the mean free path, L_ϕ is the coherence length, n_s is the 2D sheet electron density, d is the electron layer thickness and r_s the interaction strength.

Here, we study the 2D MIT in arsenic-doped δ-layers (described in more details in section 3). Table 1 shows examples of typical parameters of 2D electron gases exhibiting the MIT. As can be seen in the table, our arsenic doped δ-layers have very different characteristics to other 2D systems, specifically they are highly disordered half-filled 2D systems with a large interaction parameter r_s. Note that systems with larger r_s have low disorder, are not half-filled, and have been extensively studied. The variation of the interaction parameter r_s in single layer graphene comes from the uncertainty on the Bohr radius which can vary from 0.5 nm to 2.5 nm depending on the substrate [80]. The δ-layers in germanium have similar characteristics to our δ-layers in silicon and are also half-filled, however

their interaction parameter is three times lower because the Bohr radius of the donor electrons is three times lagrer in germanium than in silicon. Thus, the samples used in this work represent a unique opportunity to investigate the MIT in a highly disordered, dilute, and thin 2D system with relatively strong electron-electron interactions.

3 Silicon δ-doped samples

The scope of this thesis is to investigate the physics of 2D group V δ-doped silicon, with a view towards quantum computing and low-dimensional electronics, by means of low-temperature magneto-transport experiments and X-ray imaging techniques. The research project is made particularly relevant by the fact that the samples are unique in three ways: it is the first time that arsenic δ-layers are studied electrically, the doping layer thicknesses have unprecedented thinness, and layers with unprecedented low densities are fabricated. The lower densities cause electron-electron interactions to be stronger, resulting in the observation of non-conventional effects in silicon, namely an anomalous transverse voltage, hysteresis, and inhomogeneous conduction.

3.1 Fabrication

The samples used for this work on the 2D MIT are fabricated at the London Centre for Nanotechnology (LCN), at University College London (UCL), by the groups led by Prof. Neil Curson and Prof. Steven Schofield. The samples are fabricated by gas-phase dosing of hydrogen passivated silicon, much like phosphorus δ-layers are fabricated [81, 82]. The fabrication process is illustrated in figure 10.

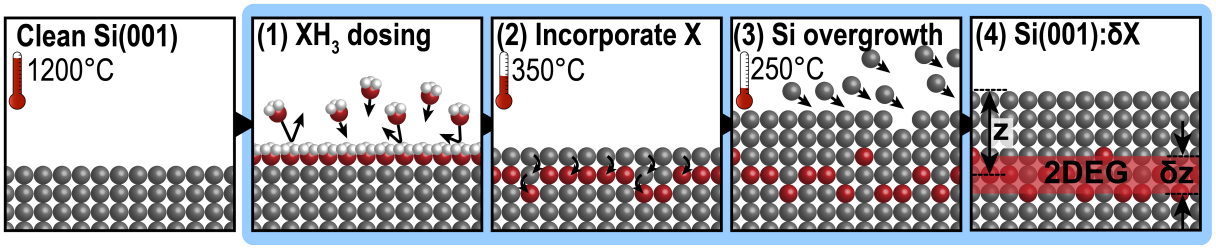

Figure 10: **Schematic illustration of arsenic δ-layer fabrication.** From left to right: flash annealing leaves the surface atomically flat, (1) AsH_3 gas forms a monolayer on the silicon surface, (2) annealing at 350 °C lets the arsenic migrate into the silicon, (3) epitaxial silicon is grown in the surface, (4) the final result is a 2D layer of dopants buried under the silicon. These schematics were made by Procopios Constantinou.

For the fabrication process, Si(001) wafers with a bulk arsenic doping density of 3×10^{14} cm^{-3} (resistivity >15 Ω cm) are used. After ultrasonically cleaning the samples, they are set in ultra-high vacuum and let to degas at 600 °C. The light background doping enables the passage of a current for flash annealing at 1200 °C by Joule heating. The purpose of the flash annealing in vacuum is to remove any surface contamination and let the silicon arrange in an atomically flat surface, as is illustrated in figure 10 on the leftmost panel. The subsequent step is to

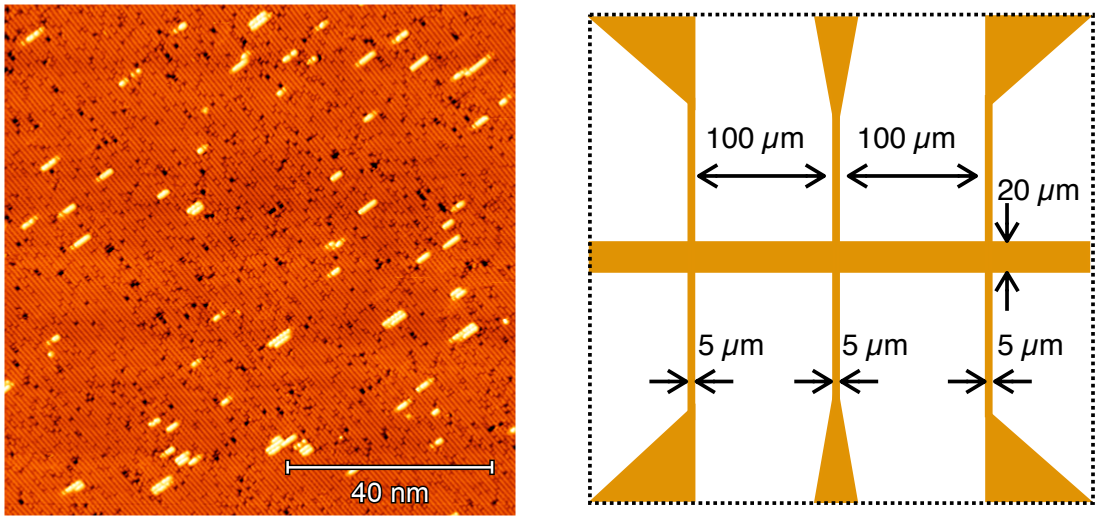

(a) (b)

Figure 11: **Arsenic Hall bar samples.** (a) STM height map of the sample's surface after arsenic incorporation, for an arsenic density n=1×10^{13} cm^2. The bright dots are silicon atoms ejected to the surface by arsenic atoms penetrating into the silicon. The image was taken by Procopios Constantinou. (b) Schematic of the Hall-bar dimensions. The orange represents the doped region. There are 8 contacts.

expose the clean silicon surface to AsH_3 gas. The gas forms a monolayer on the surface, as visible in figure 10 in image (1), and heating at 350 °C for 2 minutes makes the arsenic diffuse into the silicon (figure 10, image (2)). The amount of arsenic in the sample is controlled by choosing the total dose of AsH_3 gas. The incorporation of an arsenic atoms leads to the ejection to the surface of a silicon atom, such that, at this stage, a scanning tunnelling microscope (STM) can be used to estimate the amount of arsenic incorporated into the silicon. Figure 11a) shows an example of an STM height map, where the bright dots are dimers of silicon that were ejected to the surface. The number of dimers on the surface gives the incorporated arsenic density. Thereafter, 2 nm of silicon are deposited on the surface without heating. The function of these 2 nm of silicon, called locking-layer, is to avoid unwanted arsenic diffusion in the next annealing steps. The arsenic atoms initially find themselves in interstitial positions, where their donor electron does not contribute to the conduction band, they are not active. To activate the donors the sample is heated to 500 °C for 15 seconds, so that the atoms can move to find their energetically-favourable substitutional position, where they are active [82, 83]. Thanks to the locking-layer excessive spreading of the atoms towards the surface is avoided. Finally, epitaxial silicon overgrowth at 250 °C is used to obtain the buried active 2D layer of dopants in silicon (figure 10, image (3) and (4)).

For the magneto-conductance experiments, the fabricated samples were etched into Hall bars using optical lithography and reactive ion etching. The dimensions of the Hall-bars are shown in figure 11b, where the orange represents the arsenic-doped region. The Hall bars are 200 by 20 μm^2. Ohmic contacts were established by deposition of aluminium or palladium into arrays of etched holes extending through the δ-layer [84]. Each global δ-layer was etched into two identical Hall-bars, and a region was left unetched to be used for secondary ion mass spectroscopy (SIMS) measurements. Each Hall-bar was mounted on a chip carrier, and electrically connected to the carrier by aluminium wire bonds.

The change from phosphorus to arsenic dopants does not alter the fabrication procedure, except that the diffusion during steps 2 and 3 in figure 10 is reduced, because of the larger size and mass of arsenic compared to phosphorus, resulting in better-confined dopant layers. In bulk-doped silicon the electrons occupy one energy level scattered across the six degenerate silicon valleys. Vertical confinement of the dopants in δ-doped silicon causes the valleys to split into two types of multiply quantised sub-bands: the valleys in the k_x and k_y directions, and second with the two valleys in the k_z direction, where the electrons in samples with higher P or As densities occupy the 1Γ and 2Γ states, as shown by angle-resolved photon-emission spectroscopy in section 5.2.1. Thus the electron in thinner δ-layers have three distinct "flavours", with distinct effective masses.

3.2 Physical characteristics and dimensionality

The 2D electron gases created by sharp group V dopant layers have the particularity that the number of free electrons is simply given be the number of substitional donors, as each donor gives one electron to the conduction band. This is in contrast to many 2D electron layers, that are formed in inversion layers or trapping potential, where the number of free electrons usually depends on some gating potential.

Each donor electron is initially bound to its dopant atom. Figure 12 shows a sketch of the situation in a perfectly ordered 1D chain of donors in silicon: from top to bottom the dopant density is increased, with each arsenic atom being represented by an orange dot and the 1s orbital of its outermost electron is represented by the black circle. A sketch of the trapping potential $v(r)$ across the 1D chain is show in black for each density. The extent of the 1s orbital is 2.125 nm for a single arsenic donors in silicon [85], and the distance d between donors in a 2D layer is given by the inverse of the square root of the density ($d_{2D} = \sqrt{n^{-1}}$). In the top sketch, the dopant density is low, there is no overlap of the electron orbitals and no conduction band is formed, such that each electron is bound to the arsenic atom. In this case conduction could only happen by

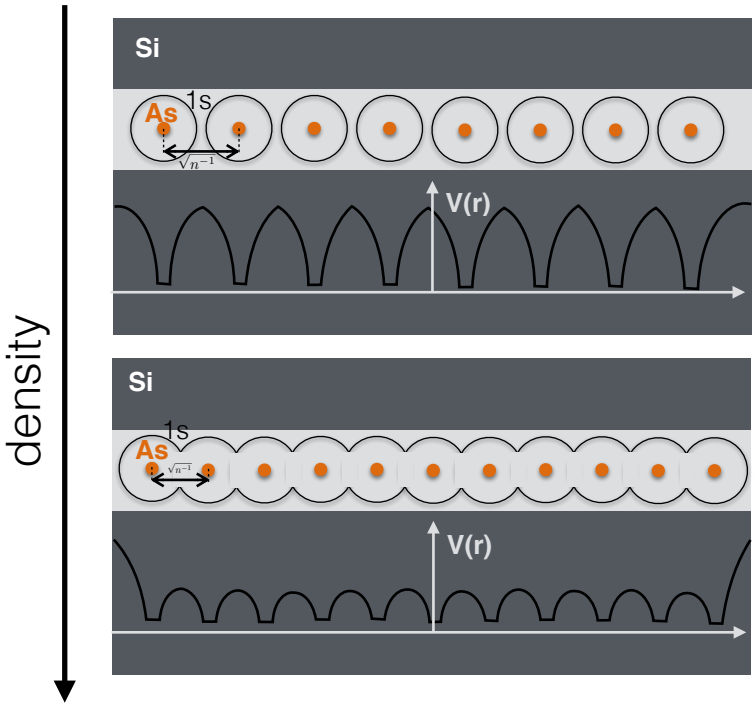

Figure 12: **Ordered donor chain.** Sketch of the arsenic donors (orange dots) and their outer electrons' 1s orbitals in silicon, for two different densities of an ordered 1D chain. $v(r)$ is the potential along the 1D chain.

thermally assisted hopping or tunnelling from one site to the other through the large potential barriers: the layer is an insulator. In the middle sketch, the density is large enough for a continuous conduction band to form, however, the electrons are still more likely to be found near the dopant atom, and the hopping energy t required for an electron to move from one site to another is such that upon cooling the electrons might become strongly bound to the dopants and the layer will become insulating. In the bottom sketch, the density is very high, such that the conduction band has only very small potential barriers between sites, allowing the electrons to move almost freely from a donor to another: the layer is metallic. An important point to this simplified image of the conduction in a dopant layer is that the electrons are always more likely to be found near the dopant trapping potential, and there are always two important parameters to describe the electron inter-site motion: the hopping energy t that depends on the potential barrier between dopant atoms, and the Coulomb repulsion U experienced when two electrons are on the same dopant. In essence, the electrons in an ordered 2D array of group V donors in silicon realise a perfect simulation of a 2D Hubbard model, given by the Hamiltonian (4), and illustrated in figure 3. Each donor contributes one electron and can host a maximum of two electrons, because of Pauli's exclusion principle, hence the Hubbard model is exactly half-

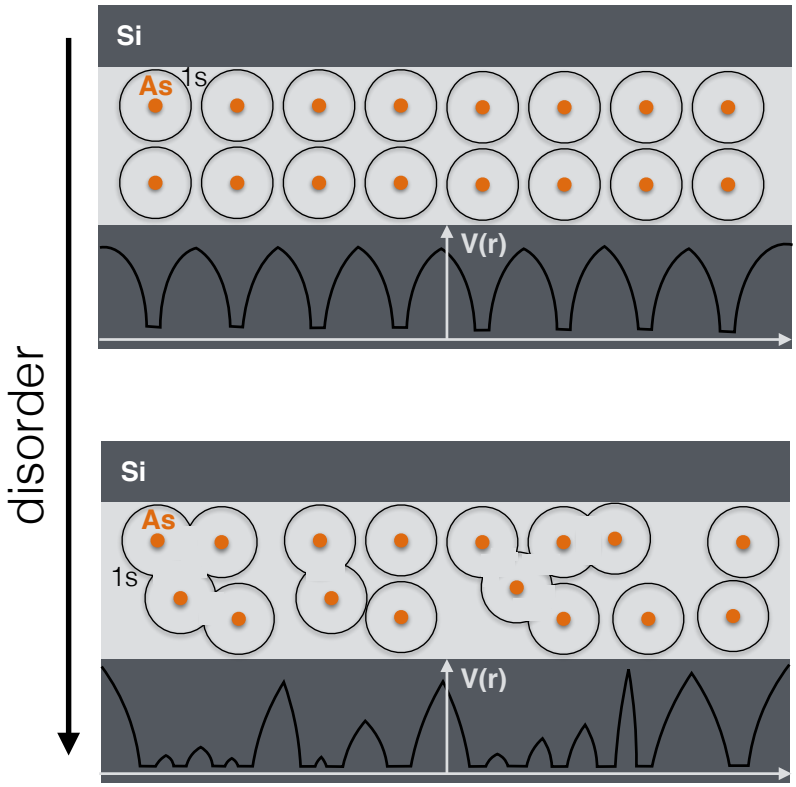

Figure 13: **Disorder in a 2D donor layer.** Sketch of the arsenic donors' electrons 1s orbitals in silicon for two different disorder strength of a 2D donor array with a fixed density. $v(r)$ is the potential along the sample.

filled. Note that in this simple picture the density required for the 1s orbitals to overlap is n $\approx 2.2\times10^{13}$ cm^{-2}, very close to the critical density n$_c$ $= 1\times10^{13}$ cm^{-2} calculated by Hwang and Das Sarma [86] for phosphorus donors.

In silicon δ-layers there is a large amount of disorder, because of the random nature of doping by exposure to a precursor gas (illustrated in figure 10). The effect of disorder is illustrated for two chains of 1D arsenic atoms in figure 13, where the effect of increasing disorder at a fixed density is shown from top to bottom. The top sketch shows an ordered insulator, in which the electron orbital do not overlap. The bottom sketch shows the situation where, for the same density, disorder creates conducting islands separated by potential barriers. Depending on the exact configuration of the disorder, the conductivity might be increased, because fewer tunnelling events are required for an electron to move across the sample. The Hamiltonian associated to such a disordered system will still be a Hubbard Hamiltonian, similar to equation (4), but now the hopping energy t is different between each site, making the simulation of such a system even more challenging. In the case of very strong disorder, the electrons are not able to hop from an island to another, they are in the strong Anderson localisation regime.

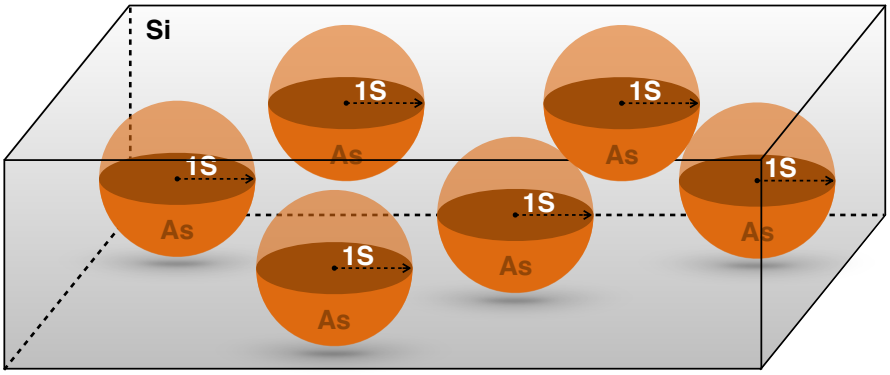

Figure 14: **Arsenic donors in a quasi-2D layer.** Representation of the arsenic atoms in the silicon with disorder in the plane and perpendicularly to the plane.

Currently it is not possible to fabricate dopant layers in silicon that are restricted to a single crystal plane, because of the diffusion of the dopant atoms during the necessary annealing steps shown in figure 10. The thinnest arsenic δ-layer measured to date has a thickness equivalent to three crystal planes, *i.e.*, $\sim$0.4 nm. The result is that there is both disorder in the δ-layer's plane and in the vertical plane, as illustrated in figure 14. The vertical disorder results in a finite thickness of the layer, and a reduction of the effective density. If the vertical spread of the dopants is larger than the electron orbitals, the layer starts to be 3D or quasi-2D instead of 2D, and the mean distance between donors becomes larger ($d_{3D} = n_{3D}^{-1/3}$ instead of $d_{2D} = n_{2D}^{-1/2}$). For arsenic and phosphorus donors in silicon, this limit is at the 1s orbital extent of $\approx$ 2 nm. The δ-layer samples studied here have a thickness lower than 1 nm, making them 2D materials on the scale of the electron orbitals.

3.3 Localisation in phosphorus δ-doped samples

Phosphorus δ-layers have been the subject of many low temperature magneto-transport studies. While in 2018 their thickness determined by magneto-resistance was around 10 nm [59], in 2020 it was already as small as 1.3 nm [87]. In this work, the thinnest phosphorus δ-layer was 1.3 nm thick, and the thinnest arsenic δ-layer was considerably thinner at 0.4 nm, corresponding to the thickness of only

three Si(100) crystal planes.

There is a general agreement that the low-temperature conductivity of phosphorus δ-layers with a doping density close to the MIT is dominated by the electrons' weak localisation, as is highlighted by the conductivity being a logarithmic function of the temperature (equation (6)), and the positive magneto-conductance being well fitted to the usual weak-localisation equations (13) [59, 87, 88]. It has to be pointed out that as the δ-layers become thinner and less dense, the weak-localisation fits become less good, and often a free global pre-factor to the whole equation (13) has to be used to obtain satisfying fits [36]. In addition, for thin and dilute layers, the magneto-conductance for planar magnetic fields has a negative part to it [36, 88] that cannot be described by weak-localisation, and is due to the Zeeman effect, as we show in section 5.2.2.

The electron mean free path L and coherence length L_ϕ are typically of the order 10 nm and 100 nm, respectively, implying that in terms of the observed localisation effects the samples can be considered 2D already at 10 nm. The exact values of L and L_ϕ depend on the sample's electron density and disorder (and temperature for L_ϕ). Reducing the density has been shown to reduce the mean free path L and the coherence length L_ϕ, as might be qualitatively expected if a larger number of strong potential barriers forms (as illustrated in figure 12 and 13) from which the electrons undergo inelastic scattering. The result of reducing the two characteristic lengths is to reduce the strength of the weak-localisation (equation (13)). Note that the weak-localisation equations are derived as an expansion in small $(k_F L)^{-1}$, where in 2D $k_F = \sqrt{2\pi n}$, such that for very low densities they might not be valid [89, 90]. At low densities, not only the dominant localisation effect is diminished, but also the Coulomb interaction screening. Therefore, it is to be expected that the electron diffusion gradually becomes dominated by electron-electron interaction effects and might crossover to a different regime.

The change in conductance as a function of temperature in phosphorus δ-layers is a logarithmic function, as mentioned earlier. As a result of the electron coherence length L_ϕ increasing with lowering temperature, the localisation becomes stronger, and the conductance lower. In terms of the derivative criterion $d\rho/dT$ from section 2.3, the phosphorus δ-layers would be considered as insulating. However, they are considered to be metallic as they have a density above the critical density calculated without taking the localisation effects into account [86], and because they have linear (Ohmic) I-V characteristics. Finally, it is noteworthy that in all dopant δ-layers the conductivity saturates at temperatures lower than $\sim$500 mK [59, 91], and such a saturating behaviour is observed in many other materials [12, 59–63]. So far this observed conductivity saturation remains unexplained [64].

Altogether, based on previous studies of phosphorus δ-layers in silicon, we can expect our arsenic δ-layers to have weakly-localised diffusive conductivity at high densities, and interaction effects at low densities. The fact that the layers are thinner makes it easier to detect interaction effect when a magnetic field is applied parallel to the layer. In addition, the heavier dopants should make the spin-orbit-coupling stronger, such that weak-anti-localisation effect or Rashba-Dresselhaus effects might be visible, however this is not the case in our samples.

3.4 Arsenic for one-and zero-dimensional devices in silicon

In 1998 the idea to use donors in silicon for quantum computing was first formulated by Kane [92]. It has led to the development of scanning tunnelling microscopy (STM) lithography, where single donor atoms can be positioned with atomic precision within the silicon lattice [88, 93]. The technique has successfully been used with phosphorus atoms to fabricate a wide variety of devices, ranging from two-dimensional dopant structures [94], to one-dimensional wires [95], and zero-dimensional devices such as single electron transistors [96]. The unique capability to make all these different structures within the silicon lattice has, for example, led to the demonstration of single qubit control and operation [97], and two-qubit gates and devices [98].

STM lithography is very similar to the technique used to fabricate global δ-layers (section 3.1), the main difference being that the clean silicon surface is exposed to hydrogen gas containing no dopant, instead of the phosphine or arsine gas. In this way, the silicon surface is terminated by a layer of hydrogen, from which single hydrogen atoms can be removed by applying local electrical pulses with an STM. Subsequently, the surface is exposed to phosphine or arsine gas which can bond only where the hydrogen was removed, and the rest of the fabrication is the same as for the global δ-layers. Importantly, the same annealing steps are necessary for dopant incorporation and activation, thus, the unwanted diffusion is the same in both fabrication methods. Therefore, improving global δ-layer thickness directly translates to an improved vertical placement precision in single atom devices fabricated by STM lithography.

Despite the impressive demonstration of all fundamental operations required for quantum computing in silicon, progress to larger qubit count in silicon devices is likely hindered by insufficient dopant placement precision in STM lithography. A main difficulty comes from the inability to tune the exchange coupling strength J between neighbouring donor, by precisely defining the inter-donor distance. The strength is not simply a smoothly decaying function of the inter-donor distance, as one could expect from the diminishing wave-functions' overlap, but has a strong cosine oscillation due to the six degenerate valleys [99]. The wave-functions tend

to concentrate around each valley, and the coupling strength J varies by orders of magnitude with a spatial period of the order of the crystal lattice constant, $a_0 \approx 0.5$ nm, as was calculated by Pica and Lovett [100], and shown in figure 15.

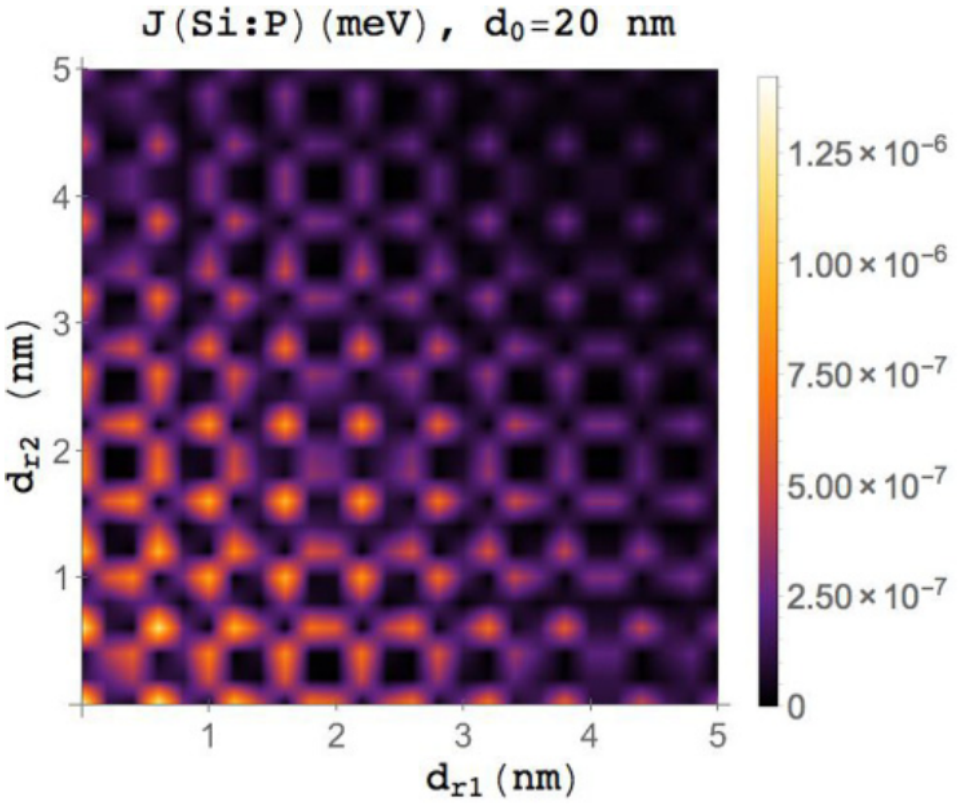

Figure 15: **Exchange coupling between phosphorus donor electrons in silicon.** Density plot of the exchange coupling J between neighbouring donors as a function of misplacements d_{r1} and d_{r2} in the orthogonal plane to the nominal donor separation $d_0 = 20$ nm. From [100].

The STM lithography fabrication process relies on the diffusion of the dopant atoms for incorporation and activation, and it has so far not been possible to control the final position with less than 1 nm placement precision [93]. To make matters more complicated, the number of incorporated phosphorus atoms per site is stochastic, and single phosphorus incorporation happens only with a $63 \pm 10\%$ likelihood of success [101]. While it is possible to partly mitigate these issues by building qubits based on clusters of multiple donor atoms, it remains necessary to improve donor-device fabrication precision, or to relax the fabrication constraints, *e.g.*, by increasing the coupling strength J.

In order to relax fabrication constraints in STM lithographically defined donor devices, there are two obvious approaches. One is to change the dopant species, the other is to change the semiconductor host material. Both approaches have

their benefits, and a combination of both could increase the benefits.

The interaction strength between neighbouring atoms has a strong lattice-constant sized oscillation due to the sixfold valley degeneracy in silicon, as shown in figure 15. This effect could be reduced by fabricating devices in germanium instead of silicon. In germanium there are only four degenerate valleys, leading to reduced oscillations in J, and the donor's electron effective mass is lower, leading to larger wave-functions and inter-donor coupling J. Calculations show that in germanium the same interaction J can be obtained at a three times larger distance [100]. While the move to germanium is a promising way to relax fabrication constraints for single-donor qubits, it will necessitate to adapt the STM lithography recipe and might not improve the precision in dopant placement.

The other possibility, to use a heavier group V dopant species, is pursued in this work. It is of interest because a larger and heavier atom will have a lower diffusivity, such that it can be annealed with less diffusion. Here we use arsenic, the next group V atom after phosphorus. Arsenic has been shown to have a lower diffusivity and a higher solid solubility in bulk silicon [102], two characteristics that imply better placement precision. Additionally, because of its larger atomic number, its 1s valence electron has a slightly larger Bohr radius $r_{As} = 115$ pm (compared to $r_P = 100$ pm for phosphorus) [103], its spin-orbit interaction is larger ($Z_{As} = 33$, $Z_P = 15$), and its nuclear spin is larger ($I_{As} = 3/2$, $I_P = 1/2$). The larger spin-orbit interaction and nuclear spin can be viewed to be additional channels for quantum computing schemes, and the larger Bohr radius implies increased coupling strength J between donors. For arsenic the STM lithography fabrication parameters are completely compatible with the ones for phosphorus. Finally, while the main advantage of using arsenic is the anticipated increase in fabrication precision, it will not solve the valley interference issue. However it will undoubtedly be useful to have the possibility to design multi-species donor devices in silicon, allowing, for example, to independently address each donor species [82].

In summary, it is of interest to develop the STM lithography technique with heavier group V donors, in particular arsenic, to improve fabrication accuracy, and to open the way to multi-species quantum devices. The first step towards replacing arsenic with phosphorus is to study the characteristics of 2D arsenic δ-layers in silicon to determine the vertical diffusion by measuring the dopant layer thickness, and to understand the physical mechanisms that govern the electrons in the new type of devices. A logical subsequent step will be to use germanium instead of silicon to reduce valley interference effects and further relax the spatial constraints.

4 Imaging of buried dopants

The development of atomic-sized buried structures in silicon for quantum applications relies on the continuous improvement of fabrication accuracy and characterisation methods. An important advantage of using donors in silicon is that the crystal lattice acts as a protection from external noise and unwanted interactions. However, the protection offered by the silicon lattice also poses a challenge in terms of the ability to image the devices non-destructively, a necessary ability for quality control and feedback for fabrication improvements. In effect, the STM lithography method described in section 3.1 does not allow for exact dopant placement measurement after the silicon overgrowth. Here, we explore the possibility to use synchrotron X-ray light to characterise the buried dopant devices, and importantly, show that X-ray fluorescence and reflectivity can give a full image of the sample without altering the dopants' position or electrical properties.

4.1 Resonant-contrast X-ray reflectometry for nm resolution depth-profiling of specific atomic-species dopant layers in silicon (paper manuscript)

Abstract

In the past decades, the miniaturisation of silicon-based electronics has been so successful that devices can now be made so small, that it has become a challenge to measure them. Here we demonstrate that resonant-contrast X-ray reflectometry (RCXR) can determine the depth-profile of a single sub-nanometer-thick dopant layer in silicon. The technique takes advantage of the large resonant change in reflectance of atoms at X-ray absorption edges. The specular angle-dependent reflection measured at energies on either side of an elemental resonance energy differs, which is used to obtain an atom-specific contrast. We show that this makes it possible to selectively measure the thickness of an arsenic-doped silicon layer within pure silicon, yielding a thickness of a $\gtrsim$1 nm layer of silicon doped with less than 5% of arsenic, and we compare the results to values obtained with destructive secondary-ion mass spectroscopy.

With the advent of scanning tunneling microscopy (STM) lithography in the nineties [104, 105], it became possible to fabricate dopant-based nano-electronic structures within semiconductors [106], as is, for example, commonly done with phosphorus donors in silicon [107]. In the meantime, industrially fabricated transistors have reached a 7 nm scale [108].

Imaging techniques have been lagging behind in terms of spatial resolution, however a number of methods are being developed or improved to obtain nanometer resolution. Some of those methods are destructive, such as atom-probe to-

mography [109] and secondary-ion mass spectroscopy (SIMS) [110], making them unsuitable for device inspection. Examples of non-destructive imaging techniques are X-ray fluorescence [1], X-ray diffraction [111], as well as, microwave impedance [74] and broadband electrostatic force [112] microscopy. Most of these techniques give two-dimensional information whilst with X-ray methods it is also possible to obtain three-dimensional images by tomography [113, 114] at the expense of time. X-ray reflectometry [115] on the other hand allows to measure the depth-profile of dopant layers in a reasonably short time of order ∼10 minutes per scan.

Here we show that X-ray reflectometry can be made more sensitive to a specific atom-species by measuring resonantly at energies around the respective X-ray absorption edge. Additionally the data analysis becomes model independent which is particularly interesting for dopant-defined devices in silicon, where the metallic structures typically contain less than 5% of dopant atoms.

Resonant-contrast reflectometry

X-ray reflectometry has first been used back in 1954 [116] and since then has become a prevalent technique at synchrotron light sources to study a wide variety of layered materials, ranging from surfaces to thin films and multilayers [117]. Reflectometry is based on measuring the specular reflection of a sample's surface, *i.e.*, the reflection at an angle $\pi - \theta$ for an incident beam at an angle θ with respect to the sample surface ($\theta = 0$ is parallel to the surface), as illustrated in Fig. 16b. In the simple case of a single interface between two materials, the reflectance R_s for sigma polarised light is given by the Fresnel equation

$$R_s = \left| \frac{n_1 \cos\theta_i - n_2 \cos\theta_t}{n_1 \cos\theta_i + n_2 \cos\theta_t} \right|^2 , \tag{8}$$

where θ_i and θ_t are the beam incidence and transmission angles, and n_1 and n_2 the refractive indices of the surface and buried material, respectively. The reflectance R_s is related to the material's atomic scattering factors f_1 and f_2 through the refractive index [118]

$$n = 1 - \frac{1}{2\pi} N r_0 \lambda^2 (f_1 + i f_2),$$

where r_0 is the classical electron radius, λ the photons wavelength, and N the average density of atoms. In the case of multiple layers, the reflection at different interfaces interfere. Depending on the beam's incident angle θ and the layers' thicknesses, this interference can be destructive or constructive. For a system with two interfaces, as shown in Fig. 16b, the condition for constructive interference is given by Bragg's law $2d\sin(\theta) = m\lambda$, with m an integer, and is periodic as a

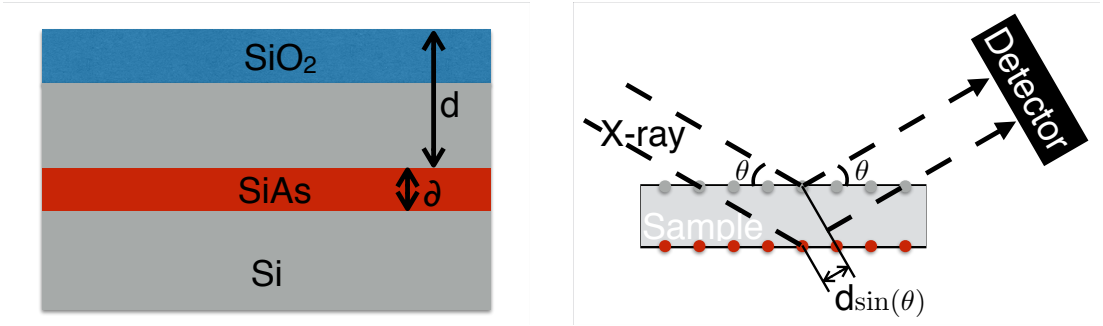

(a) (b)

Figure 16: **Schematic of the resonant-contrast X-ray reflectometry measurement.** (a) Schematic of the sample's layer structure. The surface consists of SiO_2 and Si with a combined thickness of d. Within the Si lattice there is an As-doped delta layer of thickness δ. (b) Schematic of the measurement geometry. X-rays shone on the sample with an incidence angle θ (with respect to its surface) and the specular reflection is detected with a photodetector placed at an angle 2θ (with respect to the incident beam). Positive interference occurs at $2d\sin\theta = n\lambda$ for two interfaces separated by a distance d, where n an integer and λ the X-ray wavelength.

function of $Q = 4\pi/\lambda\sin(\theta)$. For three interfaces the interferences is modulated by a cardinal sine, analogously to the double-slit experiment.

Data collected with X-ray reflectometry is traditionally analysed with programs that solve Maxwell's equations throughout the material [119, 120]. To obtain good fits to the reflectometry data it is necessary to take into account each layer's atomic-species, density, thickness and roughness, resulting in a high number of fitting parameters. Moreover, in the case that one of the layers is very thin and has a low material contrast, for example a layer of Si doped with $< 5\%$ of As as in our samples, the signal becomes indiscernible and the fit becomes insensitive to that specific layer. This is an issue expected in silicon-based nanoelectronics, where dopant structures are typically buried under two layers, *i.e.*, the Si and the SiO_2 surface.

To circumvent X-ray reflectometry's low sensitivity to dopant δ-layers in Si, we explore the possibility of using the dopant's L absorption edge as an amplifier of the dopant signal. The principle is simply to take two reflectivity measurements, one at an energy just below the dopant's L-edge and the other just above, and look at the difference between the two. This difference will primarily be a result of the dopant, because the material's scattering factors f_1 and f_2 undergo a large change at resonance, as is visible in the bottom inset in Fig. 17a, and because other atom-species have their resonances at different energies. In this way the signal from a specific atom-species can be isolated and its analysis is simplified. In

particular, no modelling is required and yet both the thickness and the species of a layer can be determined, unlike traditional reflectometry measurements where the data needs to be fitted to multi-variable models.

Experiment

Here we perform resonant-contrast X-ray reflectometry (RCXR) on As-doped Si δ-layers (Si:As) at the RESOXS station of the SIM beamline at the Swiss Light Source (SLS) of the Paul Scherrer Institut (PSI) [121, 122]. The sample is kept in high vacuum at 1e-8 mbar and at room temperature. It is mounted on a rotatable holder such that the incident angle θ of the beam can be swept from 0 to 90 degrees. The beam energy is set between 1200 eV and 1400 eV, with a spot size of 500 and 120 μm.

A schematic of the sample composition is shown in Fig. 16a. It is composed of Si with an As dopant δ-layer and an inevitable oxidised SiO_2 layer of about 2 nm on the surface. The doped layer has a density $n \approx 10^{14}\text{cm}^{-2}$, as determined by secondary-ion mass spectroscopy (SIMS) and during sample growth [82]. To fabricate the samples, a clean Si surface in ultra-high vacuum is exposed to arsine gas, which is integrated into the Si lattice by a rapid thermal anneal process and finally buried below the surface by epitaxial Si overgrowth. Four such samples were fabricated with the δ-layers buried at different depths between 15 and 75 nm, and one sample with a buried SiO_2 layer instead of As. All sample dimensions were 6×2 μm^2.

Arsenic L-edge resonance

The samples consist of three distinct layers, where the As-doped layer only contains about 5% of substitutional As, while the SiO_2 contains twice as many O atoms as Si. Because of this, the optical contrast between the Si and Si:As is small compared to that between SiO_2 and Si. Nonetheless, the As L-edge resonance is visible when measuring the reflected X-ray intensity as a function of X-ray energy at a fixed angle, as shown in Fig. 17a. The resonance can be attributed to the As, because its atomic scattering factors f_1 and f_2 change abruptly at the resonance energy, as can be seen in the figure's inset, while the Si and O atomic scattering factors remain a smooth function of the energy.

In the case that the exact two-dimensional density n_{2D} of dopant is known, it is possible to extract the layer thickness δ directly from the relative intensity of the As resonance (Fig. 17a). Indeed, the refractive index of the layers and the resonance intensity are determined by the the three-dimensional dopant density $n_{3D} = n_{2D}/\delta$ and the Fresnel equation at each interface (eq. 8), respectively. The

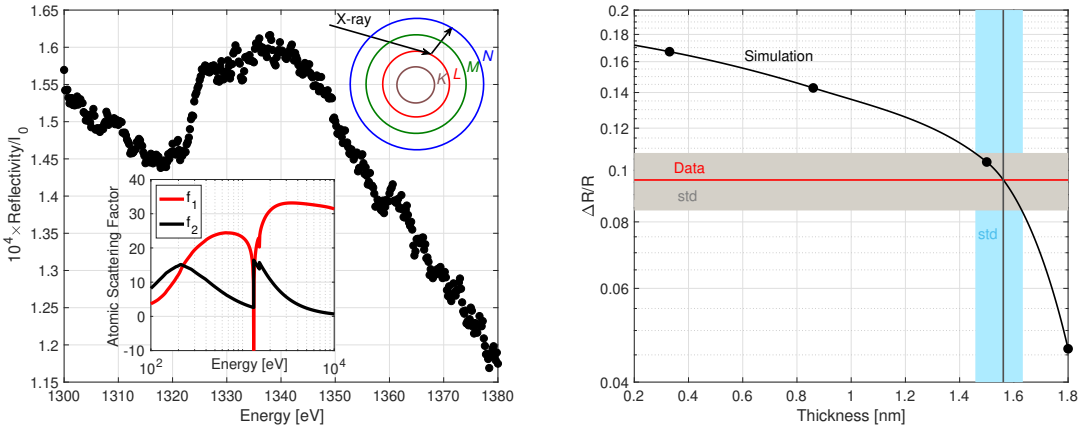

(a) (b)

Figure 17: **Reflectometry contrast across the As L-edge.** (a) Example data of the sharp edge at the As L-edge resonance at 1324eV, measured with an incidence angle of $\theta = 10°$. The reflected signal is normalised by the beam current I_0 to take into account incident photon flux fluctuations. The top inset shows a sketch of the resonant process in which an X-ray photon is absorbed and excites an electron from the L-shell to an unoccupied M- or N-shell. The bottom inset depicts the energy dependence of the As scattering factors, f_1 in red and f_2 in black, as they undergo a large change at at the L-edge. (b) In black, calculated $\Delta R/R$ for an As 2D density $n_{2D} = 2.77 \times 10^{14}$ cm^{-2}. In red $\Delta R/R$ extracted from the data in Fig. 17a, the grey area is the standard deviation. The intersection of the data and the calculation (gray line and light blue region) gives the As layer thickness $\delta = 1.55 \pm 0.09$ nm, in agreement with Fig. 19.

relative change in reflection $\Delta R/R = (R(1330\ eV) - R(1320\ eV))/R(1320\ eV)$ depends mostly on the three-dimensional dopant density n_{3D} of the layer that undergoes the resonance, here the arsenic doped layer, but it's absolute value also depends on all the other layers characteristics. As a consequence, if the dopant layer's n_{2D} and its depth are known, it is possible to obtain its thickness δ from its resonance spectrum.

The two-dimensional dopant density n_{2D} is readily obtained by X-ray fluorescence [1]. In principle it is straightforward to record the X-ray fluorescence and reflectometry simultaneously, as the fluorescence photons have an isotropic distribution, however n_{2D} was only measured for one sample in this work, and was found to be $n_{2D} = 2.77 \times 10^{14}$ cm^{-2} for the sample shown in Fig. 17, Fig. 18, and Fig. 19. For this sample, the expected relative change in reflection $\Delta R/R$ at the As resonance as a function of the dopant layer thickness was calculated with the DYNA program [120] and shown in Fig. 17b in black. The layer depth used for this calculation was obtained in Fig. 18a, as explained in the next section. As expected, decreasing the dopant layer thickness (and density at fixed n_{2D}), re-

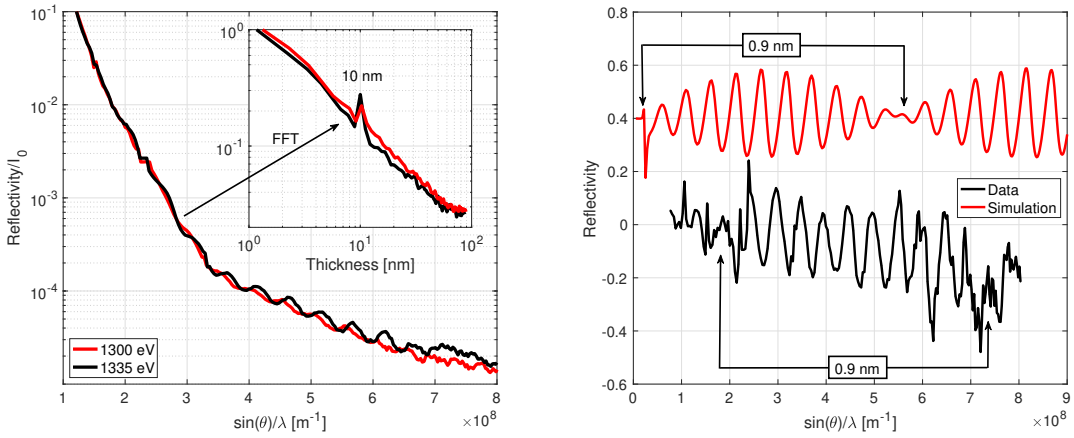

Figure 18: **As contribution to the reflectometry for photon energies below and above the As L-edge.**
(a) Example of an X-ray reflectometry curve with an X-ray energy below (red, 1300 eV) and above the As L-edge (black, 1335 eV). The data is obtained by rotating the sample and the photodetector such as to measure the specular reflection. The horizontal axis shows the projection of the wave-vector perpendicular to the surface normal, such that interference occurs are at the same values for both X-ray energies. The inset shows the fast Fourier transform (FFT) of the reflectometry curves, yielding the thickness d of the Si plus the SiO_2 on top of the As-doped delta layer. The fast oscillations are more apparent above the As L-edge. (b) Difference between the logarithm of a reflectometry curve measured at an energy lower and higher than the As L-edge. The black curve is obtained from the experimental data on the left, whereas the red curve shows a simulation of a 0.9 nm thick dopant layer (offset vertically by +0.4 for clarity). The arrows indicate the location of beatings in the envelope modulation of the signal and is associated with the As-dopant δ-layer thickness.

sults in an increased relative change in resonance intensity $\Delta R/R$. In figure 17b, the experimental value of 0.10±0.01 for $\Delta R/R$ extracted from Fig. 17a is drawn in red, with the grey shaded area representing its standard deviation. From the intersection between the data (red) and the calculation (black), the As layer's thickness can be deduced to be 1.55±0.09 nm. This result is in agreement with the wavelet transform analysis developed in the next sections, however it relies on fitting the resonance with each layer's thickness, density, and roughness, resulting in a large fitting parameter space and the necessity to have knowledge about all layers.

Enhancing the Arsenic signal

Typical reflectometry data for our samples are shown in the main plot of Fig. 18a. The data in black is taken at an energy of 1335 eV, above the As L-edge at 1324eV, and the data in red is taken at an energy of 1300 eV, below the As L-edge. The data show distinct fast oscillations that come from the reflection on the Si to Si:As interface. The periodicity of the oscillations is related to the layer thickness d through the Bragg condition $d = n\lambda/2\sin\theta$, such that a smaller d implies a larger period, and corresponds to a thickness $d = 10$ nm, as is obtained by taking the Fourier transform (see inset of Fig. 18a). The data also contain a much slower oscillation due to the top SiO_2 surface. Moreover, the fast oscillations are modulated by an envelope function with an even longer period due to the thin Si:As layer. The nodes of this modulation give the thin As δ-layer thickness δ. At very small angles no signal-structure is visible, because some of the light directly goes to the detector, while at high angles the roughness determines the overall signal intensity and oscillations fall-off [123].

To extract the modulation of the fast oscillations in the reflectometry data, we look at the reflectometry measured below and above the As L-edge resonance energy, at 1300 eV and 1335 eV, respectively. Figure 18b, shows the difference of the logarithm of both energies. The logarithm is used for clarity, since the reflected intensity decays exponentially. This subtraction removes the effect of the SiO_2 layer and keeps that of the As-doped layer because the scattering factors of the former are almost constant at those energies while they change drastically for the latter. The arrows indicate the apparent position of the nodes of the envelope modulation of the fast oscillations, where the distance between the two nodes corresponds to a Si:As layer thickness of $\delta = 0.9$ nm. For comparison, the same procedure is shown for a simulation (from [124]) of a 0.9 nm Si:As layer buried 10 nm into Si (with no oxide). At first glance, the experimental data and the simulation might look qualitatively in agreement, however, the oscillations in the data are not largest at the centre of the envelope and they decay abruptly at high and low angles ($\sin\theta/\lambda$), indicating a possible cutoff to the data. The fast decay of the signal at high angles originates from the roughness of the sample's surface and the noise limit at the largest incident angle where signal can be detected [118, 125, 126]. The roughness causes the signal at high angles to vanish because of increased noise, thus it acts as a cutoff and can misleadingly look like a modulation node of the signal. Similarly, at low angles the signal is limited by total internal refraction and by direct light reaching the detector, creating a lower cutoff. Both cutoffs limit the minimum measurable layer thickness, *i.e.*, the minimum thickness detectable with RCXR measurements depends on the surface roughness and is 0.9 nm for the sample shown in Fig. 18b. Therefore, it is not sufficient to find the modulation nodes by eye, but it is necessary to extract the

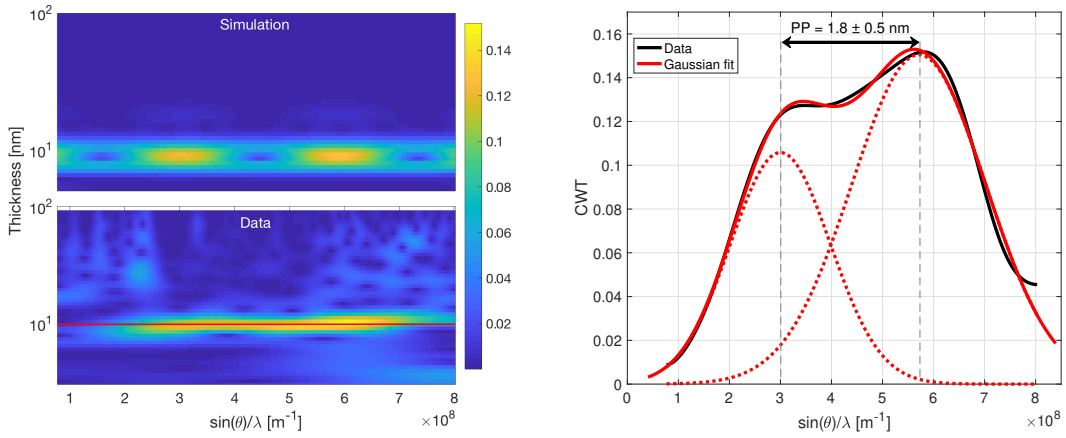

(a) (b)

Figure 19: **Dopant layer thickness extraction from the signal modulation.** (a) Wavelet-transform of the simulated data for a layer thickness of 1.8 nm (top) and of the experimental data from Fig. 18b (bottom). The red line indicates the cut shown on right figure. (b) Wavelet-transform amplitude obtained along the red line shown on the left. The obtained data (black) is fitted to two Gaussians (red). The peak to peak (PP) distance corresponds to an As layer thickness of 1.8±0.5 nm.

fast oscillations' amplitude as a function of angle and determine the modulation period.

A more sophisticated approach to estimate the modulation frequency is shown in Fig. 19, is to take the wavelet-transform [127] of the data resulting from the resonant-contrast. The wavelet transform is similar to the Fourier transform, in that the signal is decomposed into a reciprocal frequency space, however instead of being a projection onto sine functions of different frequencies, it is a projection onto the orthonormal Morse wavelet basis [128]. Because the wavelets are periodic oscillations that quickly decay in time, the wavelet transform retains both time and frequency information. In our case, the frequency domain is converted to the corresponding thickness and the time domain is the sine of the angle over the wavelength ($\propto$Q-vector). The colour scale of the wavelet transforms shown in Fig. 19a represents the intensity of the signal at a given angle and frequency, for the experimental data on the bottom, and for a simulation of a 10 nm deep and 1.8 nm thick As layer on top. The yellow regions indicate a large oscillation amplitude. The vertical position of the high amplitude region indicates the detected frequency corresponding to the sample's Si:As layer depth of $d = 10$ nm. To extract an estimate of the Si:As layer thickness δ, we take a horizontal cut through the yellow region of the wavelet-transform, as shown with a red line in Fig .19a and displayed in Fig. 19b, and fit the amplitude peaks to Gaussian distributions. This cut corresponds to the amplitude of the oscillations at the As doped-layer

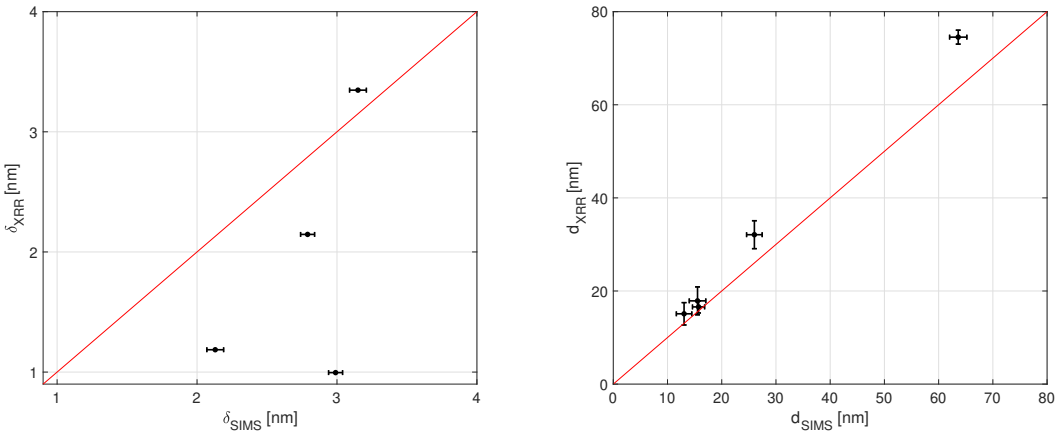

(a) (b)

Figure 20: **Dopant layer thickness and depth measured by RCXR and SIMS.** Comparison of thicknesses obtained by RCXR and SIMS, highlighting that SIMS over-estimates the Si:As layer thickness. (a) and (b) show the thickness δ of the Si:As layer and the depth d of the As layer below the surface, respectively. The values obtained by RCXR denote an upper bound and so no error is associated with them.

depth, here 10 nm. Each peak in Fig. 19b corresponds to a maximum modulation of the fast oscillations, and the peak-to-peak distance is the envelope modulation period, which is converted to a layer thickness of 1.8±0.5 nm using the Bragg condition. Note that the wavelet transform of the simulated data in Fig .19a has the same peak-to-peak distance corresponding to 1.8 nm as obtained from the data in Fig .19b, however the envelope function is a sine function and not Gaussian. This is because in the simulation the dopant layer has a step function distribution (of which the Fourier transform is a sine), while in the samples the real dopant distribution at the layer interface is Gaussian [] (of which the Fourier transform is a Gaussian). It should also be emphasised that in the presence of a low- and high-angle cutoff due to noise and roughness, the peak-to-peak period extracted in Fig. 19b gives a lower-bound estimate of the As layer's thickness. As mentioned before, the main advantage of this technique is that it determines the thickness of a chosen atomic-species layer without the need of any modelling and model-specific fitting.

Results

The RCXR experiment was performed on five different samples, of which four contained Si:As δ-layers and one reference sample contained only a SiO_2 layer. These samples were also measured with SIMS, a destructive technique commonly used to characterise Si δ-layers samples. The results for both techniques are shown

in Fig. 20. The measured depths d for the shallower samples coincide, whereas SIMS underestimates the depth of more buried Si:As layers. This discrepancy might originate from the variability of the SIMS sputter rate [129]. The measured Si:As layer thickness δ is found to be lower when measured with RCXR, as can be expected since SIMS is known for not being able to resolve thicknesses smaller than 2 nm [87]. The values for δ measured with RCXR are given with no error bar as they denote an upper bound. Nevertheless, the RCXR results show that our As δ-layer samples are as thin as 1 nm. This finding is consistent with a study based on angle-resolved photoemission spectroscopy (not published yet), where the thickness δ of Si:As samples fabricated in the same way was measured to be between 0.4 and 0.7 nm, suggesting that the value obtained here by RCXR is limited by the noise at large incidence angles which could be improved by reducing the surface roughness.

In conclusion, the sensitivity of X-ray reflectometry to specific elements can be improved in a layered sample by performing a differential measurement above and below a resonance edge of the element. With this technique it is possible to isolate the signal from one specific element with an increased sensitivity, without needing to model the material. RCXR yields an upper-bound of 1 nm on the thickness of As-doped δ-layer buried in Si containing $< 5\%$ of As ($\approx 10^{14}\mathrm{cm}^{-2}$). A lower upper-bound could be obtained by increasing the X-ray source fluence, or by reducing the sample surface roughness. Combining RCXR with X-ray fluorescence measurements will make it possible to fully and non-destructively characterise a sample in three-dimensions at the same beamline. In future experiments it will be possible to use this technique, combined with nano-X-ray beams of less than 10 nm spot-size [130] to measure the thickness of STM-patterned dopant structures, such as nano-wires and conduction leads in single-electron transistors and quantum bits.

4.2 Non-destructive X-ray imaging of patterned delta-layer devices in silicon (paper submitted [1])

Abstract

The progress of miniaturisation in integrated electronics has led to atomic and nanometre-sized dopant devices in silicon. Such structures can be fabricated routinely by hydrogen resist lithography, using various dopants such as phosphorous and arsenic. However, the ability to non-destructively obtain atomic-species-specific images of the final structure, which would be an indispensable tool for building more complex nano-scale devices, such as quantum co-processors, remains an unresolved challenge. Here we exploit X-ray fluorescence to create an element-specific image of As dopants in silicon, with dopant densities in absolute units and a resolution limited by the beam focal size (here ~ 1 μm), without affecting the device's low-temperature electronic properties. The As densities provided by the X-ray data are compared to those derived from Hall-effect measurements as well as the standard non-repeatable, scanning tunnelling microscopy and secondary ion mass spectroscopy, techniques. Before and after the X-ray experiments, we also measured the magneto-conductance, dominated by weak localisation, a quantum interference effect extremely sensitive to sample dimensions and disorder. Notwithstanding the 1.5×10^{10} Sv (1.5×10^{16} Rad/cm^{-2}) exposure of the device to X-rays, all transport data were unchanged to within experimental errors, corresponding to upper bounds of 0.2 Angstroms for the radiation-induced motion of the typical As atom and 3% for the loss of activated, carrier-contributing dopants. With next generation synchrotron radiation sources and more advanced optics, we foresee that it will be possible to obtain X-ray images of single dopant atoms within resolved radii of 5 nm.

The ability to build nanometre-scale dopant structures buried in silicon has led to great progress in classical and quantum technologies [131]. As the patterned structures become increasingly small and complex, it becomes indispensable to develop techniques to image the dopant structures non-destructively for device inspection and quality control [113, 132, 133].

Scanning tunnelling microscopy (STM) can be used to pattern acceptors and donors into silicon with atomic resolution using hydrogen resist lithography [93, 134]. The technique has been used to create complementary metal-oxide-semiconductor compatible structures, including two-dimensional conductive sheets [135], three-dimensional structures [136], nano-wires [106], and quantum dots [137]. Precisely measuring the location of buried dopants patterned by STM is challenging and can only be accomplished with STM itself for patterns extremely near to the

surface [138, 139]. Techniques capable of imaging such nano-scale structures are typically destructive, such as secondary-ion mass spectrometry (SIMS) [110] and atom probe tomography [109], making them unsuitable for device quality control [140]. Two techniques that can image the dopants non-destructively are broadband electrostatic force microscopy (bb-EFM) [112] and infrared ellipsometry [141], however both come with limitations. In particular, bb-EFM can only measure the polarity of the dopant but not its elemental species, whereas infrared ellipsometry can, in principle, obtain information regarding the species and density of atoms, but it is model-dependent and requires elaborate fits to the data.

Here we show that X-ray fluorescence (XRF) can be used to create non-destructive atomic-species specific images of dopants in silicon with a resolution only limited by the beam-size, in our case of order one micron. This technique uses synchrotron X-rays to locally ionise the atoms in the investigated device, leading to the emission of photons via fluorescence. The measurements are conducted at ambient temperature and pressure, and the photon spectrum is analysed to obtain the species and densities of the atoms in the device. Low-temperature magneto-transport on the two-dimensional Hall-bar device before and after imaging with the X-ray fluorescence demonstrates that the technique does not alter the electrical characteristics of the device, namely the free carrier density, electron mean free path, coherence length, and vertical confinement. We conclude therefore that the technique is non-destructive. As an extension of the principle demonstrated here, by rotating the sample in the X-ray beam it will be straightforward to obtain a tomographical three-dimensional reconstruction of the atoms' positions in the device [113, 114].

X-ray fluorescence

When an X-ray photon impinges on an atom it can be absorbed by the atom that will, in turn, be ionised. Inner orbital electrons are expelled from the atom and replaced by outer orbital electrons. In this process photons are emitted with wavelengths corresponding exactly to the energy difference between the electrons' orbitals. Therefore, the resulting energy spectrum of the fluorescence photons will uniquely identify the atomic species of the ionised atom. In the presence of many different atoms the fluorescence spectrum will be the sum of the different spectral lines. As each atomic spectrum is well known, it is straightforward to decompose an arbitrary fluorescence spectrum into element-specific components [142].

XRF experiments reported here were conducted at the microXAS beamline of the Swiss Light Source (SLS) synchrotron [143]. The beamline produces high brightness X-rays in the energy range from ~ 4 to 22 keV. At the photon energy of 11.88 keV used here, the delivered photon rate is approximately $I_0{=}10^{10}$ pho-

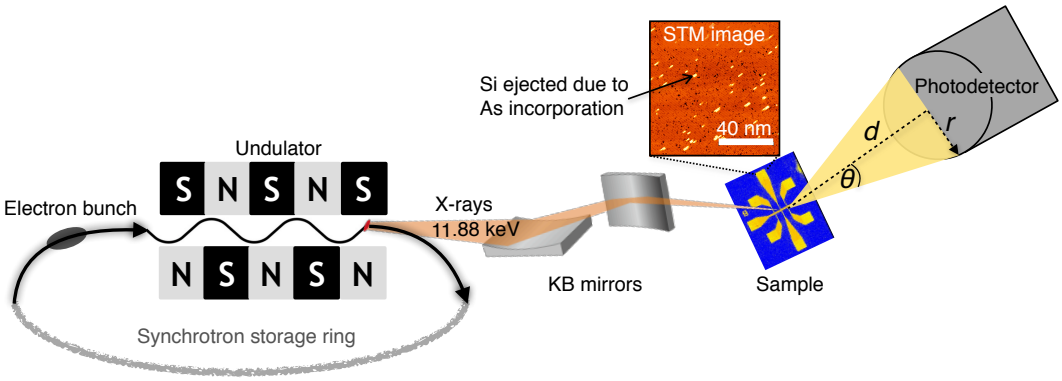

Figure 21: **Schematic of the X-ray fluorescence measurement**. From left to right: Electron bunches from the synchrotron are directed through the undulator magnets emitting highly collimated photons on account of the repeated electron beam bending. The X-ray beam with a photon energy of 11.88 keV from the synchrotron is focused to 1 μm with the help of a Kirkpatrick-Baez (KB) mirror system. Fluorescence photons from the sample that is illuminated by the X-ray beam are emitted in all directions and a photodetector is placed at $d = 2$ cm away from the sample, collecting the photons from a solid-angle $\Omega = 2\pi(1 - \cos\theta) = 2\pi(1 - d/\sqrt{d^2 + r^2}) = 0.04\pi$. The inset shows an STM image of the sample's doped silicon surface before silicon overgrowth; the short bright lines are rows of Si dimers ejected from the surface plane due to the incorporation of As atoms.

tons/sec when the beam is focused to 1×1 μm using a Kirkpatrick–Baez mirror system, and an energy resolution of $\Delta E/E < 10^{-4}$ is chosen. The beam was set to normal incidence. An X-ray energy of 11.88 keV is sufficiently high to dislodge core electrons from the As K-edge, without exciting the gold atoms found in parts of the sample holder.

Measurements are conducted in air at room temperature, with a gentle flow of helium gas into a 15 mm long pinhole cavity that encapsulates the silicon drift detector (SDD), with the exit gas flow located 2 mm from the sample position. A silicon drift detector with an active area of 50 mm^2 is placed in close proximity of the sample to maximise fluorescence photon collection. Figure 21 shows a schematic of the experiment; the solid angle captured by the detector is $\Omega = 0.04\pi$. The detector not only measures the intensity of the fluorescence photons but also resolves their energy spectrum, *i.e.*, it counts the number of photons reaching the detector as a function of photon energy, as shown in Fig. 22e. The collected spectrum is then decomposed into the sum of the individual atom-specific spectra with the PyMca software [144]. To determine the atom density from the detected fluorescence, it is compared to an arsenic containing reference sample from nanoXRF_standards [145] with a known density under the same X-ray beam illumination and placed at the same position as the measured device.

Device	n_{STM} (10^{14} cm^{-2})	n_{XRF} (10^{14} cm^{-2})	n_{Hall} (10^{14} cm^{-2})	n_{SIMS} (10^{14} cm^{-2})	t_{SIMS} (nm)	t_{MR} (nm)
#1	1.6 ± 0.3	1.40 ± 0.07	1.31 ± 0.03	1.8 ± 0.2	2.7 ± 0.2	0.97 ± 0.02
#2	0.10 ± 0.03	0.06 ± 0.01	—	0.21 ± 0.02	3.6 ± 0.4	—

Table 2: **Dopant density and layer thicknesses.** As density n of the two devices measured with STM, XRF, Hall effect and SIMS. Additionally the As layer thickness t is given as measured by SIMS and MR. Device #2 was not conductive and, therefore, Hall measurements were not possible.

The intensity of each fluorescence peak in the spectrum depends not only on the density of atoms participating in the fluorescence process, but also on the ionisation cross-section. Note that these X-ray ionisation cross-sections are well-known and do not depend on factors such as the atom's depth or environment. In XRF the measured density corresponds to the absolute number of atoms, unlike other non-destructive imaging techniques which measure only electrically activated dopants [132]. By comparing the atomic density to the free carrier density (obtained from magneto-transport, see Magneto-Conductance section) it is thus possible to deduce the activation percentage in a given device. Knowing the dopant electrical activation is important for optimising device fabrication; in particular when making atomic-scale devices it is important to have an activation percentage close to 100% to ensure that all donors contribute an electron to the conduction band.

At the microXAS beamline, the beam position is fixed and the sample was swept across the beam with a step size of 500 nm, and for each position a full spectrum of the fluorescence was recorded. The data collected in this way contain the information of the atomic concentrations at each position of the scan, from all elements that are excited with the chosen X-ray energy. By decomposing the full spectrum at each position into a sum of spectra from each possible element, a two-dimensional elemental density map is obtained.

Subsurface imaging

Structures consisting of atomically thin layers of As ('As δ-layers') buried 30 nm below the Si(100) surface were patterned into 20×200 μm^2 Hall-bars and contacted with aluminium as detailed in the methods. The As layer is made by exposing atomically flat silicon to a dose of arsine, annealing the wafer to incorporate the As into the surface layers, then overgrowing with epitaxial silicon. The As density is simply controlled by the total As dose. Two such structures are studied here, one with a nominal As density of $n_{\mathrm{As}} = 1.6 \times 10^{14}$ cm^{-2} and the other with $n_{\mathrm{As}} = 1 \times 10^{13}$ cm^{-2}. The dopant density is determined with the STM

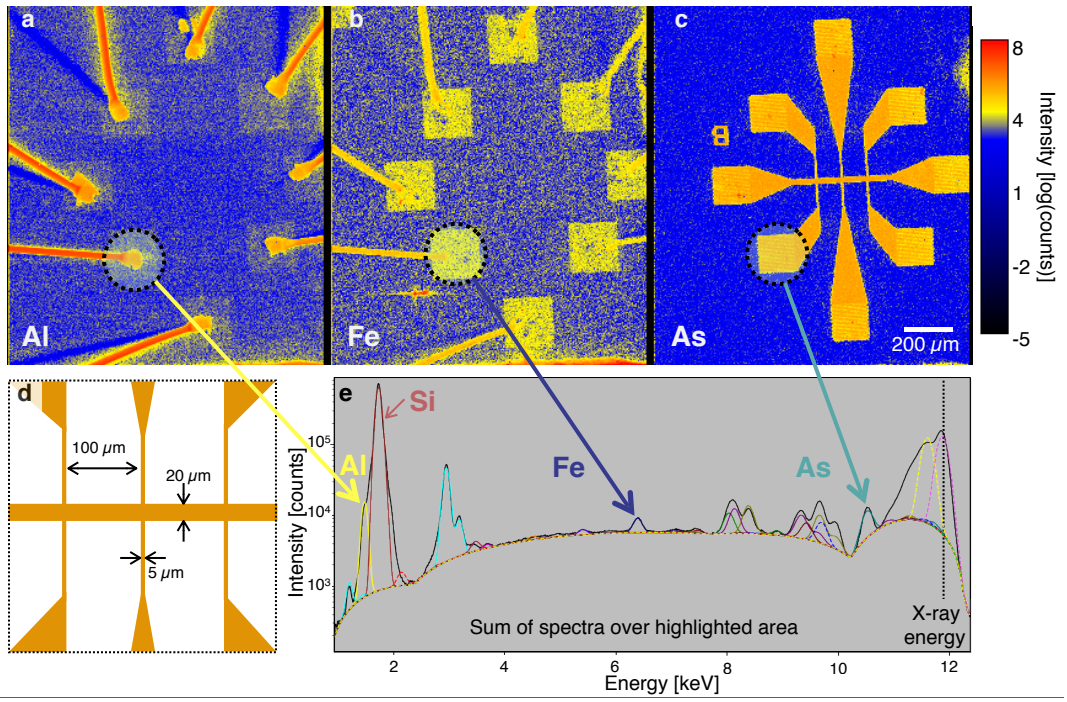

Figure 22: **X-ray fluorescence image of an As Hall-bar device. a-c** Al, Fe, and As distribution of device #1 with a density of $n_{\mathrm{As}} = 1.4 \times 10^{14}$ cm^{-2} for a photon energy of 11.88 keV, a beam size of 1×1 μm^2 and a step-size of 0.5 μm. At each step a spectrum is recorded during 200 ms. **d** Sketch of the top view of the samples with the As Hall-bar structure shown in orange. **e** Sum of the fluorescence spectra taken at each scan point within the highlighted area in **a-c**. The black line represent the measured data and the coloured lines are fits to individual elements. See Fig. 52 in the methods section for details on the elemental contributions.

before the silicon overgrowth by counting Si atoms ejected by the incorporated As, as seen on the inset in Fig. 21 and explained in [82] and the methods. The same devices were used for the XRF and the magneto-resistance (MR) measurements. Table 2 summarises the devices' density and thickness as measured by STM, XRF, SIMS and MR. Additionally, to quantify the background As dopant density a reference sample was measured.

Figure 22d shows a sketch of the studied devices, where the orange colour illustrates the two-dimensional As layer. Figures 22a-c depict the higher density Hall-bar structure #1 as imaged by XRF for Al, Fe, and As, respectively. For each pixel of the image a spectrum is recorded for a duration of 200 ms. The sum of many such spectra is shown in Fig. 22e with fitted peaks to deduce the elemental origin. Note that each element's fluorescence spectrum has peaks at unique energies (see methods), such that fitting the data is straightforward.

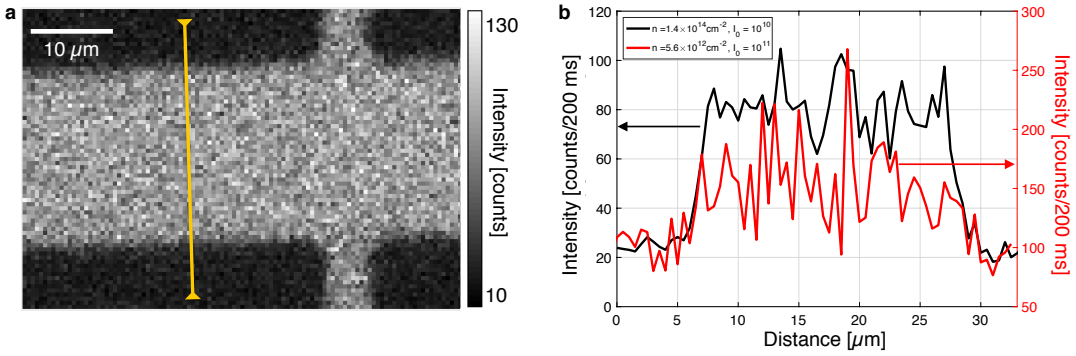

Figure 23: **Fluorescence contrast across the Hall-bars. a** As fluorescence image of the high density Hall-bar device #1, taken with a beamsize of 1×1 μm^2 and an averaging time of 200 ms. The image is obtained by scanning the beam across the sample, with the x-axis parallel and the y-axis perpendicular to the Hall-bar, respectively. The yellow line denotes the line trace. **b** Line traces in counts per dwell time measured across the Hall-bars of the high-density (black, $1{\times}1$ μm^2 spotsize and photon flux $I_0 = 10^10$ photons/sec) and the low-density device (red, $3{\times}1$ μm^2 spotsize, with 3 μm horizontal width and photon flux $I_0 = 10^11$ photons/sec). The As fluorescence signal clearly resolves the 20 μm width of the Hall-bar and features a signal/noise ratio of ~ 7 and ~ 2 for the high- and low-density Hall-bars, respectively.

The As image in Fig. 22c clearly shows the conductive layer of interest, which defines the Hall-bar and its contact leads. The unique possibility to distinguish different atomic species makes it possible to verify whether there is contamination in the device. Here the spectrum contains traces of many elements (see methods section for element identification), which originate from the lead-less chip-carrier, the glue used to fix the sample and the He gas that is blown on the sample (traces of Ar in Fig. 52). We also see that the Al contact pads and bonding wires contain not only aluminium, but also a very small quantity of Fe. The exact density is obtained by comparing the intensity of the fluorescence to the reference sample. While the Fe density is only $n_{\mathrm{Fe}} = 1 \times 10^{13}$ cm^{-2} in the Al contacts, it provides a stronger XRF signal than the aluminium whose density is $n_{\mathrm{Al}} = 6.0 \times 10^{15}$ cm^{-2}. This is due to the larger (107.3 cm^2/g) absorption cross-section of iron, compared to aluminium (14.76 cm^2/g), and the considerably larger absorption of the low energy Al fluorescence by the air/He atmosphere and by the detector window . The As density is uniform across the entire Hall-bar and is found to be $n_{\mathrm{As}} = 1.4 \times 10^{14}$ cm^{-2} and $n_{\mathrm{As}} = 5.6 \times 10^{12}$ cm^{-2}, for the two devices measured. For both the values obtained with XRF and STM agree within the uncertainty (see Tab. 2). The uncertainty in XRF measurements is low because atomic cross-sections are well-known, such that the reference sample yields an uncertainty of less than 5%. By comparing the atomic density to the free carrier

density obtained from Hall measurements we find that the dopant activation in the high-density Hall-bar device #1 is $94 \pm 5\%$. The low-density device #2 was not conductive and no Hall density could be measured.

The low-density device #2 was also measured in an identical fashion except that the beam size was increased to 1×3 μm^2 yielding a photon flux of $I_0 = 10^{11}$ photons/sec. That way, in the low- and high-density device there were 1.7×10^5 and 1.4×10^6 As atoms within the spot size, respectively. Taking into account the As cross-section, the number of photons absorbed collectively by the As atoms in 200 ms was 1.9×10^5 and 4.8×10^5 photons for the low- and high-density device, respectively. Figure 23 shows the contrast obtained when measuring the As fluorescence peak intensity across the Hall-bar structures. The contrast in the fluorescence signal when moving the beam on and off the dopant layer has a signal/noise ratio of $\sim$ 2 and $\sim$ 7 for the low- and high-density device, respectively. Through the use of focusing elements, *e.g.* Fresnel zone plates, the X-rays can be focused beyond the beam size of $\sim$ 1 μm used here. In this way, it will be possible to obtain fluorescence images of buried structures reaching a resolution better than tens of nanometres, while still maintaining the demonstrated sensitivity to low densities [130, 146–148].

5 Electrons in buried dopant layers

5.1 Localisation and confinement at saturation density

5.1.1 Weak-localisation in the metallic phase to measure the electron displacement induced by X-rays (continuation of X-ray fluorescence paper)

Weak localisation

The XRF images obtained from the two-dimensional As Hall-bars show that the technique is highly sensitive and directly discriminates atomic species without requiring any modelling of the sample. We measure the low-temperature electrical characteristics of the high-density Hall-bar devices #1 in magnetic fields up to $B = 9$ T before and after exposure to the X-rays. At $T = 1.8$ K electrons move diffusively, resulting in a conductivity $\sigma_0 > e^2/\hbar$ and are in the so-called weakly localised regime, as evidenced by a logarithmic temperature dependence of the zero-field conductivity [6, 8, 11, 149]. Weak localisation is a quantum interference effect that occurs for electrons in a medium with time-reversal symmetry, such as silicon, so long as the electrons' coherence length is longer than their mean free path. In that case an electron's trajectory can form a loop and interfere constructively with itself—it is weakly localised. This interference effect and particularly its behaviour in external magnetic fields depends strongly on the disorder and dimensions of the electron channel and so is an ideal diagnostic of radiation damage.

In the weakly localised regime, the conductance can be described by the Hikami-Larkin-Nagaoka theory [6], in which the conductivity change resulting from an applied magnetic field depends only on the electron mean free path L, the coherence length L_ϕ, and the applied magnetic field B. If the conductive medium is purely two-dimensional and there are no spin-orbit or electron-electron interaction effects, only field components $B_\perp$ perpendicular to the conductive plane can couple to the electrons' orbital degree of freedom. The corresponding conductivity change is then given by

$$\Delta\sigma(B_\perp) = \sigma_0 \left[\psi\left(\frac{1}{2} + \frac{B_\phi}{B_\perp}\right) - \psi\left(\frac{1}{2} + \frac{B_L}{B_\perp}\right) + \ln\left(\frac{2L_\phi^2}{L^2}\right) \right], \tag{9}$$

where $\psi(x)$ is the digamma function, $\sigma_0 = \frac{e^2}{2\pi^2\hbar}$, e is the charge of an electron, and $\hbar$ is the reduced Planck constant. The phase breaking field is given by $B_\phi = \frac{\hbar}{4eL_\phi^2}$ and the elastic characteristic field $B_L = \frac{\hbar}{2eL^2}$.

Our samples have a finite thickness, meaning that electron orbitals can have a small perpendicular component that can couple to a field $B_{||}$ parallel to the

conductive plane, the effect is described by [150]

$$\Delta\sigma(B_{\parallel}) = \sigma_0 \ln(1 + \gamma B_{\parallel}^2), \tag{10}$$

where γ is obtained by fitting the equation to the data and depends on the sample thickness t and roughness. By fitting $\Delta\sigma(B_{\perp})$ and $\Delta\sigma(B_{\parallel})$ we can derive this thickness as [151]

$$t = \left(\frac{1}{4\pi}\right)^{1/4} \left[\left(\frac{\hbar}{eL_{\phi}}\right)^2 (\sqrt{n}L\gamma)\right]^{1/2}, \tag{11}$$

where n is the free carrier density as measured by the Hall effect. Finally, for tilted magnetic fields the change in conductance can be described by the phenomenological expression [59]

$$\Delta\sigma(B)^p = \Delta\sigma(B_{\perp})^p + \Delta\sigma(B_{\parallel})^p, \tag{12}$$

where p is obtained by fitting the data and is sample and temperature-dependent.

Magneto-conductance

To establish whether the XRF imaging technique is non-destructive, we measure the magneto-transport at $T = 1.8$ K of high-density device #1 before and after the exposure to the X-rays. During the X-ray imaging the sample absorbs $2'000$ photons/nm^2 at an energy of 11.88 keV, corresponding to a radiation dose of 1.5×10^{10} Sv (1.5×10^{16} Rad/cm^{-2} or 1.7×10^{-14} J/nm^3). Taking into account the absorption lengths of Si and the As atoms doped into silicon, as well as the As atom cross-section, we find that each As atom absorbs on average 0.3 photons during the measurement.

Figure 24a shows the Hall effect measured in a magnetic field of up to $B = 9$ T, before and after the X-ray measurement shown in red and black, respectively. The transverse resistance R_{xy} is linear in the field and crosses zero with no signs of quantised, non-linear, or anomalous Hall effects. Combining the Hall effect with the device's zero-field conductivity gives a mean free path $L = \sqrt{2\pi n}\mu\hbar e = 4.8 \pm 0.1$ nm and $L = 4.9 \pm 0.2$ nm before and after the XRF measurements, respectively, where μ is the electron mobility. The derived Hall electron density is $n = 1.31 \pm 0.03 \times 10^{14}$ cm^{-2} before and $n = 1.27 \pm 0.06 \times 10^{14}$ cm^{-2} after the XRF measurements. Comparing the free carrier density to the dopant density obtained from the X-ray florescence shows that the activation percentage for this device amounts to $94 \pm 5\%$. Figure 24b shows the magneto-conductance at $T = 1.8$ K with a field up to $B = 9$ T applied perpendicular and parallel to the conductive plane. Fitting the data to Eq. (9) and (10) yields the electron channel's

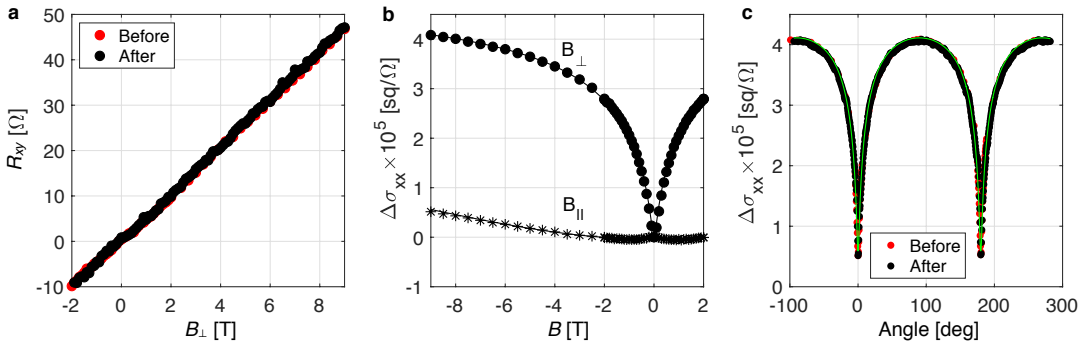

Figure 24: **Magneto-transport of the Hall-bar device before and after XRF measurements.** **a** Hall effect measured at $T = 1.8$ K, before (red) and after (black) the XRF imaging. **b** Magneto-conductance for a magnetic field perpendicular (dots) and parallel (stars) to the conductive layer. The lines are fits to Eq. (9) and (10). **c** Change of conductance in square per Ohm, as a function of the magnetic field angle with respect to the conductive layer at an external field of $B = 9$ T ($0° \equiv$ in-plane field). The green line is a fit to Eq.(12).

characteristic parameters. Before the XRF, the magneto-conductance yields a coherence length of $L_\phi = 73.6 \pm 0.4$ nm and δ layer thickness of $t = 0.98 \pm 0.02$ nm. After the XRF measurement we obtain $L_\phi = 74.2 \pm 0.3$ nm and $t = 0.97 \pm 0.02$ nm. Finally, Fig. 24c shows the change in conductivity as a function of the out-of-plane angle of a 9 T magnetic field before and after the X-ray measurement. According to the Eq. (12) the field direction-dependent data contains information of both $\Delta\sigma(B_\perp)$ and $\Delta\sigma(B_\parallel)$. Fitting the data to Eq. (12), we obtain $p = 1.9 \pm 0.3$ and $p = 2.3 \pm 0.5$ before and after the XRF, respectively. Combining this with Eq. (9) and (10), as well as the Hall measurements implies that, within error bars, none of the device's electronic characteristics were altered by the X-ray measurement. In particular, it is important to note that the determination of the thickness by the weak-localisation measurements has a precision of 0.2 Å, which sets a strict bound to the extent X-rays could have displaced the atoms.

We have shown that X-ray fluorescence imaging is a technique well-suited for non-destructive investigation of dopant-based devices in silicon. This approach has the unique capability of directly identifying dopant species without relying on sample modelling, making it an attractive alternative to bb-EFM and infrared ellipsometry. X-ray scattering techniques can be used in parallel to fluorescence imaging to obtain complementary information, such as strain fields [111] and overall device layout and morphology [113,133]. Additionally, with magneto-transport measurements, we confirm that the technique does not affect the electronic properties of the measured devices, *i.e.*, it is non-destructive for Si:As, an important condition for useful device characterisation. This is in contrast to common inspection techniques such as electron microscopy and SIMS which always entail

sample destruction. Finally, with the three orders of magnitude enhancements to brilliance expected for beamlines, including focusing optics, as well as improvements both to detector solid angle and signal/noise, it is reasonable to anticipate the ability to locate single As atoms in devices to within several nm over time scales of order seconds per imaging pixel. Radiation effects will then need to be mitigated via the same strategies already exploited for X-ray ptychography today [152, 153] and diagnosed exploiting the single electron transistor characteristics of such atoms [96, 154].

5.2 Soft X-ray ARPES and magneto-resistance

In the previous sections, we used X-rays to non-destructively image the dopant distribution in our samples. The results show that our arsenic doped δ-layers are sub-nanometer thin, making them the thinnest 2D dopant layers fabricated in a semiconductor. Moreover, we determined that the doping density is homogeneous across the sample, with no sign of changes near the edges induced by the reactive ion etching. Having the ability to implant a new type of dopant (arsenic), to control its density, and to have unprecedented layer thinness, motivates the systematic study of our samples' low-temperature conduction properties. As explained in section 2 and 3, the interplay between the dopant density, disorder, and interaction effects can lead to multiple different phases around the density driven MIT.

Dopant species, depth	n (10^{13} cm^{-2})	μ (cm^{2}V^{-1}s^{-1})	σ_0 ($10^{-4}\Box/\Omega$)	$n_{2D}^{-1/2}$ (nm)	$n_{3D}^{-1/3}$ (nm)	L (nm)	L_ϕ (nm)	d (nm)	k_FL ( )
P, 15 nm	18.73±0.06	51.8±0.2	15.556±0.005	0.7	1.7	11.7±0.04	86±6	10±1	40.1±0.2
As, 20 nm	12.23±0.08	27.3-±0.2	5.3516±0.0004	0.9	1.1	4.98±0.04	75±1	1.46±0.08	13.8±0.1
As, 20 nm	10.18±0.09	22.4±0.2	3.649±0.002	0.99	1.1	3.72±0.04	57.6±0.3	1.26±0.03	9.4±0.1
As, 20 nm	9.15±0.09	15.4±0.2	2.2511±0.0006	1.05	0.77	2.42±0.03	41.9±0.2	0.41±0.04	5.80±0.09
As, 20 nm	8.47±0.03	34.4±0.1	4.67±0.01	1.1	1.1	5.23±0.02	77.4±0.5	1.04±0.04	12.07±0.06
As, 15 nm	2.82±0.05	42.4±0.9	1.92±0.02	1.9	1.9	3.72±0.09	27.5±0.3	1.82±0.07	4.9±0.1
As, 20 nm	2.3±0.3	29.7±0.1	1.0879±0.0002	2.1	1.01	2.3±0.01	31.75±0.01	0.24±0.06	2.8±0.4
As, 20 nm	2.14±0.02	38.9±0.3	1.3314±0.0008	2.2	1.3	2.97±0.02	35.5±0.2	0.42±0.06	3.44±0.04
As, 20 nm	1.70±0.04	44.5±0.1	1.210±0.005	2.4	1.7	3.03±0.07	23.2±0.2	0.88±0.06	3.1±0.1
P 15 nm	1.61±0.02	34.5±0.5	0.891±0.008	2.5	2.0	2.29±0.04	20.5±0.5	1.3±0.1	2.30±0.05
As, 20 nm	1.18±0.01	35.6±0.3	0.6708±0.0002	2.9	1.8	2.01±0.02	22.4±0.2	0.65±0.05	1.73±0.02

Table 3: **Characteristics of the electron layers in this work.** All values are extracted from magneto-conductance measurements taken at 2 K. n is the 2D electron density, μ the electron mobility, σ_0 the conductivity at 2 K, $n_{2D}^{-1/2}$ the average distance between donors in 2D, $n_{3D}^{-1/3}$ the average distance between donors in 3D, L the electron mean free path, L_ϕ the electron coherence length, d the δ-layer thickness, and k_F the Fermi wave-vector.

In this section, we look at the low temperature magneto-conduction and photo-emission of the electrons in arsenic and phosphorus δ-layers. Both techniques probe the conduction electrons directly and not the dopant atoms, as was the case in the previous section. Therefore, the photo-emission measurements give relevant information for the magneto-transport experiments. The most striking results are

the appearance of a low temperature inhomogeneous phase in low density samples, which is evidenced by an even in magnetic field transverse voltage V_{xy}, hysteresis in both longitudinal V_{xx} and transverse V_{xy} voltages. The magneto-transport results are discussed in section 5.2.2. A summary of the samples used for the experiments is given in table 3.

5.2.1 Soft X-ray ARPES

In a work lead by Procopios Constantinou [155] on the same 2D δ-layer samples used here, soft X-rays (300–1600 eV) were used to measure angle-resolved photoemission spectroscopy (ARPES). In ARPES experiments, monochromatic light dislodges electrons from a material of interest, and the angle-dependent kinetic energy distribution of the emitted electron is analysed to obtain the electrons' energy distribution and thus the energy band structure (in reciprocal space). The technique, can be used with ultra-shallow devices, as the soft X-rays penetrate a few nanometres beneath the silicon surface [156]. The scope of the experiment was to precisely determine the vertical confinement of the dopants' electrons in the δ-layers, by looking at the effect of confinement on the electron conduction band.

Silicon has six degenerate valleys, such that in reciprocal space there are six minima along the <100> direction. When silicon is bulk-doped with group V atoms, the donor electrons will occupy the six valleys, and the Fermi surface will be an ellipsoidal shape around each minimum, as shown in figure 25b in green. The electron effective mass in each minimum has two components: the longitudinal and transverse effective mass, denoted m_L^* and m_t^*, respectively. However, in the case that the doping is strongly two-dimensional, as in our δ-layers, the confinement in the two Γ valleys perpendicular to the the doping layer (k_z direction) causes quantisation of the electron energy levels in the k_z direction. In the limit that the confinement is arbitrarily small, the effective mass m_t^* in the Γ valleys becomes infinitely large and the Fermi surface in the Γ valleys becomes a cylinder, as shown in figure 25c in purple. In the more realistic case of a quasi-2D layer, the Γ valleys will have a shape in-between the ellipsoidal and cylindrical shapes, with the strength of the cylindrical character indicative of the confinement dimension.

The confinement well, illustrated in figure 25.a, causes the out-of-plane and in-plane valleys to split into three sub-bands, denoted 1Γ and 2Γ for the two out-of-plane valleys, and Δ for the four in-plane valleys. As a result, strong 2D confinement creates three distinct "flavours" of electrons with different effective masses and populations.

The ARPES measurements conducted on shallow δ-layers reveal the elongation of the Fermi surface in the Γ valleys. The results for a phosphorus and an arsenic

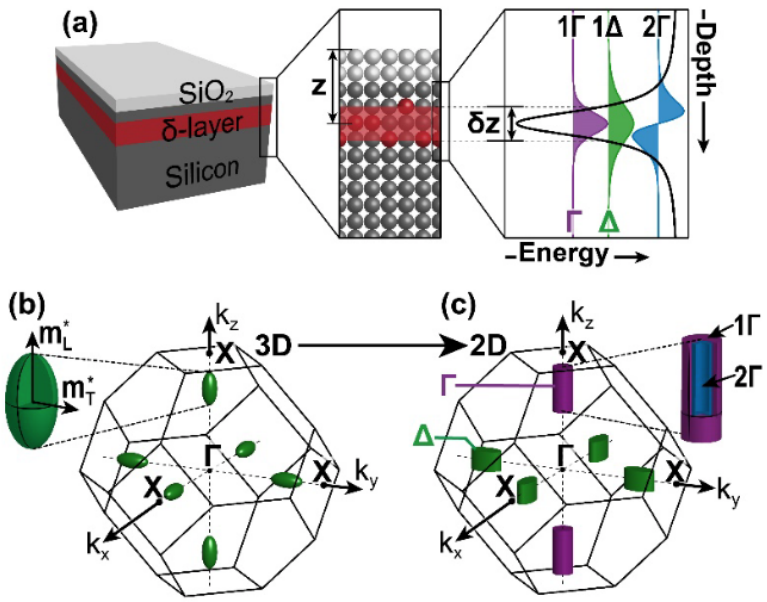

Figure 25: **Schematic of the samples and conduction valleys.** (a) The thin dopant layer (red) creates a vertical potential well. In the potential well the electron energy levels are quantised into 1Γ, 2Γ and Δ. (b) In Bulk doped silicon the donor electrons occupy six degenerate ellipsoidal valleys (in green on the left). In 2D doped silicon, the Γ valleys in the k_z direction deform into cylinders (right). The colours of the valley indicated the energy level from (a) populating it. Courtesy of Procopios Constantinou [155] .

sample are shown in figure 26, where the sketches on the left show the different planes measured in the ARPES data (purple, green, and orange). The purple cuts show the deformation of the Fermi surfaces in the $+k_z$ and $-k_z$ directions, and highlight that in arsenic layers (figure 26.f) the surface is more cylindrical than in phosphorus layers (figure 26.b), or in other words: the dopant confinement is stronger with arsenic atoms. The exact dopant layer thickness δz is obtained by the inverse of the difference of the Fermi surface's extent in the k_z direction in the 3D case (δk_z), and in the measured 2D case (δk_∞) : $\delta z = 1/(\delta k_z - \delta k_\infty)$. It was found that the arsenic layers are ∼0.5 nm thick and the phosphorus layers are ∼1 nm thick (the exact results for arsenic are in table 4), showing that our new arsenic δ-doped samples are the thinnest 2D electron liquids ever fabricated in silicon.

The slices through the Δ valleys displayed in figure 26.c and 26.g, show that in the absence of confinement all valleys are equally populated. By measuring the area enclosed by the Fermi surfaces in the $k_x - k_y$ plane (figure 26.c, 26.g, 26.d and 26.h), the 2D electron density n is obtained. For these two samples we find $n = 0.81 \pm 0.08 \times 10^{14}$ cm^{-2}, close to the expected saturation density value

of 1.4×10^{14} cm^{-2}, and in agreement with Hall measurements.

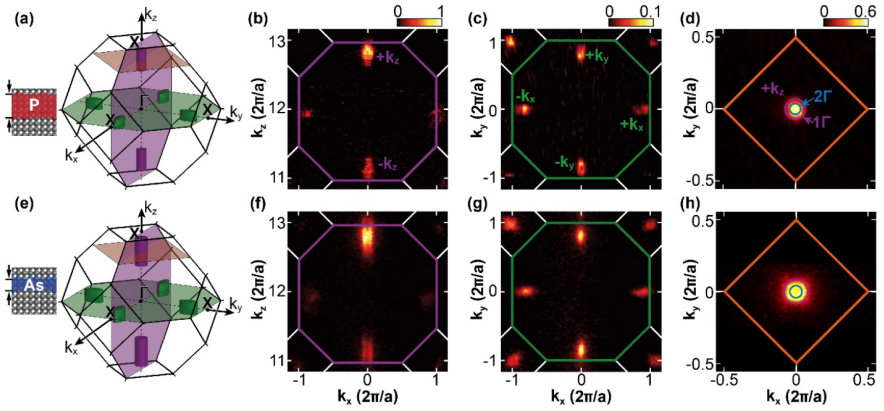

Figure 26: **Fermi-surface measurements of the six conduction valleys in doped silicon.** (a,e) Schematic of the six conduction valleys and the Fermi surfaces ARPES slices shown in (b,f, c,g, d,h). (b,f) ARPES measurements of the k_x-k_z plane, (c,g) ARPES measurements of the k_x-k_y plane, (d,h) ARPES measurement in the k_x-k_z plane through the centre of the upper k_z valley. Courtesy of Procopios Constantinou [155].

The quantisation of the energy levels in the k_z direction is observed with ARPES in figure 27c-f for the four studied samples. The fitted energy distributions of the two states, 1Γ and 2Γ, are shown on top of each plot for the momentum, and on the right for the energy. In percentage of the electron density, the 2Γ state is more populated in the thinner arsenic layers than in the phosphorus layers. The summary of the energy distribution of the electrons in each sample is shown in figure 27.b, the thinner layers have a lower total electron density, and a more even distribution of the electrons in the three states 1Γ, 2Γ, and Δ. Figure 27 shows that the thinner the δ-layer is, the more the 1Γ and 2Γ levels are split, as expected for confined electrons.

In table 4 we show the results obtained for the δ-layer thickness of four samples using four different techniques. It stands out that SIMS is a technique that cannot resolve features thinner than ∼2 nm, and that soft X-ray ARPES and magnetoresistance have similar accuracy and concurring results to within 0.1 nm. The X-ray reflectometry from section 4.1 cannot directly be compared to the soft X-ray ARPES because it was only tested on deeper samples, however it gives a slight over-estimate of the δ-layer thickness as explained in section 4.1. Note that the 2 nm deep As layer has a thickness of 0.45 nm corresponding to three Si(100) crystal planes.

Constantinou's work showed that soft X-ray ARPES is an extremely sensitive tool to measure electron layer thicknesses in silicon with Angstrom precision, and that the use of arsenic leads to improved 2D confinement. The work showed

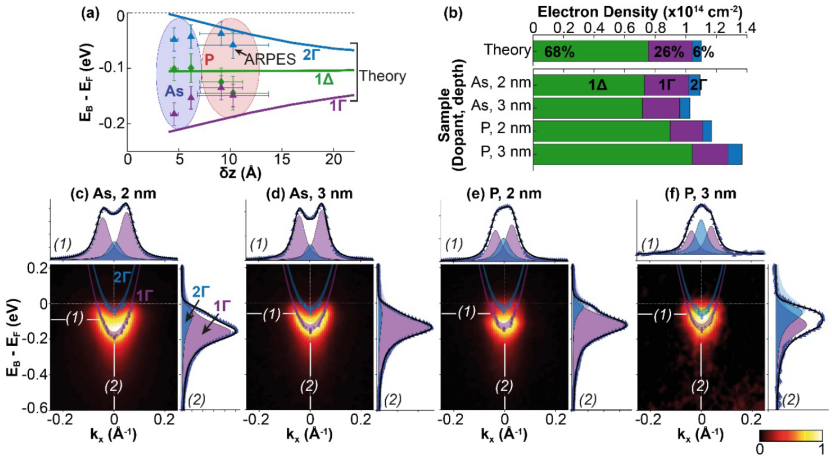

Figure 27: **Conduction band quantisation.** (a) Energy of the 1Γ, 2Γ, and Δ sub-bands as a function of the confinement width δz. (b) Measured electron density and sub-band distribution for each sample. (c-f) ARPES data showing the Γ band dispersion for each sample. The fitted electron momentum and energy distributions are shown on top and on the right of each plot, respectively. Courtesy of Procopios Constantinou [155].

As δ-layer depth (nm)	SIMS (nm)	Magneto-resistance (nm)	SX-ARPES (nm)	XRR upper-bound (nm)
2	2.0±0.2	-	0.45±0.04	-
3	2.2±0.2	0.4±0.1	0.6±0.1	-
18	3.0±0.1	-	-	1
32	2.8±0.1	1.46±0.08	-	2.1

Table 4: **δ-layer confinement.** The thickness d of the As layers measured by secondary-ion mass spectroscopy (SIMS), magneto-resistance, soft X-ray (SX) ARPES, and X-ray reflectometry (XRR) for As δ-layers with various depths. The XRR values are upper-bounds and as such are given without uncertainty.

that the vertical confinement causes the six-fold degenerate energy states to split into three separate sub-bands, and the occupancy of each energy level can be accurately measured. The results highlight that for strong confinement and low density of the electrons, the three energy sub-bands have similar occupancy, implying that for the analysis of 2D dopant electrons in silicon, at densities near the MIT, it might be necessary to take into consideration the three distinct flavours of electrons.

5.2.2 Magneto-transport of variable density few-layers group-V doping in silicon

Abstract

We report on magneto-transport evidence of an inhomogeneous phase in two-dimensional dopant layers in silicon, near the metal-to-insulator transition, associated with an anomalous Hall response and hysteresis. In this work we use gas-phase dosing of dopant precursor molecules on silicon to create arsenic and phosphorus δ-layers as thin as 0.4 nm and as dilute as 10^{13} cm^{-2}. We show that for such low dopant densities electron-electron interactions play an important role in the magneto-transport through the isotropic (in magnetic field) Zeeman effect, and we show how the Zeeman and conventional weak-localisation effects combine additively to yield the net magnetoconductivity.. In addition, we show that when the δ-layers are cooled below $\approx$ 300 mK, they cross over to an inhomogeneous state where more conducting and more localised/insulating regions coexist. The associated random anisotropy of the sample is reflected in a significant increase of the transverse voltage V_{xy} response (even in magnetic field). Inelastic scattering of the diffusive electrons on the insulating inclusions acts as a temperature independent cut-off to the coherence length, and causes the conductivity to saturate at low temperatures. For dilute layers, the low temperature phase is marked by a hysteretic longitudinal and transverse magneto-conductance, an anomalous even V_{xy} effect, and anisotropic conduction.

Introduction

The physics of two-dimensional (2D) electron gases has been the subject of extensive experimental and theoretical research efforts since the 60s, and has led to some of the most remarkable discoveries in solid-state physics, including the quantum Hall effect [157], and topological quantum states of matter [158]. Despite considerable advances, 2D materials remain the subject of intense ongoing research because of the many possible consequences of combined disorder, intersite hopping, and Coulomb interaction effects. A problem that has proven to be elusively difficult to solve is the nature of the metal-to-insulator transition (MIT) in two-dimensions. It went from being widely thought to be nonexistent in the 80s and 90s, because it was believed that localisation would turn any 2D material into an insulator [39], to being observed in most 2D systems [42–48]. While the 2D MIT has been studied in many materials, the mechanisms driving it and the phases associated with it remain an open question [49, 159]. In silicon, 2D electron layers can be formed in a number of ways, for example with silicon MOSFETs [40], silicon quantum wells [160], and silicon δ-doped layers [161]. In these systems the electron mobility and the disorder strength are substantially different, nonetheless they all exhibit the MIT at similar interaction parameter

strength $r_s \approx 20$ [53], defined as the ratio of the Coulomb energy and the Fermi energy ($r_s = g_v/(\pi n_s)^{1/2} a_B$, where n_s is the electron density, a_B the effective Bohr radius, and g_v the valley degeneracy of the host material). There is no agreement on the mechanisms driving the MIT [68], but a number of insulating phases were proposed for clean [49] and disordered systems [56–58].

Here we report on the low temperature magneto-conductance of arsenic- and phosphorus-doped silicon δ-layers at various doping densities near the MIT. Owing to the unprecedented combination of low densities and thinness for such δ-layers in silicon, we are able to access and highlight a new phase dominated by strong Coulomb interactions, where the interaction parameter strength is $r_s \approx 3$. In this system the number of free electrons corresponds to the number of donors, and it is described by a highly disordered half-filled 2D Hubbard model. Recent theoretical studies of the ordered half-filled 2D Hubbard model [73] predict that at low temperature and low interaction strength there is a spinodal crossover from the metallic to the insulating phase with a coexistence region. With the addition of disorder the crossover can be expected to become a first order transition, in agreement with our observation of hysteresis in dilute δ-layers.

Electron-electron interactions in dilute δ-layers

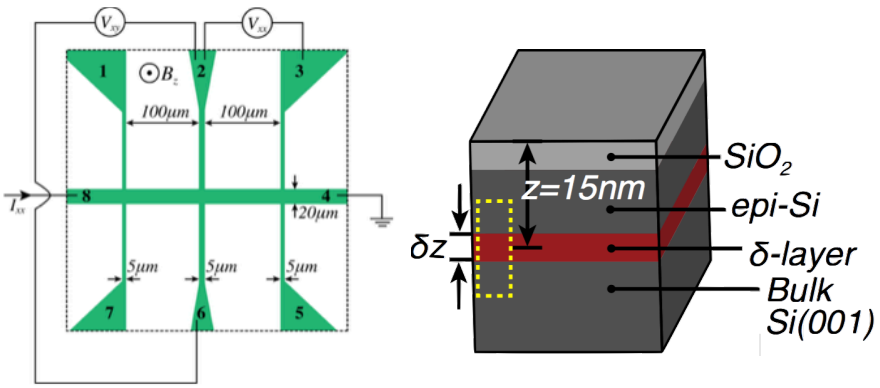

Figure 28: **Sketch of a sample.** On the left, Hall-bar geometry of the contacts allowing for 4 point measurements. On the right, schematic of the sample composition, the arsenic donor layer is encapsulated in the silicon lattice.

The samples studied here are made by gas-phase dosing of dopant precursor arsine (AsH_3) molecules on a Silicon (001) flat surface, followed by homoepitaxial overgrowth of crystalline silicon, then etched into Hall bars, and contacted with aluminium, as shown in Fig. 28. The samples are measured in a dilution refrigerator with a 2 T 4π vector magnet and a 40 mK base temperature. To measure the

longitudinal resistance R_{xx} and the transverse resistance R_{xy} a four-point scheme is used, where a source applies a constant low frequency current (13.7 Hz) and a lock-in amplifier measures the voltage drop across the sample, such that the measured voltage is insensitive to the contact resistance. The arsenic δ-layers have dopant densities ranging from $1{\times}10^{13}$ to $2{\times}10^{14}$ cm^{-2}, and their thickness lies between 0.4 and 1.8 nm, as determined by the magneto-conductance measurements. At these dopant densities the δ-layers are metallic and very close to the metal-insulator transition, which is estimated to be at 1×10^{13} cm^{-2} [86], and the interaction strength parameter r_s goes from 0.8 in the dense layers to 3 in the dilute layers.

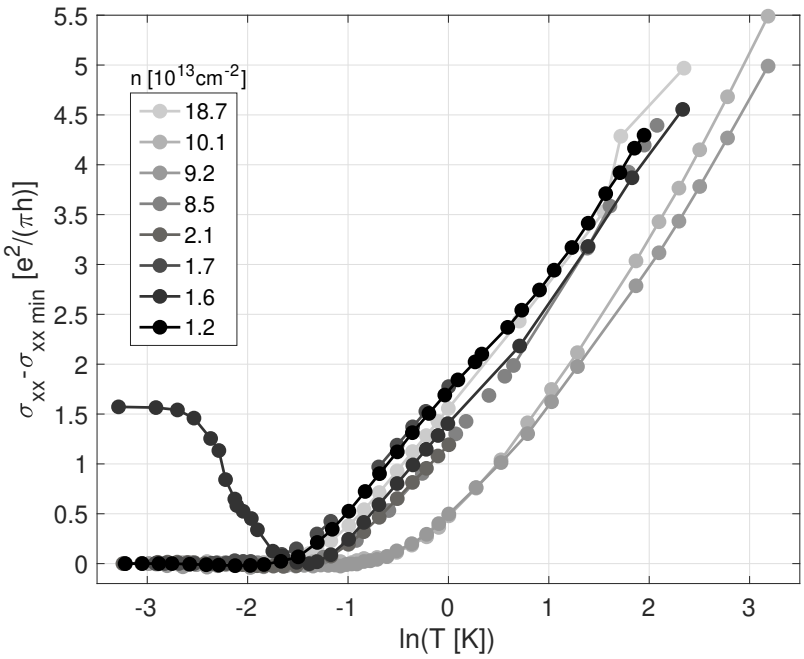

Figure 29: **Logarithmic temperature dependence of the conductivity.** Conductivity of all the studied samples as a function of the temperature, in the absence of magnetic fields, and normalised to the minimum conductivity. The samples' electron density n is indicated in the legend.

The temperature dependence of the samples' longitudinal conductivity σ_0 in the absence of magnetic field, shown in Fig. 29, and Fig. 31b, exhibits two regimes. The conductivity decreases logarithmically with decreasing temperature down to about 300 mK, with a dependence $\sigma_0 \propto \ln T$, but then saturates and stays constant down to the base temperature of 40 mK, except for one sample with electron density $n = (1.61 \pm 0.02) \times 10^{13}$ cm^{-2}. Such a temperature dependence has been observed in many different materials [12, 59–63], but the reasons for the saturation remain a topic of discussion [64]. The logarithmic regime at higher temperatures combined with the conductance being larger than the quantum

of conductance $\sigma_0 > e^2/h$ is an indication that the transport is diffusive, for which weak-localisation (WL) effects can be expected [35]. Weak-localisation is a quantum correction to the Drude conductivity that stems from the interference of diffusive electrons with themselves through self-intercepting loops. For weak-localisation to arise the electron coherence length L_ϕ must exceed the mean free path L, which sets the scale of the smallest loops, and it is strongest if time reversal symmetry is not broken. When a magnetic field is applied, the time-reversal symmetry is broken as the field couples to the electron's orbital motion. For a two-dimensional conduction layer with the field perpendicular to the layer, the ensuing change in conductivity is given by the equation derived by Hikami, Larkin and Nagaoka [6]:

$$\Delta\sigma(B_\perp) = \left(\frac{e^2}{2\pi^2\hbar}\right)\left[\psi\left(\frac{1}{2}+\frac{\hbar}{4eL_\phi^2 B_\perp}\right) - \psi\left(\frac{1}{2}+\frac{\hbar}{2eL^2 B_\perp}\right) + \ln\left(\frac{2L_\phi^2}{L^2}\right)\right], \tag{13}$$

where $\psi(x)$ is the digamma function, L is the mean free path, L_ϕ is the coherence length, $\hbar$ is the reduced Planck constant, and e the electron charge. If the layer has a finite thickness d, a magnetic field applied in the conduction plane will still have a small orbital effect that depends on the thickness of the layer through a single parameter γ [150],

$$\Delta\sigma(B_\parallel) = \left(\frac{e^2}{2\pi^2\hbar}\right)\ln(1+\gamma B_\parallel^2). \tag{14}$$

Where the thickness d is related to γ as $\gamma = d^2\sqrt{\frac{4\pi}{n}}\left(\frac{e}{\hbar}\frac{L_\phi}{\sqrt{L}}\right)^2$.

Figure 30 shows the typical in-plane and out-of-plane magneto-conductance obtained at 115 mK. At this temperature and sample density ($n = (1.18\pm\ 0.01)$ $\times\ 10^{13}$ cm^{-2}) the magneto-conductance is negative. This cannot be explained by weak-localisation, nor can the data be fit with weak-anti-localisation [162], nor with Minkov et al.'s model which includes Rashba and Dresselhaus spin-orbit interaction [14, 21, 22], as could be expected for samples with large spin-orbit coupling. We find instead, that the magneto-conductance corrections are governed by two effects that add up in conduction, as two channels in parallel: $\Delta\sigma_{xx}^{\mathrm{tot}} = \Delta\sigma_{xx}^{\mathrm{WL}} + \sigma_{xx}^{\mathrm{Zeeman}}$ [31, 163]. The first effect $\Delta\sigma_{xx}^{WL}$ is conventional weak-localisation as described in Eq. (13) and Eq. (14). The second effect $\Delta\sigma_{xx}^{Zeeman}$ is the Zeeman effect on the conductivity as described in 1982 by Lee and Ramakrishnan [31]:

$$\Delta\sigma(h) = -\frac{e^2}{\hbar}\frac{F}{4\pi^2}\ln\left(\frac{h}{1.3}\right),\ \text{for } h \gg 1, \tag{15}$$

where $h = \frac{g\mu_B B}{k_B T}$ is the reduced field, and F is a constant (the angular average of the statically screened Coulomb interaction). The effect scales as $\ln(B/T)$, meaning that it becomes strong for low temperatures.

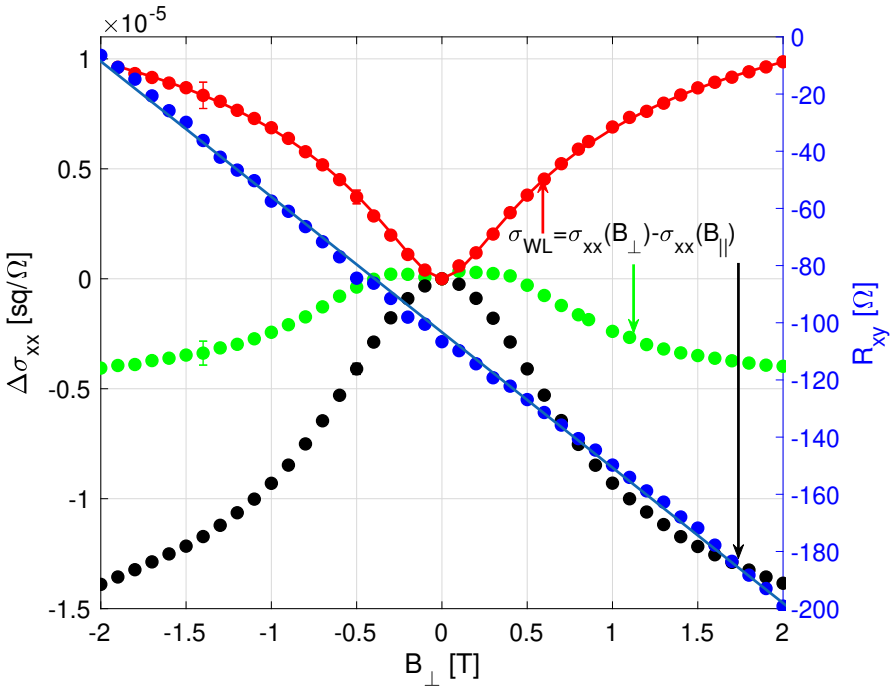

Figure 30: **Typical magneto-conductance measurements.** At $T = 115$mK, the magnetic field is set parallel to the plane of the δ-layer (black points - with no dependence on the relative orientation to the current) and perpendicular to it (green points). The red points are the difference between in and out of plane magneto-conductance, the solid red line being a fit to weak-localisation corrections Eq. (13) and Eq. (14). The sample's electron density is $n = (1.18 \pm 0.01) \times 10^{13}$ cm^{-2}. The blue data is a typical Hall measurement (R_{xy}) taken at 1.75 K, with the solid line being a linear fit, consistent with the dopant density.

The Zeeman effect couples the magnetic field to the spin of the electrons, and thus (to the extent that spin orbit coupling does not interfere) is isotropic in the direction of the magnetic field, unlike weak-localisation that couples to the orbital motion [59]. We can isolate the anisotropic WL contribution by taking the difference between the out-of-plane and in-plane magneto-conductance, as shown in Fig. 30 (red dots), and Fig. 31a where the full lines are fits to the weak-localisation expression Eq. (13) from which Eq. (14) has been subtracted. In figure 31b the blue points are the coherence length obtained from the fits at different temperatures, exhibiting the expected power law behaviour [13]. Note that to fit these curves only the coherence length L_ϕ and the thickness parameter γ are free parameters. The mean free path L, the free carrier density and mobility are all obtained from Hall measurements at high temperatures (2 K), as shown in Fig. 30 in blue. In particular there is no need for a global free fitting prefactor to Eq. (13) as is often used but not justified for similar data [36, 135]

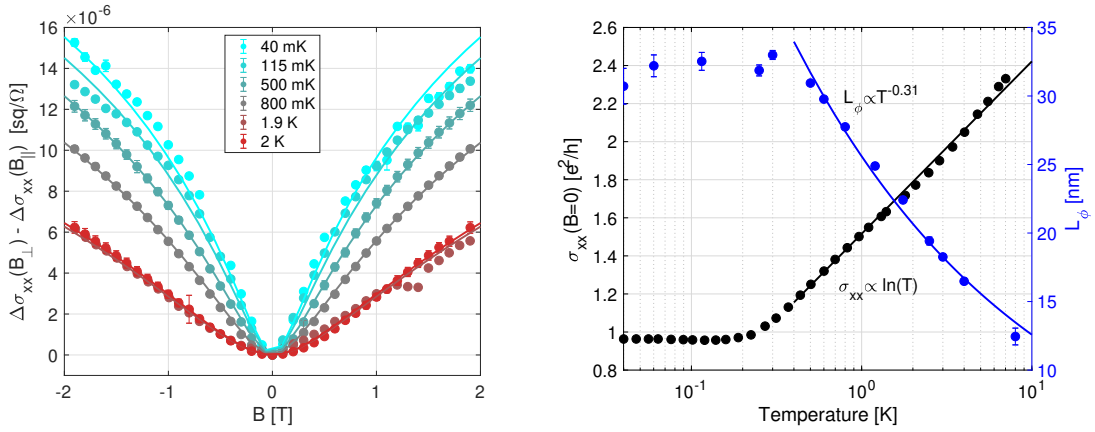

(a) (b)

Figure 31: **Extracted weak-localisation contribution.** (a) Difference between the magneto-conductance with the field out-of-plane and in-plane for various temperatures in a sample with density $n = (1.18\pm0.01)\times10^{13}$ cm^{-2}. The solid lines are fits to the Eq. (13) minus Eq. (14). (b) Conductivity versus temperature in black, displaying a logarithmic dependence as expected for weak-localisation down to $T_{crossover}$ ≈300 mK. The coherence length L_ϕ obtained from the fits in (a) is shown in blue. It follows a power law $T^{-0.31}$ down to T≈300 mK.

(though for $\sigma_0 \lesssim 10G_0$ it can be justified by considering the two-loop localisation correction [89,90]). We find that for thicker and denser samples, the out-of-plane magneto-conductance data can erroneously be fitted only to weak-localisation if one uses a free pre-factor, because the Zeeman effect is small. However, if one removes the Zeeman effect one does not need to add an extra parameter to the fit. From the parameters obtained from these fits it is possible to calculate the thickness of the dopant layer [151], which is 0.65±0.05 nm for the sample shown in Fig. 31, and between 0.4 and 1.8 nm for the arsenic δ-layers studied in this work, thinner than what has been obtained in phosphorus doped Si [87, 164], as is expected due to arsenic's lower diffusion during annealing steps of the sample fabrication. In the thinnest layer only three Si(100) crystal planes are conductive, compared to thirteen in the thickest layer.

The weak-localisation effect calculated in Eq. (13) is given by an expansion in $k_F L$, where k_F is the Fermi momentum of the electrons and is inversely proportional to the square root of the dopant density. As such, for samples with different densities, the parameters related to the weak-localisation effect scale with $k_F L$, as is the case for the perpendicular magneto-conductance and its intensity at 2 T, shown in Fig. 32 and Fig. 33a. The Zeeman effect depends on the Coulomb interaction, which is proportional to the ionisation energy over the donors' wave-functions overlap integral, such that it is stronger for lower free carrier densities. For in-plane magnetic fields, when the δ-layer is thin enough

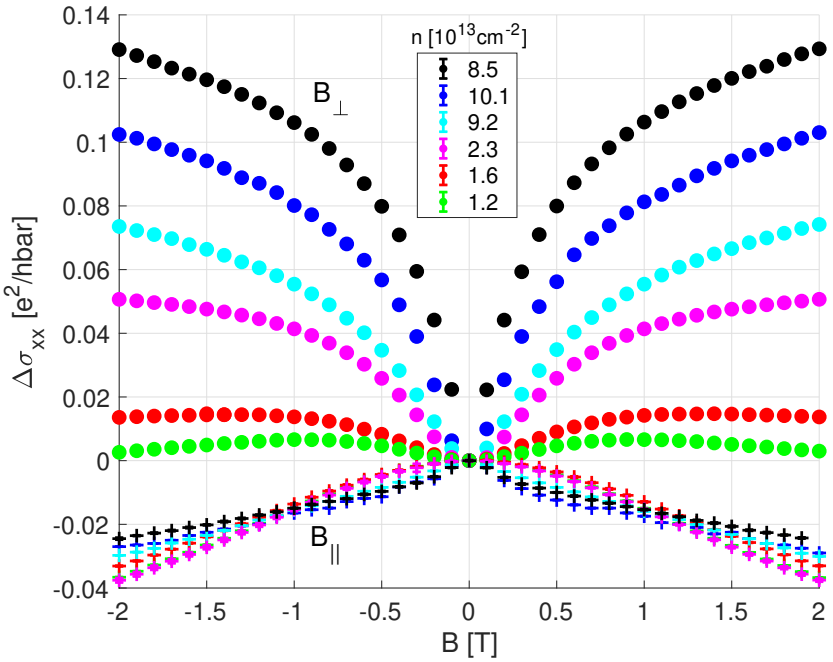

Figure 32: **Influence of density on the magneto-conductance.** Magneto-conductance at 600 mK for samples with different free carrier densities n. As the density decreases the effect of the perpendicular magnetic field (full dots) becomes smaller, whereas the effect of the in-plane magnetic field (crosses) becomes stronger.

and/or dilute enough, the Zeeman effect competes with the weak-localisation. This is the case for our arsenic δ-layers, as is visible in Fig. 32.

To isolate the Zeeman effect we remove the weak-localisation's contribution to the magneto-conductance as determined by the fits shown in Fig. 30 and Fig. 31a. The remaining magneto-conductance is found to follow Eq. (15), in particular it scales as $\ln(g\mu_B B/k_B T)$. Figure 33b shows that the absolute value of the change to the conductivity due to the Zeeman effect at a field such that $\ln(g\mu_B B/k_B T) = 1$ (black data) is a function of the sample's dopant density. This is expected because the term F in Eq. (15) depends on the average Coulomb interactions, which depend on the density dependent electron screening effect. In figure 33b on the right y-axis, $k_F L$ is shown as a function of sample density. Note that if the roughness and disorder of the dopant layers does not vary much from sample to sample, then $k_F L$ increases monotonically with the density and makes it look like the weak-localisation effect is governed by density rather than $k_F L$, as is the case in [135]. In our samples $k_F L$ is not a monotonic function of the density allowing us to distinguish the effects that scale with the density (the Zeeman effect) from the effects that scale with $k_F L$ (the weak-localisation effect).

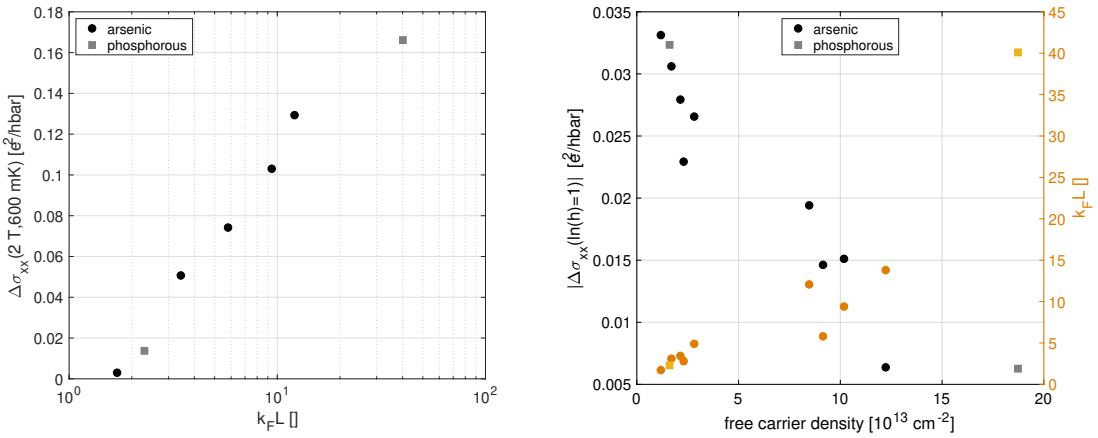

(a) (b)

Figure 33: **Magnitude of the weak-localisation and Zeeman effects.** (a) Magnitude of the magneto-conductance at 600 mK in a 2 T perpendicular magnetic field as a function of $k_F L$, showing that the out-of-plane magneto-conductance is governed by weak-localisation, the amplitude of which depends on $k_F L$ rather than the density. (b) Magnitude of the Zeeman effect versus free carrier density in black on the left y-axis. The magnetic field was adjusted such that $\ln(g\mu_B B/k_B T) = 1$. The Zeeman effect scales with the free carrier density rather than with $k_F L$ (shown in orange with labels on the right y-axis). In (a) and (b) the dots correspond to arsenic δ-layers while the squares are from phosphorus δ-layers, showing that the magneto-conductance does not depend on the dopant species.

The data shown in Fig. 33 also contains data from phosphorus δ-layers (squares), showing that the effects depend predominantly on the dopant density or $k_F L$, but not on the dopant species.

The strength of the Zeeman effect depends on the interaction parameter F in Eq. (15). The same parameter can be extracted from the conductivity's temperature dependence, shown in Fig. 29, which is of the form $\sigma_0 \propto (1 + \kappa_{ee}) G_0 \log T$, with $G_0 = e^2/(2\pi^2\hbar)$ and $\kappa_{ee} = 1 - F/2$. Figure 34a shows κ_{ee} as a function of the electron density obtained from the conductivity's temperature dependence and the Zeeman effect. The two methods give very similar values and the same trend of larger F (lower κ_{ee}) for lower densities, as expected because of reduced screening. Nonetheless, as is visible in Fig. 34b, κ_{ee} obtained from the magnetic field dependence is consistently (with one exception) larger than when it is obtained from the temperature dependence.

The Zeeman effect on the conductivity, Eq. (15), is a logarithmic function of the reduced field $h = \frac{g\mu_B B}{k_B T}$. Therefore, when the Zeeman contribution to the magneto-conductance is plotted against the reduced field h at different temper-

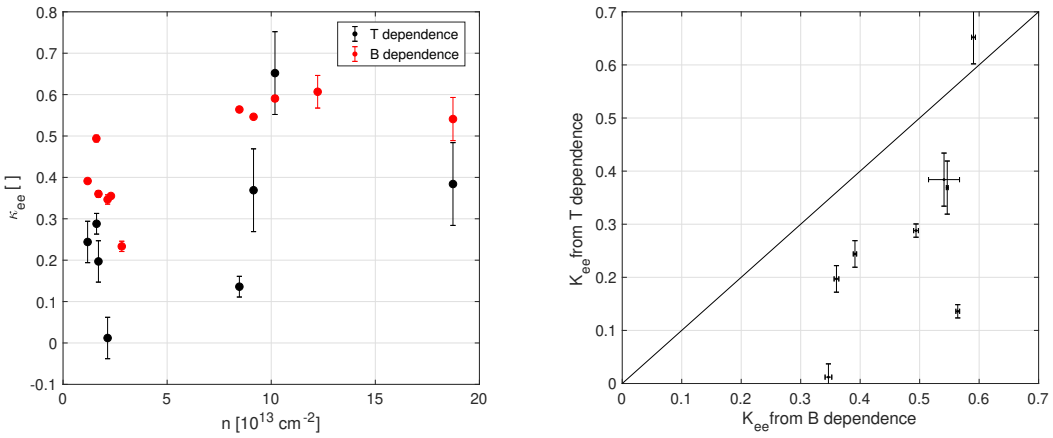

(a) (b)

Figure 34: **Interaction effects on the temperature and magnetic field dependence.** (a) Electron-electron interaction parameter κ_{ee} as a function of sample electron density n. The parameter κ_{ee} extracted from the conductivity's temperature dependence and the in-plane magneto-conductance is shown in black and red, respectively. (b) κ_{ee} extracted from the temperature dependence against κ_{ee} extracted from the magnetic field dependence.

atures, the data should collapse to a single curve. This is shown in Fig. 35a for a sample with density $n = (2.14 \pm 0.02) \times 10^{13}$ cm^{-2}, where a clear collapse of the data is seen down to 250 mK. In figure 35b the same data are shown, but instead of the phonon temperature an effective electron temperature was used to obtain a collapse down to the fridge's base temperature. The effective temperatures used for the various samples to obtain the collapse are shown in Fig. 35d. Interestingly the conductivity σ_0 and coherence length L_ϕ in Fig. 31b follow the same trend as the Zeeman effective temperature, namely at $T_{crossover}$ $\approx$ 250 mK they stop being temperature dependent, as if the samples stopped thermalising. However, although L_ϕ and σ_0 are constant below $T_{crossover}$, other effects start to become visible as the samples are cooled even more, showing that the sample temperature is still falling, at least in some part of the sample. In particular, at $T_{crossover}$ the transverse voltage response starts to become non-linear as a B-symmetric transverse voltage V_{xy} emerges for all magnetic field directions (Fig. 36a and Fig. 36b). At the same time hysteresis in the longitudinal and transverse magneto-conductance (Fig. 42a) appears with a maximum amplitude around $T_{crossover}$. These effects can be qualitatively explained by the formation of a phase with an inhomogeneous conductance, *i.e.*, a mixture of insulating and conductive regions.

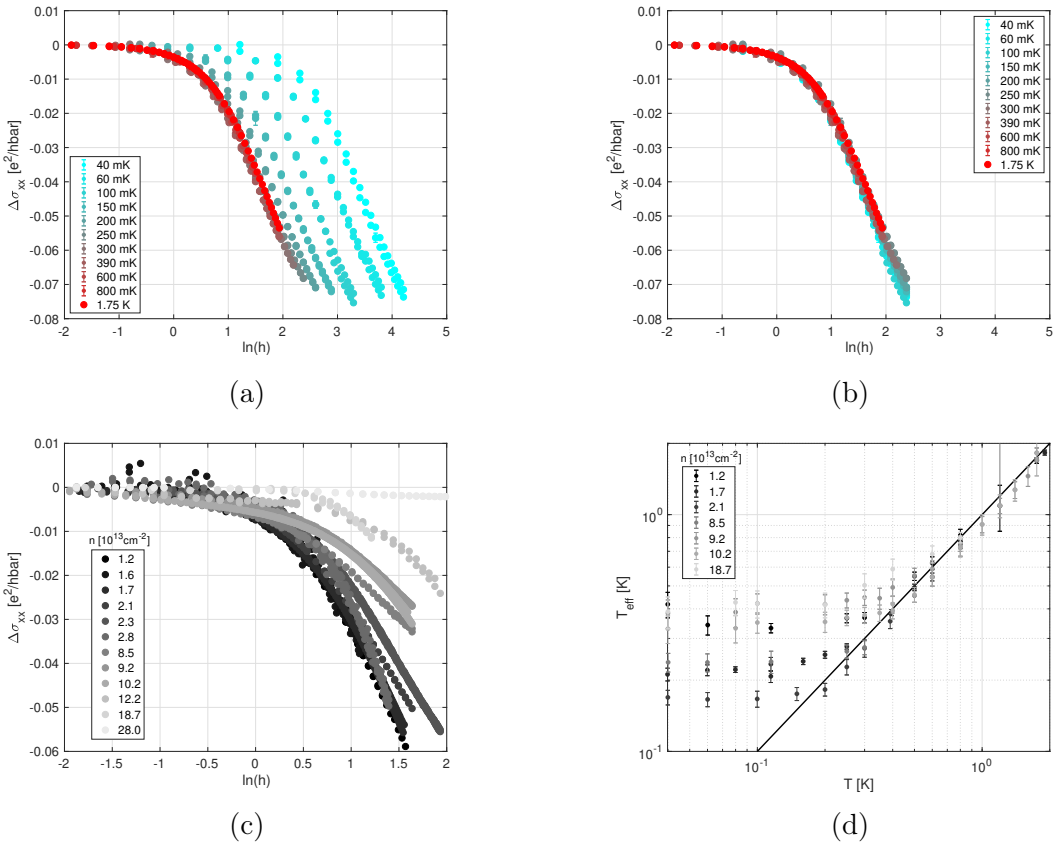

Figure 35: **Zeeman effect B/T scaling.** (a) Change in conductivity due to the Zeeman effect in units of the conductance quantum $e^2/\hbar$, as a function of the logarithm of the reduced field $h = g\mu_B B/k_B T$. The data is shown for multiple temperatures and is from a single sample with free carrier density $n = (2.14 \pm 0.02) \times 10^{13}$ cm^{-2}. The data collapse down to 250 mK. (b) Same as in (a), except that an effective temperature T_{eff} is used to obtain a full collapse of the data. T_{eff} is plotted for all samples in (d). (c) Zeeman effect for all samples. The effect is stronger for lower free carrier densities (darker colour). (d) Effective temperature T_{eff} determined for all samples to collapse the Zeeman effect as in (a) and (b).

Low temperature inhomogeneous phase: Transverse voltages

Below the transition temperature $T_{crossover}$ two unexpected effects are visible for low density samples. The first is a transverse voltage V_{xy} created by a magnetic field in any direction. This anomalous V_{xy} effect only arises for temperatures lower than $T_{crossover}$ as is seen in Fig. 36 and Fig. 37a for a sample with a density $n = (1.18 \pm 0.01) \times 10^{13}$ cm^{-2}. It is even in magnetic field; its amplitude increases by three orders of magnitude as $k_F L$ and the free carrier density decrease, and is non-existent for high $k_F L$ and density, as is shown in Fig. 37b. In the lowest

density sample ($n = (1.18\pm\ 0.01) \times 10^{13}$ cm^{-2}), the transverse voltage V_{xy} in the absence of magnetic field is non zero below $T_{crossover}$, visible in Fig. 37a. The appearance of a large transverse V_{xy} in the absence of noticeable changes in longitudinal V_{xx} cannot be explained by lead misalignment (see appendix A.3).

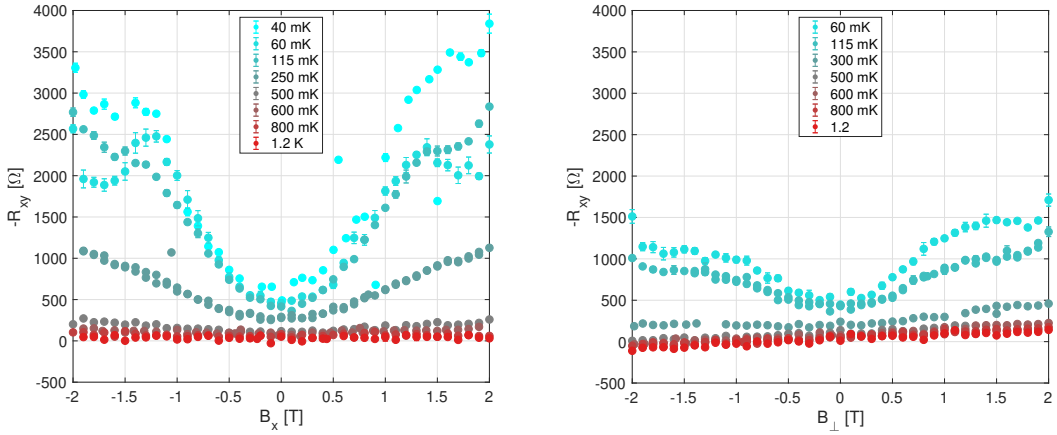

(a) (b)

Figure 36: **Anomalous transverse resistance in magnetic fields.** Transverse resistance ($R_{xy} = V_{xy}/I$) in presence of an in-plane magnetic field in (a) and an out-of-plane magnetic field in (b) for a sample with a free carrier density of $n = (1.18\pm\ 0.01) \times 10^{13}$ cm^{-2} at various temperatures. When the bath temperature falls below $T_{crossover} \approx 250$ mK, a transverse voltage even in the B-field appears. The y-scale on both (a) and (b) are the same to highlight the weaker R_{xy} effect in the out-of-plane field.

The second unexpected effect visible below the transition temperature $T_{crossover}$ is a hysteresis in the magneto-conductance with a butterfly shape, shown in Fig. 42a. The area of the hysteresis loop as a function of temperature has a maximum at $T_{crossover}$ and vanishes at higher and lower temperatures, as can be seen for a sample with $n = (1.18\pm\ 0.01) \times 10^{13}$ cm^{-2} in Fig. 42a. Here again, the density plays an important role to the anomalous Hall effect and the hysteresis, which are stronger for lower density samples. The hysteresis is visible with the same relative strength in both the longitudinal V_{xx} and transverse V_{xy} voltages and for all field directions, already indicating a mixing of V_{xx} and V_{xy} due to the formation of an inhomogeneous conductive phase.

The low-temperature effects might be explained similarly to Kapitulnik, Kivelson and Spivak's failed superconductors theory [64], in which superconducting grains form within a conductor and fail to establish global superconducting coherence. In our case it is a failed insulator, the idea being that for temperatures below $T_{crossover}$, the 2D metallic layers undergo a crossover to a state where there are insulating puddles in a metal, as has often been suggested [58, 165–167]. This

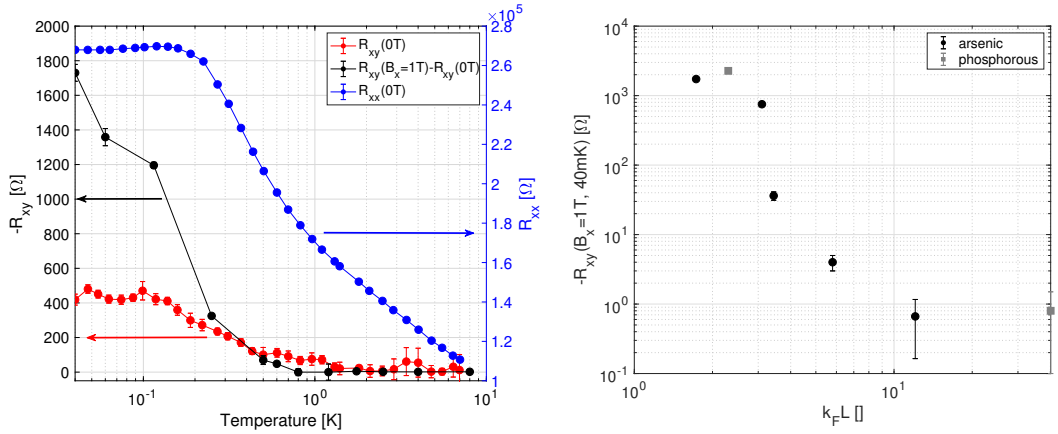

(a) (b)

Figure 37: **Temperature and density dependence of the anomalous transverse resistance.** (a) Temperature dependence of R_{xy} and R_{xx} in a sample with $n = (1.18 \pm 0.01) \times 10^{13}$ cm^{-2}: In black, the change in R_{xy} induced by a 1 T in-plane magnetic field ($R_{xy}(B_x = 1T) - R_{xy}(B = 0T)$). In red, R_{xy} in the absence of magnetic field. Both values show a strong increase at low temperatures. The sign of R_{xy} is set such that the Hall effect at higher temperature has a negative slope. In blue, R_{xx} in the absence of magnetic field, R_{xx} and R_{xy} do not have the same temperature dependence. (b) Change in R_{xy} at $B = 1$ T (in plane) and $T = 40$ mK as a function of $k_F L$. The dots indicate data from arsenic samples and the squares from phosphorus samples. The effect depends only on $k_F L$ (or density), but does not depend on the dopant species.

is likely to happen because the samples are near the metal-insulator transition. The metallic part is responsible for the conduction and is affected by weak localisation and the Zeeman effect, however the localisation strength becomes limited by inelastic scattering on the insulating puddles, such that it saturates at low temperatures. On the contrary, the insulating puddles do not participate directly in transport, but rather act as highly resistive inclusions that force the current to flow around them. In this picture, especially in the limit when the insulating inclusions are relatively dense and thus nearly interrupt the percolation of metallic parts, the conductivity becomes anisotropic, such that the current does not necessarily follow a straight path, as was shown by Parish and Littlewood [168]. This leads to non-zero transverse voltages V_{xy}, which depend on the meandering paths followed by the electrons. The transverse voltage V_{xy} is very sensitive to local variations along Hall bar's edges, while the longitudinal voltage V_{xx} depends on the mean of all current paths and is much less sensitive to small changes. This can explain why V_{xy} saturates at lower temperatures than V_{xx}. The insulating inclusions are present even in denser samples because of the high disorder, however their size and number is lower, such that they limit the the coherence

times and lead to the observed temperature saturation without causing detectable inhomogeneous conduction and perpendicular voltages.

The extreme case of such an inhomogeneous conductor would be that there is only one 1D conducting wire within the dopant layer. In that case, pictured on Fig. 38, the 1D conducting wire might follow a straight line across the layer (Fig. 38a), or a random zigzag trajectory (Fig. 38b). In the former case, the transverse voltage V_{xy} would be zero and the longitudinal voltage V_{xx} should be quantised. If the wire were quasi-1D, no quantisation of the conduction would be visible, but the magneto-resistance should reflect the anisotropy and be strongest when the magnetic field is parallel to the wire, such that it can couple to the electrons' orbital motion. In the latter case, as illustrated in Fig. 38b, the transverse voltage V_{xy} can be mixed with the longitudinal voltage V_{xx}, and be non-zero even in the absence of magnetic fields. If the 1D wire follows a sufficiently random path, the planar magneto-resistance might be isotropic, as electrons move in all directions in the plane. However, in the case of a single wire, V_{xy} would be exactly proportional to V_{xx}, simply by a factor determined by the length of the wire in-between the contacts, which disagrees with our measurements (see also appendix A.3).

An inhomogeneous conductor could also be composed of multiple 1D wires, which might be short, *i.e.*, constrictions between insulating islands could force the electrons to pass through locally 1D regions. When the number of such 1D wires (or quasi 1D) is not too large (at low densities), there can still be a mixing of V_{xy} and V_{xx} such that V_{xy} is non-zero. A magnetic field increases the number and size of insulating regions, leading to an increase of regions with constricted current flow (1D wires), and consequently to an increased mixing of V_{xy} and V_{xx}. As a result, when a magnetic field is swept, V_{xy} changes more than V_{xx}, although it is always only a part of V_{xx}, *i.e.*, $V_{xy} = \alpha(B)V_{xx}$ with $\alpha(B) \propto B^2$ in our samples.

In the failed insulator picture, the inhomogeneity is linked to the disorder and the varying local dopant distribution. At lower densities it is more likely that a region becomes insulating. Thus, the inhomogeneity should be a continuous function of the decreasing density, and it should have a random distribution. The picture of a few current paths is certainly exaggerated, particularly at relatively high densities. However, even in the case of a random array of resistors there are preferential current paths, as shown by Parish and Littlewood [169]. Figure 39 shows a result from their simulation of an array of 20×20 2D resistors, in which the arrows indicate the direction and the amplitude of the current flow, and the colour-scale is the associated local voltage. They simulated a uniform resistor network, Fig. 39.a, and a random resistor network, Fig. 39.b, in the presence of a perpendicular magnetic field. In the random network, the current creates loops and has a strong local variability, and the ensuing voltage displays strong

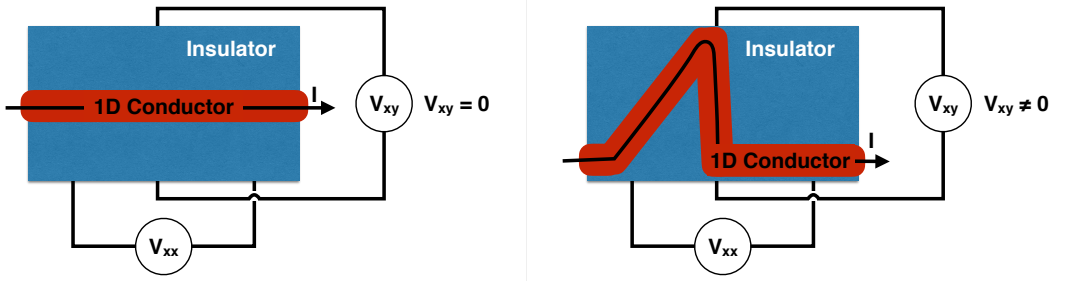

(a) (b)

Figure 38: **V_{xy} in a 1D wire within a 2D layer.** (a) The conducting part of the dopant layer is limited to a straight 1D wire and the voltage $V_{xy} = 0$ V. (b) The conducting part of the dopant layer is a zigzagging 1D wire and the voltage $V_{xx} = \alpha V_{xx}$, with α given by the geometry.

anisotropy. It is visible in Fig. 39.b that there is an anomalous V_{xy} in the random network due to the filamentary current flow. However the exact influence of the inhomogeneity on V_{xy} could not be extracted from such small networks, because V_{xy} has a too strong local variation. Nonetheless, these results are relevant to our disordered electron layers near the MIT, as they show that a random local variation of the resistance naturally leads to anomalous transverse voltages V_{xy}.

The proposed inhomogeneous phase can qualitatively explain the observed magnetic-field-symmetric V_{xy} (Fig. 36), its dependence on the sample's electron density, and its temperature dependence (Fig. 37). In this scenario, the measured V_{xy} should depend on the location it is measured at, and the sign of the voltage V_{xy} should be random from location to another. In figure 40 we show results from the sample with electron density $n = (1.70 \pm 0.04) \times 10^{13}$ cm^{-2}. In both plots, two resistances, $R_{xy,1}$ (black) and $R_{xy,2}$ (red), are shown as a function of the magnetic field out-of-plane (crosses) and in-plane (dots). $R_{xy,1}$ is measured on the centre of the Hall bar (Fig. 28 contacts 2-6) and $R_{xy,2}$ on the side (Fig. 28 contacts 1-7). At 40 mK, Fig. 40a, the results on $R_{xy,1}$ and $R_{xy,2}$ are entirely different, most notably the sign of the measured voltage in planar fields is opposite, and the magnitude of the effect has a factor two difference. At 500 mK, Fig. 40b, the results are much more alike for both $R_{xy,1}$ and $R_{xy,2}$, in particular the sign of the effect is the same. These results are in line with an increasing inhomogeneity in the sample for decreasing temperatures.

The change of sign of $R_{xy,2}$ observed in Fig. 40, is also shown in Fig. 41. As mentioned, the effect of a planar magnetic field on $R_{xy,2}$ changed sign upon warming the sample from 40 mK to 500 mK, as is visible in Fig. 41a. Under the assumption that the effect is due to inhomogeneous resistance in the sample, we

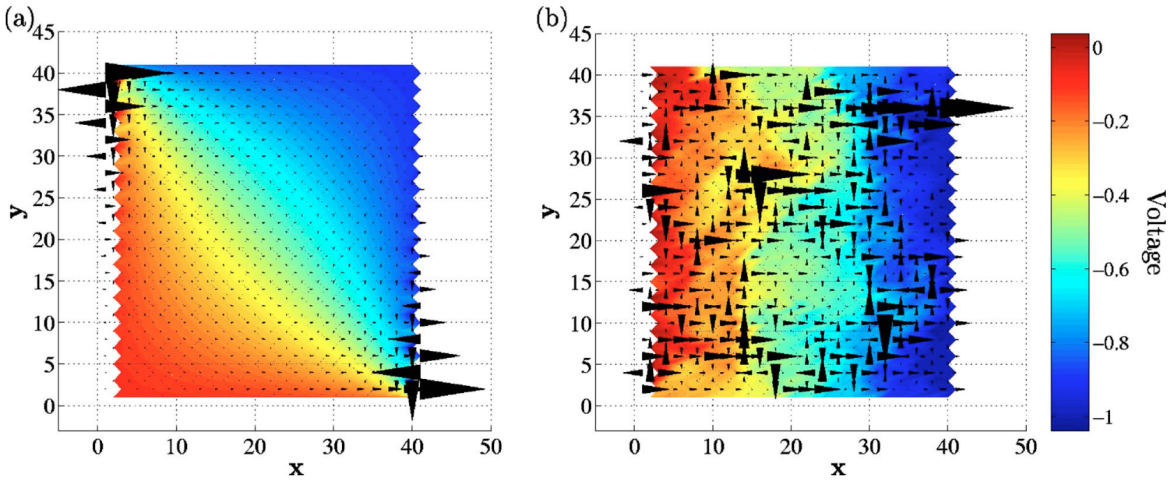

Figure 39: **Inhomogeneous network of resistors simulation.** Simulation from [169]. A potential difference of 1 V is applied from the top left to the bottom right corner of the sample. The current directions and amplitudes are indicated by the arrows and their thickness, respectively. The colour-scale shows the local voltage. (a) A uniform 20×20 network. (b) A random 20×20 network.

could suspect that the exact distribution of insulating and conducting regions is history dependent, and specifically dependent on the applied magnetic field while cooling or warming the sample. The events leading to the sign change of $R_{xy,2}$ are shown in Fig. 41b, in an H_x-T plane, where H_x is the in-plane field parallel to the current. Initially H_x was set to 2 T at 800 mK, whereupon the temperature was lowered to 40 mK, and an H_x field sweep from 2 T to -2 T gave the negative effect in $R_{xy,2}$. Subsequently, the temperature was raised to 500 mK with the field still at -2 T, and H_x was swept from -2 T to 2 T, resulting in the positive $R_{xy,2}$ effect. Thus, the direction of the B_x magnetic field while thermalising the sample could have influenced the formation of the random low temperature phase. Here, we need remind that while the effect of H_x on $R_{xy,2}$ changed sign, it remained the same on $R_{xy,1}$, and we have to specify that such a change of sign was observed only in one sample out of five. However, the experiments were not conducted specifically to look for this effect; in particular we did not try to magnetise the samples by cooling from high temperatures (>1 K) with a magnetic field, which will be done in future experiments.

The sign of V_{xy} in planar magnetic fields has been observed to change upon warming the $n = (1.70 \pm 0.04) \times 10^{13}$ cm^{-2} sample from 40 mK to 500 mK, suggestive of a random time reversal symmetry breaking in the sample. In the same sample, the sign was seen to be different when measured on different V_{xy} contacts, indicating a strong local variability, as can be expected in a strongly inhomogeneous conductor. However, these observations were only made in one sample,

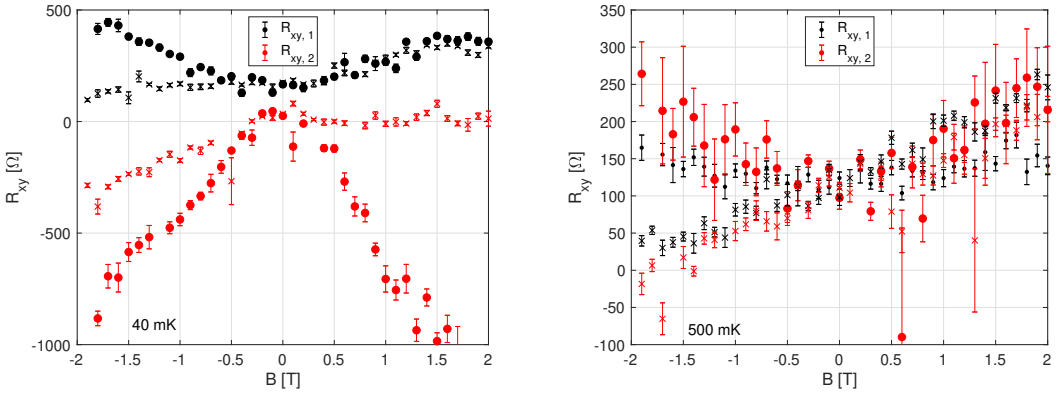

(a) (b)

Figure 40: **Local variability of the anomalous transverse resistance.** (a) The transverse resistance as a function of magnetic field at 40 mK measured on two different pairs of contacts, $R_{xy,1}$ and $R_{xy,2}$, on the same sample ($n = (1.70 \pm 0.04) \times 10^{13}$ cm^{-2}). At 40 mK $R_{xy,1}$ and $R_{xy,2}$ are very different because of strong sample inhomogeneity. (b) The same as in (a) at 500 mK.

and the other four samples with noticeable planar V_{xy} effect had consistently the same negative sign in V_{xy} (the same sign as in the Hall effect when a positive perpendicular magnetic field is applied). The odds of seeing four times the same V_{xy} sign in response to a magnetic field if it were random are of 12.5%. However, if the sign were not random, to account for this observation it would be necessary for the time reversal symmetry to be broken consistently in the same biased fashion, namely such that it results in an effective upwards pointing magnetic field. For example, one could suspect the Rashba spin-orbit effect originating from the asymmetry of the donors' vertical confinement (see appendix A.5) to contribute to V_{xy}. Time reversal symmetry has been reported to be broken by Coulomb interactions in low density phosphorus δ-layers in silicon and germanium [36], in that case the direction is random as it is the case in inhomogeneous conduction and would not explain the possibly consistent sign of V_{xy}. The measured voltage in the doping layers is given by

$$V_a = \sum_b R_{ab}(B) I_b, \tag{16}$$

where, in two-dimensions, the indices a and b are the x and y axis and R_{ab} is a two-by-two matrix. The resistance matrix must satisfy Onsager's reciprocity,

$$R_{xy}(B, M) = R_{yx}(-B, -M), \tag{17}$$

where M is magnetisation. Onsager's reciprocity implies that the symmetric part of R, $(R_{xy} + R_{yx})/2$, is even under inversion of the field and magnetisation, $(B, M) \Leftrightarrow (-B, -M)$, while the antisymmetric part, $(R_{xy} - R_{yx})/2$, is odd and

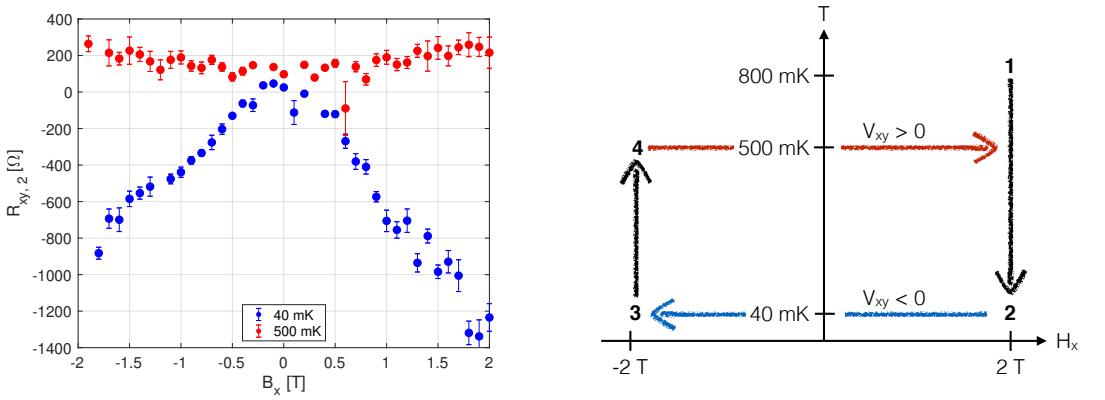

(a) (b)

Figure 41: **Transverse voltage sign in the H_x-T plane.** (a) The transverse resistance $R_{xy,2}$ as a function of planar magnetic field at 40 and 500 mK, from the sample with $n = (1.70 \pm 0.04) \times 10^{13}$ cm^{-2}. The sign of $R_{xy,2}$ changed upon warming. (b) H_x-T trajectory for the measurement in (a). The bold numbers indicate the chronological order.

requires time reversal symmetry breaking. Thus, the observed even in magnetic field R_{xy} is the symmetric part of R, or if there is a stable internal magnetisation M breaking time reversal symmetry, it can be part of the Hall part of R. If time reversal symmetry is not broken (M=0), and R_{xy} is even in B, Onsager's relations imply $R_{xy} = R_{yx}$, and the measured sign of R_{xy} has to depend on the directions of the measurements. If instead time reversal symmetry is spontaneously broken, the ensuing Hall effect (antisymmetric part of R_{xy}) is an even function of B, but reflects the arbitrary sign of the spontaneous magnetisation and thus is again random. Altogether, it seems most likely that the planar R_{xy} effect has a random sign. If R_{xy} were the symmetric part of R caused by inhomogeneity it would be resilient to thermal cycles, while if it were the Hall part due to a magnetisation it should vary upon thermal cycling.

Low temperature inhomogeneous phase: Hysteresis

Recent calculations for the translationally invariant, non-disordered 2D Hubbard model [73] predict that near the MIT the metallic phase has a higher entropy than the insulating phase, such that, if the insulating phase has a lower internal energy than the metallic phase, lowering the temperature or applying a magnetic field in any direction favours the insulator and increases the number of insulating inclusions. The isotropic response to magnetic fields explains the observed even V_{xy} effect and hysteresis. If the transition is first order, as expected for high disorder, then it takes a long time to nucleate the flip to the more stable insulat-

ing phase, leading to hysteresis in the magneto-conductance. When a magnetic field is applied, polarisation of the spins promotes the insulating phase, resulting in an increase of insulating regions. When the field is removed, the newly created insulating regions progressively re-become metallic, resulting in the observed butterfly-shaped hysteresis.

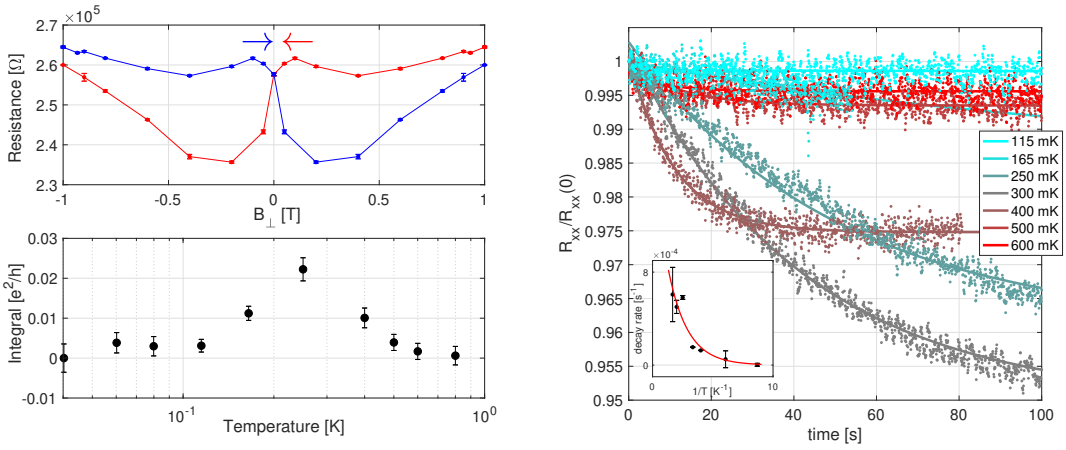

(a) (b)

Figure 42: **Magnetic field induced hysteresis.** (a) Top: example of the hysteresis in longitudinal magneto-conductance seen in low density samples at $T_{crossover} = 250$ mK for a sample density $n = (1.18 \pm 0.01) \times 10^{13}$ cm^{-2}. Bottom: temperature dependence of the area of the hysteresis loop, showing that the hysteresis is most visible around $T_{crossover}$. (b) Time traces taken immediately after sweeping the magnetic field from $B_\perp = 1.6$ T to 0.1 T, for many temperatures indicated in the legend. The points are data, and the lines are fits to an exponential decay function $\exp -t/\tau$. The inset shows the decay rate τ as function of the inverse temperature.

The hysteresis is due to a slow relaxation time from a more insulating state to a more conductive state, as can be seen by sweeping the field from 1.6 T to 0.1 T, and measuring the resistance as a function of time, as is done in Fig. 42b. At temperatures higher but close to $T_{crossover}$ a fast decay to a constant resistance is observed. As the temperature reaches $T_{crossover}$ the decay is slow and the final resistance is not reached within 100 s. For even lower temperatures, the decay time becomes very long, such that the change in resistance is barely detectable in 100 s, explaining the apparent disappearance of the hysteresis at low temperatures in Fig. 42a. The decay rate τ is obtained by fitting the time traces with an exponential decay of the form $\exp -t/\tau$. The temperature dependence of τ is shown in the inset of Fig. 42b in an Arrhenius plot, highlighting that the dynamics of the hysteric phase slows down with decreasing temperatures to the point that it becomes a glassy metallic phase, as was also seen in Si MOSFETs near the MIT [68, 69].

The observation of hysteresis is suggestive of a first order phase transition tuned by the magnetic field. However, in the case of an inhomogeneous material, one would rather expect a stretched exponential time decay composed of multiple decay times, reflecting the multitude of regions with different activation energies. The Arrhenius plot gives a single activation energy of the order of 600 mK, which corresponds to the temperature at which the hysteresis starts to be visible, and points to an energy barrier associated with spin-orbit coupling through the antisymmetric Dzyaloshinskii–Moriya (DM) exchange interaction. In the case of broken spatial inversion symmetry, neighbouring spins pointing in different directions can interact through the antisymmetric DM interaction (of the form $H_{DM} = \alpha J(S_i \times S_j)$), with an interaction strength αJ, where $J = t^2/U$ is the exchange constant, and α might be expected to be of the order 0.1 in silicon [170]. Using $U \sim 40$ meV for a single donor in silicon, and $t = U/6$ at the MIT [73], we obtain an estimation for the DM interaction $\alpha J \sim 1.2$ K, close to the observed activation energy. The mechanism responsible for the hysteresis could be the following: clusters with an odd number of sites have a ground state with a net spin, because of the DM interactions the cluster's spin has a preferential direction. Thus, to rotate the cluster's spin (after the magnetic field was changed) an energy barrier has to be overcome, which is the activation energy αJ. The mechanism requires a large number of clusters with an odd number of spins, and inversion symmetry to be broken. Both requirements are enhanced by larger inhomogeneity, and thus, are enhanced at low densities, in agreement with our observations, and with experiments on similar silicon and germanium δ-layers [36].

Low temperature inhomogeneous phase: Edge conduction

In the failed insulator picture, the transverse voltages are due to the samples' conductivity becoming anisotropic because of randomly emerging insulating regions. It stands to reason that the lower the dopant density, the more regions become insulating. This agrees with the planar-field transverse response and the hysteresis being stronger for lower density samples. When the density is sufficiently low, the anisotropy can be such that the conduction is different along different edges of a sample. To test this hypothesis, we made a special low density arsenic Hall bar ($n = (1 \pm 3) \times 10^{13}$ cm^{-2}) inspired by [171], as shown in Fig. 43a, in which the current can be passed through an edge and the voltage measured on the same edge (V_{Lat}) or on the opposite edge (V_{Hyb}). If the conduction is isotropic (and if source and drain contacts are sufficiently far from the contacts for the voltage measurements), then both voltages V_{Lat} and V_{Hyb} must be the same, however if the conduction is inhomogeneous, the voltage V_{Hyb} on the opposite edge becomes

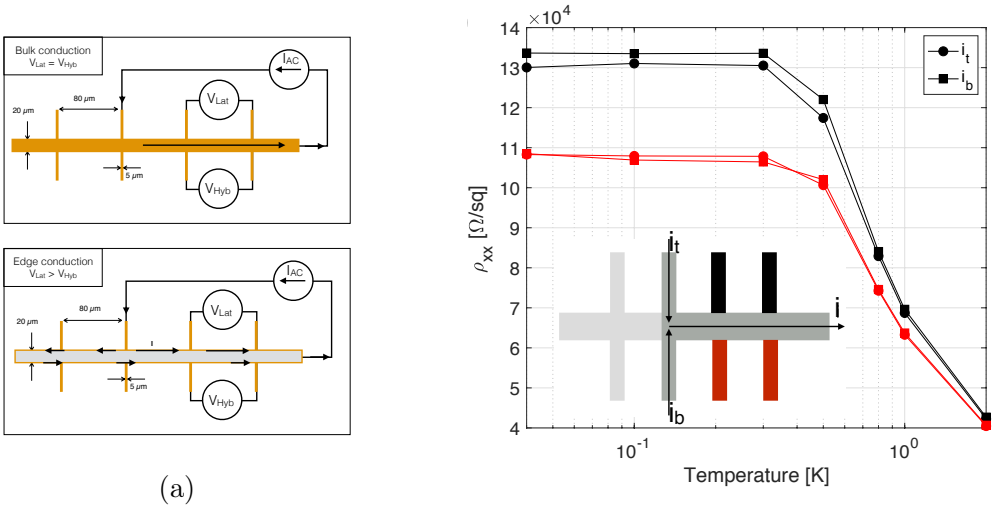

(a) (b)

Figure 43: **Evidence of inhomogeneous conduction.** (a) Setup for edge conduction measurements. Top: if the conduction is homogeneous in the sample both voltages V_{Lat} and V_{Hyb} are the same. Bottom: if the conduction is only on the edges of the sample the voltage V_{Lat} will be larger than V_{Hyb}. (b) Voltages V_{red} and V_{black} measured on the black and red leads (inset), respectively, as a function of temperature for a sample with density $n = (1 \pm 3) \times 10^{13}$ cm^{-2}. At $T < T_{crossover} \approx 500$ mK, V_{red} becomes different than V_{black}, indicating that the sample's conductivity is inhomogeneous. The inset shows the geometry used for the measurements, with I_t indicating the current being set from the top and I_b from the bottom. The resistance measured with I_t and I_b is indicated with circles and squares respectively. The colour of the contacts used to measure the resistance corresponds to the colour of the data.

different to V_{Lat}, and in the case of edge-only conduction V_{Hyb} is smaller than V_{Lat}. By looking at the temperature dependence of V_{Lat} and V_{Hyb} in Fig. 43b, it is clear that for temperatures above $T_{crossover}$ the voltages are the same, indicating homogeneous conduction, while for temperatures below $T_{crossover}$ they differ, proving that the conduction becomes highly inhomogeneous.

The inset in Fig. 43b shows the geometry used for the measurements shown in Fig. 43b, the red data are measured on the leads coloured in red and the black data on the leads coloured in black. Each voltage was measured twice, once for the current source connected to the top edge (black arrow I_t) and once to the bottom edge (black arrow I_b). The circles indicate the resistance measured with I_t and the squares the resistance measured with I_b. We find that the measured voltages are independent of the side on which the current was passed (I_t or I_b), meaning that the sample's conductivity is inhomogeneous but not limited to the edge, *i.e.*, it is not a topological insulator with edge-only conduction. In fact if the conduction was limited to the edges, the measurement would be symmetric

upon switching I_t to I_b and the black circle would be equal to the red squares (and inversely).

A further indication that the sample changes phase to an inhomogeneous phase is seen in Fig.44, in which the I-V characteristics are measured for V_{Lat}, along the edge of the $n = (1 \pm 3) \times 10^{13}$ cm^{-2} sample. For temperatures below $T_{crossover}$, the voltage V_{Lat} and V_{Hyb} show non-linear response to the applied current, indicating a transition to a non-Ohmic state. The non-Ohmic response could indicate an inhomogeneous glassy state, as also suggested by the hysteresis.

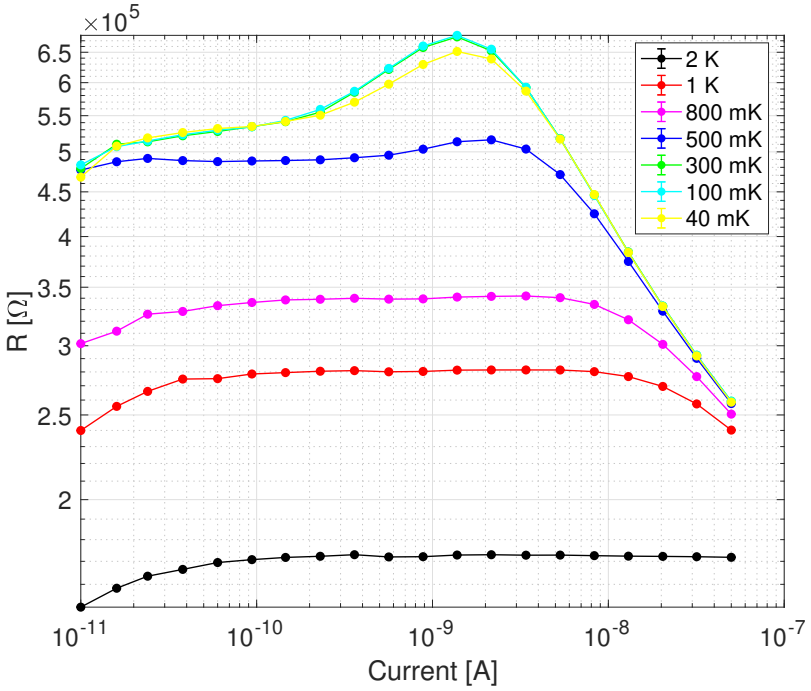

Figure 44: **Ohmic to non-Ohmic transition in the inhomogeneous phase.** Resistance on V_{Lat} as a function of current for multiple temperatures, in a sample with density $n = (1 \pm 3) \times 10^{13}$ cm^{-2}. As the temperature drops below $T_{crossover} \approx$ 500 mK the sample becomes non-Ohmic, as shown by the non-linear response to the current (non-constant resistance).

In conclusion we used magneto-transport measurements to show that for low dopant density δ-layers in silicon there are two regimes. The first is a conventional weakly localised disordered metal. While this regime has been extensively studied and described by localisation effects for silicon-based δ-layers, we find that when the conduction layers are sufficiently thin and dilute it becomes necessary to consider the Zeeman effect to describe the magneto-conductance. Moreover, we find that the Zeeman effect is isotropic and adds up in conductivity to the weak-localisation effect. The second regime is a failed insulator phase, for which the δ-layer becomes a mosaic of insulating and metallic regions. In this regime a

number of exotic effects appear, linked to strong inhomogeneity and time reversal symmetry breaking. In particular, at low electron densities we observe an anomalous even transverse voltage response, hysteresis in the magneto-conductance, and anisotropic conduction. It is interesting to note that in many cases planar-field transverse response, hysteretic magneto-conductance, and edge conduction are interpreted as proof of non-trivial topology [171,172], whereas our works suggests that non-trivial topology is not necessary to explain such effects. Instead, we can explain them by a regime of coexisting metallic and insulating regions, which is a plausible picture for materials close to the metal-to-insulator transition.

6 Conclusions

In this PhD work a number of observations are made about group-V doping layers in silicon. First of all, we can make the general statement that using arsenic instead of phosphorus for dopant-based quantum electronic devices is beneficial, because the adsorption of arsenic in silicon can be achieved with less donor diffusion and thus better precision. This claim is based on the fact that two-dimensional layers fabricated with arsenic are thinner than their phosphorus counterpart. The dopant layer thickness was measured by three methods: soft X-ray angle-resolved photon-emission spectroscopy (ARPES), X-ray reflectometry, and low temperature magneto-resistance. It is consistently found to be of the order of half a nanometre for arsenic δ-layers, and one nanometre for phosphorus δ-layers.

In addition to showing that X-rays can be used to measure two-dimensional dopant layer thickness, we showed that a combination of X-ray fluorescence and reflectometry can determine the three-dimensional distribution and atom-species of buried dopant structures in silicon, without affecting any of the electron's characteristics. This is an important development for device inspection and quality control, necessary for the fabrication of more complex structures, such as multi-qubit devices.

By means of low-temperature magneto-transport experiments, we also found that for low-dopant densities, electron-electron interactions effects become large, such that the magneto-conductance cannot be described by weak-localisation alone, but the Zeeman effect has to be taken into account. The Zeeman part of the magneto-conductance is isotropic in magnetic field direction and can be subtracted out by taking the difference between perpendicular and planar magnetic field sweeps. We found that for very thin layers, even at high dopant densities, omitting the Zeeman effect leads to a misestimation of the dopant layer thickness.

Finally, the reduced thickness and density of the conductive layers sets the conduction electrons in an unexplored regime; that of a highly disordered, half-filled, interacting electronic Hubbard model. The access to this new regime revealed new physical effects for doped silicon layers. Notably, we discovered that in low-density doping layers there is a low-temperature phase characterised by inhomogeneous conduction and slow spin relaxation dynamics. Because of the meandering of the current in the inhomogeneous conductor, we observe an anomalous transverse voltage that has an even response to magnetic fields. The inhomogeneous phase is marked by the apparent freezing of the conduction parameters, which can be due to the electron coherence length becoming limited by inelastic scattering on insulating regions. In future experiments it will be important to study the effect of cooling the conductive layers in the presence of magnetic fields, to determine

whether the formation of the inhomogeneous phase is history dependent, and whether the direction of the time reversal symmetry breaking can be controlled.

In conclusion, this work motivates the use of arsenic donors in silicon and germanium for quantum devices, and should foster interest in the physics of dilute, thin dopant layers in silicon. It is of particular interest to further explore the intriguing properties of two-dimensional doped silicon when doped close to the metal-insulator transition, in order to understand the exact nature of low temperature electron transport in the world's most common semiconductor.

A Appendix

A.1 Electrical measurement setup

In order to reach sufficiently low temperatures for the conductivity to be sensitive to quantum interference effects, we use a Triton 400 cryogen-free dilution refrigerator from Oxford instruments with a base temperature of ∼25 mK. The dilution system is equipped with a vector magnet operated at 4 K. The magnet is composed of three superconducting coils placed orthogonally with respect to each other, that can apply a magnetic field up to 2 T each. The sample holder is placed in the centre of the magnets. By controlling the current in each coil, the magnetic field can be rotated in any direction without moving the sample.

In the experiments the magnetic field is swept at 300 Gauss/min, slow enough to avoid excessive heating by induced currents, and before measuring the voltages we always wait for the temperature on the sample holder to have been stable for at least 60 seconds. The temperature is considered to be stable if it is within 3% of the set temperature, or within 60 mK when the temperature is set above 2 K. The temperature was measured with a RuO_2 thermometer attached on the puck at ∼1 cm distance from the sample.

The samples were attached with silver paint into standard lead-less chip-carriers and contacted with aluminium bonding wires. Most of the thermal contact was through the thermalised wires.

The longitudinal voltage V_{xx} and the transverse voltage V_{xy} were measured with a four-point scheme such as to be insensitive to the contact resistances, as shown on figure 45. A small AC current was passed across the Hall bars, and the voltage was measured with a lock-in amplifier on a pair of contact leads on one side of the Hall bar for V_{xx}, and on opposing sides for V_{xy}. The samples have eight contacts, of which two are used for passing the current, meaning that there are six ways of measuring V_{xx} and three ways of measuring V_{xy}. For extremely low temperature measurements, it is important to use low currents, in our case less than 1 nA, to avoid heating the samples by Joule heating. The use of low currents comes with the difficulty of extracting low voltages from the environment noise. Firstly, all the measurement circuits have to be shielded from electromagnetic radio-frequency interference from lab equipment, etc., and care is taken to not create ground loops. The remaining noise mostly comes from the thermal electric noise in the room-temperature part of the setup. Noise is reduced by limiting the distance that the voltage signal and current have to travel at room-temperature outside of the dilution refrigerator before being amplified. However, the voltage signal often remains smaller than the background noise, making it necessary to use a low frequency AC (13.7 Hz) current and lock-in amplifiers to amplify the

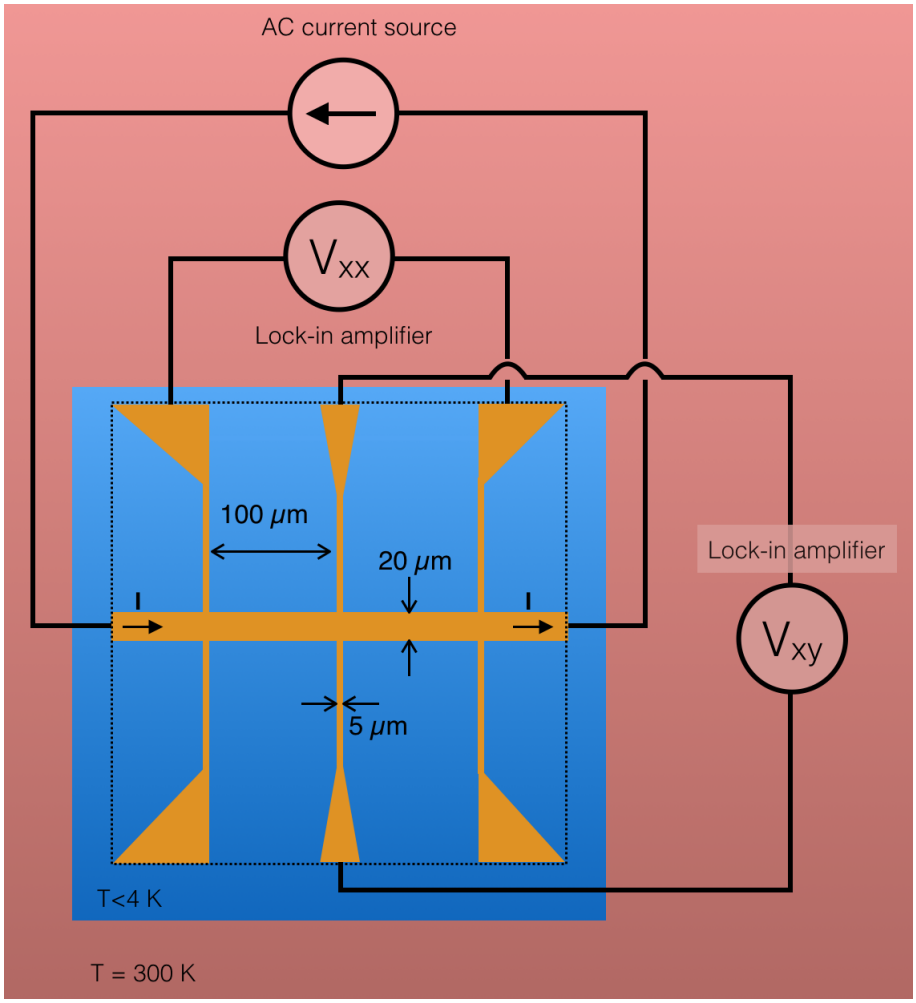

Figure 45: Four-point setup for electrical measurements of a Hall bar. The red region represents the electronics at ∼300 K, and the blue region represents the part of the circuit in the dilution refrigerator.

voltage at the excitation frequency.

For our measurements we first used a Lakeshore 370, which contains the AC current source and the lock-in amplifier. Later we changed to using a CS580 current source and a SR830 lock in from Stanford research instruments, and the current source was controlled by the SX199 optical switch. While the latter setup offered more experimental flexibility, the results were not influenced by the instrumentation.

A.2 Sample alignment and Ohmic measurements

The vector magnet in the dilution system gives the possibility to align the field very precisely to the device's axis. In many measurement systems, the magnetic

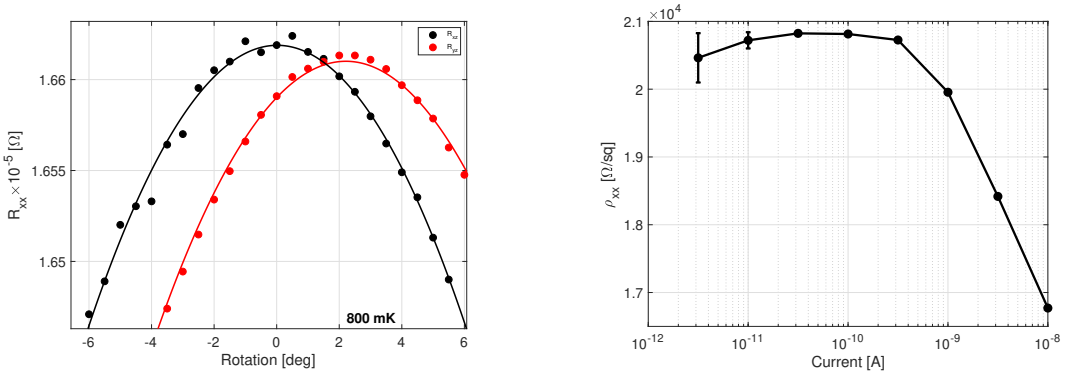

(a) (b)

Figure 46: (a) Magnetic field alignments at 2 T and 800 mK. The maximum of resistance is for the magnetic field in the Hall bar's plane. (b) Resistivity as a function of the current at 40 mK and 0 T.

field is fixed and the sample rotated around one axis, such that it is impossible to correct field misalignment in all direction. Here, after having cooled down a sample, we start by rotating the magnetic field around the Hall bar's X and Y axis. Because of the weak-localisation effect (equation (13)), the resistance is maximum when the field is in the δ-layer's plane. An example of alignment measurements for a sample with electron density $1.2{\times}10^{13}$ cm^{-2} is shown in figure 46a, by finding the angles at the maximum of resistance in the field rotations around the X and Y axis we can define the orthonormal sample axis. The alignment is very precise, for example the uncertainty of the correction angles from the measurements shown in figure 46a is ≈ 0.03 degrees.

A prerequisite to making magneto-transport measurements is to ensure that the measurements are taken in the linear I-V regime, *i.e.*, in the Ohmic regime. Figure 46b shows a measurement of the resistivity as function of the current at 40 mK and in the absence of magnetic field, for the same sample. In practice, the resistance is obtained from the measured voltage using Ohm's law ($R = V/I$), which implies a linear I-V relation for the resistance to be independent of the current. In the case of our δ-layers, as is visible figure 46b, the resistivity is independent of the current up to hundreds of pA. At higher currents, the sample is heating, such that the resistance decreases as expected for weakly localised conduction (see equation (6)). The maximum current of the Ohmic regime depends on the sample's resistance, because the power from the Joules heating $P = I^2R$ causes samples with higher resistance to experience significant heating at lower currents. In our experiments we always make sure to be in the Ohmic regime.

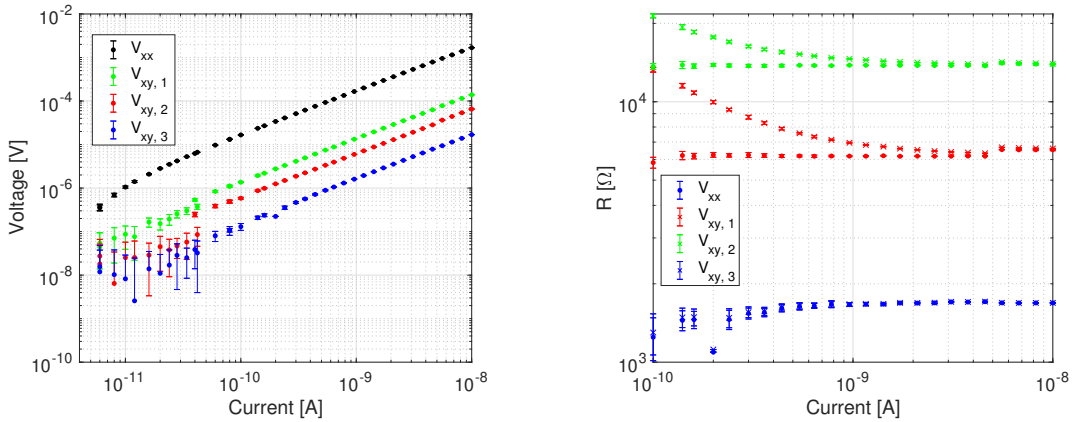

(a) (b)

Figure 47: (a) I-V characteristics of the longitudinal voltage V_{xx} and transverse voltage V_{xy} measured on three pairs of contacts, with no magnetic field, at 100 mK. (b) The resistance extracted from (a) with (crosses) and without (dots) taking into account the I=0 voltage offset.

A.3 Anomalous V_{xy} effect and feedthrough

The anomalous transverse voltage V_{xy} shown in section 5.2.2, observed in low-density δ-layers, is discussed here in more details. The I-V characteristics in the absence of a magnetic field at 100 mK of our lowest density sample (which has the strongest anomalous behaviour) are shown in figure 47a. The curves are linear with a constant offset of the order of 10^{-7} V at zero current. The transverse voltage V_{xy} measured on three separate pairs of contacts (see figure 11 for a sketch of the sample) shows that V_{xy} is location dependent, as would be expected in an inhomogeneous conductor. In section 5.2.2, the transverse resistances shown in figure 36 are taken from the same contacts as $V_{xy,3}$ in figure 47a. The same I-V data is converted to resistance using Ohm's law in figure 47b, both by subtracting the zero current offset (crosses) and not (dots). We see that not taking into account the offset results on a non-constant resistance R_{xy} up to $\sim$1 nA for $V_{xy,1}$ and $V_{xy,2}$, and makes no visible difference for $V_{xy,3}$. The lead misalignment necessary to cause such spontaneous voltages at 100 mK would be of 16.6 μm, 7.8 μm, and 2.0 μm for $V_{xy,1}$, $V_{xy,2}$, and $V_{xy,3}$, respectively, much more than what can be expected for lithographically etched devices.

A good way to look for the effect of lead misalignment to the transverse resistance R_{xy} is to look at R_{xy} as a function of R_{xx}, because one expects

$$R_{xy} = R_{offset} + \delta R_{xx} + R_{Hall}, \tag{18}$$

where δ is the lead misalignment. Thus, in the absence of planar V_{xy} effects, the data plotted as R_{xy}/R_{xx}, as in figure 48a for in-plane magnetic fields should, be

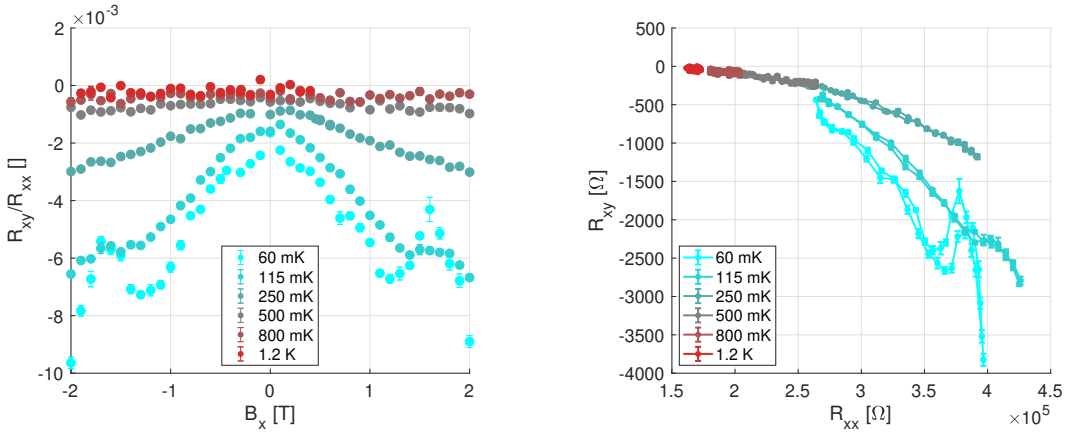

(a) (b)

Figure 48: (a) R_{xy}/R_{xx} as function of B_x for multiple temperatures, measured in the the low density sample, n=1.2×10^{13} cm^{-2}. (b) The same data as in (a), shown in the from of R_{xy} as a function of R_{xx}, for multiple temperatures.

a constant, δ. Similarly, plotting the same data from figure 48a in the form R_{xy} as a function of R_{xx} should give a linear function with slope δ. In figure 48b the dependence is linear for temperatures down to 500 mK, with a realistic slope δ=0.46μm. For lower temperatures, for which a non constant R_{xy}/R_{xx} effect is seen in figure 48a, the relation becomes non linear, indicating that feedthrough cannot explain the measured R_{xy}.

Finally, the anomalous transverse voltage was shown to be stronger for planar fields in figure 36. Here, in figure 49a and 49b we show that in a dilute sample, the effect at 250 mK of a planar field parallel to the current B_x and transverse to the current B_y, is the same within error margins. In figure 49b we see that the angle of the planar field with respect to the current in the sample has a small influence, with the largest R_{xy} response when the field is parallel to the current.

A.4 Hall factor temperature dependence

The Hall factor R_H is the slope of the antisymmetric piece of R_{xy} as a function of magnetic field $B_\perp$. R_H is related to the electron density n as $R_H = 1/(ne)$, such that the Hall slope is lower for higher density samples. The effect of electron-electron interactions is to increase R_H by an amount δR_H at low temperatures, proportionally to the increase of the longitudinal resistance δR. The expected relation is $\delta R_H/R_H = 2\delta R/R$, however it is necessary to extract the part of δR that stems from electron-electron interactions to verify the relation [87]. In our case, the Hall effect in low density samples becomes indiscernible because of the dominating anomalous effect, and taking the odd part of the effect does not

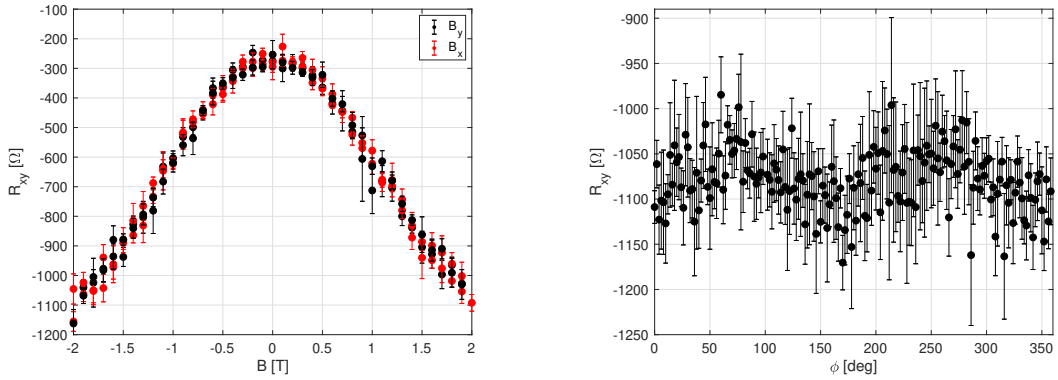

(a) (b)

Figure 49: (a) Measured R_{xy} in the sample with density $n = 1.2 \times 10^{13}$ cm^{-2}, at 250 mK as a function of a planar magnetic field parallel B_x to the current and perpendicular B_y to the current. (b) R_{xy} in the same sample as a function of the in-plane angle of a 2 T field. At 0 degrees the field is parallel to the current.

give a clear linear function. Thus, we can only look at the change of R_H at low temperatures in denser samples, as shown in figure 50. The sample with density $n = 8.5 \times 10^{13}$ cm^{-2} has a Hall factor R_H that increases at low temperatures and saturates at the critical temperature for which the conductivity saturates. This effect, along with the Zeeman effect, and the conductivity's temperature dependence, confirms that in the dilute δ-layers electron-electron interactions are non negligible.

A.5 Dopant depth profile and transverse voltage

From SIMS measurements, shown in figure 51, we know that the dopant distribution as a function of depth is not a symmetric gaussian function, but has a stretched tail away from the surface. The asymmetric distribution is a result of diffusion during sample growth. The gradient of donor electrons across the layer causes an electric field $E_\perp$ perpendicular to the dopant layer. When the electron density is high, screening prevents the electrons from feeling $E_\perp$. In the frame of the moving electrons, the electric field is seen as an in-plane magnetic field $B_{||}$, this is the Rashba effect [19]. However, the Rashba magnetic field cannot be responsible for the transverse voltage, as it is in-plane. For a transverse voltage V_{xy} to be generated, there should be an effect that would couple the electric field $E_\perp$ and the electron current I with a cross product such that a transverse voltage V_{xy} is generated, however such an effect would contradict the Onsager relation $\rho_{xy}(H) = \rho_{yx}(-H)$, without breaking time reversal symmetry, and is thus not possible.

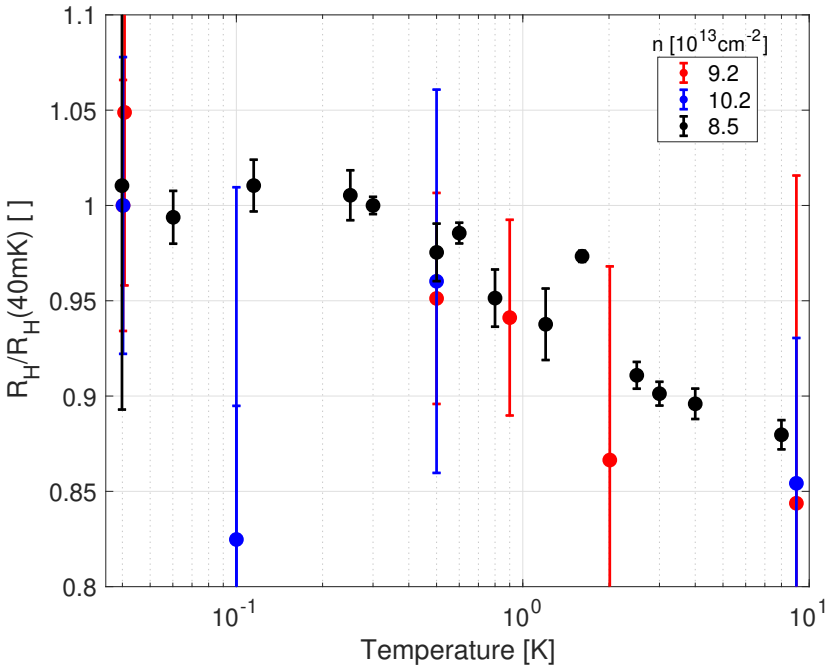

Figure 50: Hall slope as a function of temperature for three samples. The samples' electron density is given in the legend.

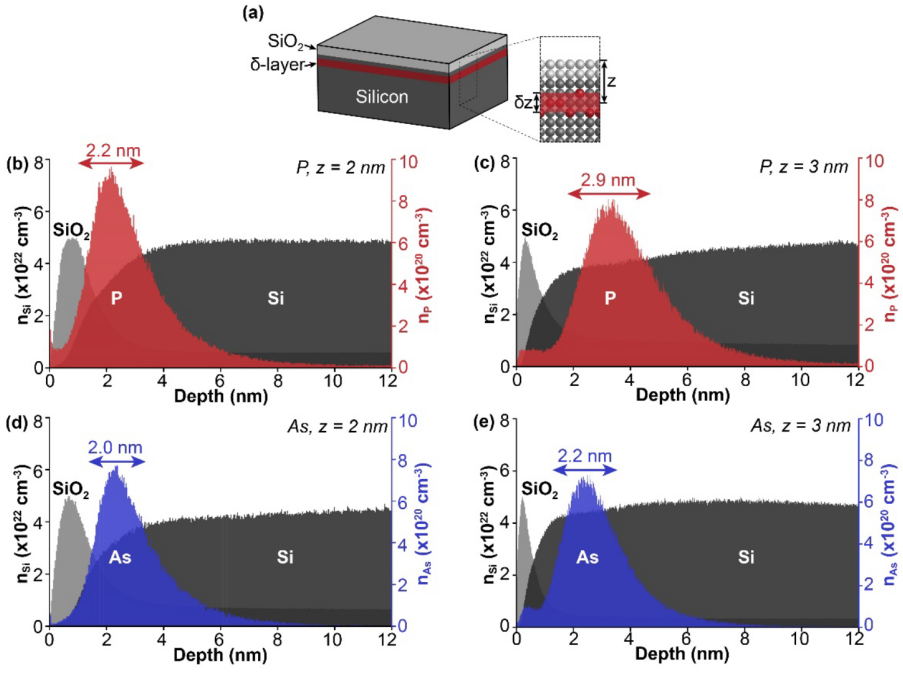

Figure 51: **Dopant distribution depth profile.** Secondary-ion mass spectroscopy depth profile of four δ-layers, from Procopios Constantinou. (a) Is a sketch of the sample. (b,c) As layers depth profiles. (d,e) P layers depth profiles.

A.6 X-ray fluorescence methods

Sample preparation. Si(001) samples were diced to 2×9 mm from a 0.5 mm thick, Czochralski grown wafer, with bulk arsenic doping of density $3{\times}10^{14}$ cm^{-3}, and resistivity >15 Ω cm. These samples were cleaned ultrasonically in acetone followed by isopropyl alcohol. Each sample was thermally outgassed in vacuum (base pressure $<5{\times}10^{-10}$ mBar) for >8 h at 600 °C, and flash annealed multiple times at 1200 °C, using direct current resistive sample heating. Sample temperature was monitored using an infrared pyrometer (IMPAC IGA50-LO plus), with a total estimated measurement uncertainty of ±30 °C.

The samples were dosed with AsH_3 with varying total exposures to control the dopant density. They were then heated at 350 °C for 2 minutes to incorporate the dopants into the Si lattice [173]. Subsequently, samples were imaged with STM, as shown in Fig. 21, and the density of ejected Si atoms was used to estimate the density of incorporated As atoms n_{STM}. All STM measurements were performed in an Omicron variable temperature series STM at room temperature with a base pressure of $<5{\times}10^{-11}$ mBar. After incorporation, 2 nm of Si were deposited on the samples with no resistive sample heating. The samples were then resistively heated to 500 °C for 15 seconds. This procedure gives a well-confined, electrically active dopant layer [82, 83]. A further 28 nm of Si was deposited on the samples held at 250 °C. Si deposition was performed at a base pressure of $2{\times}10^{-10}$ mBar, using an all silicon, solid sublimation source (SUSI-40, MBE Komponenten GmbH) operated at a deposition rate of 0.003 nm/s. During Si deposition, the sample temperature was indirectly monitored by measuring the sample resistance, while heating using a direct current resistive sample heater.

To measure the electrical properties of the dopant layers, the samples were etched into Hall bars. This was done using optical lithography and reactive ion etching. Ohmic contacts were established by deposition of aluminium into arrays of etched holes extending through the δ layer [84]. On each sample, two Hall-bars were produced, as well as an unetched region to be used for SIMS. The samples were cleaved between the two Hall-bars. Each Hall-bar was mounted on a chip carrier, and electrically connected to the carrier by aluminium wire bonds.

X-ray fluorescence spectrum. The fluorescence spectra obtained at each pixel of the XRF images (see Fig. 22a-c) are decomposed into a sum of elemental spectra with the help of the PyMca software [144]. An example of a decomposition is presented in Fig. 52, where the fluorescence spectrum of each separate atomic-species is shown. Scattering peaks are also shown as dotted lines; they are the two peaks at highest energy, with the elastic scattering at the incident energy 11.88 keV and the inelastic Compton peak at slightly lower energy. Clearly visible in the spectrum is that each elemental spectrum contains at least one peak

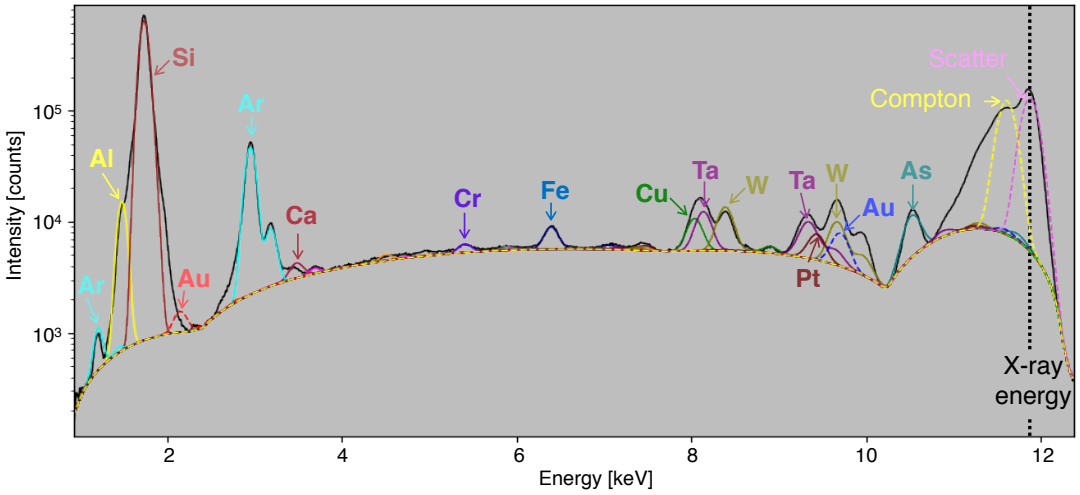

Figure 52: X-ray fluorescence spectrum taken over the highlighted area in Fig 22. The black line is the data and coloured lines are fits to one element's resonant edge. Full lines indicate a K-edge, while dotted lines indicate L and M-edges as well as the scattering peaks.

at a unique frequency, such that it is straightforward to identify the elements contributing to the spectrum. Only elements that cannot be excited by the incident X-ray energy cannot be detected by fluorescence. For the energy used here, 11.88 keV, the heaviest detectable element is U. To obtain a single element image, as shown in Fig. 22a-c, it suffices to isolate in each pixel the intensity of one elemental fluorescence peak at its known energy.

X-ray fluorescence signal/noise ratio. To calculate the signal/noise ratio (SNR) given in Fig. 23, we took two 30 μm traces, one on the doped region (T_{on}) and one off the doped region (T_{off}). The SNR was then simply defined as $SNR = (\text{mean}(T_{On}) - \text{mean}(T_{off}))/\text{std}(T_{On}))$.

Magneto-transport setup. For the electrical measurements we used a standard Physical Property Measurement System (PPMS) from Quantum Design. It contains a cryostat with a superconducting magnet coil, and can control the temperature down to $T = 1.8$ K and the magnetic field up to $B = 9$ T. The samples were bonded on a standard lead-less chip carrier and inserted in a socket attached to a horizontal rotator. The rotator is motor-controlled and the rotation axis is such that the magnetic field can be set from parallel to perpendicular to the current in the Hall-bar. The resistance is measured in a four-point geometry using a resistance bridge and with a 5 Hz square wave 100 nA current. The current is chosen to be in the linear $I - V$ response regime, and such that the Joule heating is negligible.

Secondary-ion mass spectrometry. Time-of-flight SIMS measurements were

conducted using an IONTOF ToF-SIMS(5) system with a 25 keV Bi^+ primary ion beam in high current bunch mode, and a 500 eV, 35 nA Cs^+ sputter beam. Depth profiles were made with a 300 $\times$ 300 μm sputter crater, and the analytical region was the central 50 $\times$ 50 μm of the sputter region. The measured As-ion count rate was converted to a dopant density by measuring a sample of known density with the same setup.

Author's contribution

As the author of this thesis, Nicolò D'Anna, I made the following contribution to each section:

Section 2, *Physics of two-dimensional disordered conductors*: I wrote the introduction to the two-dimensional metal-to-insulator transition.

Section 3, *Silicon δ-doped samples*: I wrote the introduction to the samples fabricated at UCL.

Section 4, *Imaging of buried dopants*: I lead the research projects, wrote a proposal and obtained an X-ray reflectometry beamtime, analysed the data and wrote the papers. I did not take the X-ray fluorescence measurements myself.

Section 5, *Electrons in buried dopant layers*: I did all the magneto-transports measurements and analysis, and wrote the magneto-transport paper (draft). In the ARPES project I contributed by doing the magneto-transport measurements of the samples to benchmark the technique, and I will be a co-author on the ensuing paper.

All the content of the thesis was written by me.

Acknowledgments

This work would not have been possible without the help and contribution of many skilled scientists and technicians, and the supervision of Prof. Gabriel Aeppli.
At PSI, I was always given a hand when in need by my group members, Simon Gerber, Guy Matmon, Jakub Vonka, Maël Clémence, Aidan McConnell and Stefan Stutz.
I am thankful that I was welcomed by Marek Bartkowiak and Yeong-Ah Soh to use their low temperature transport setups. I am grateful to Dario Ferreira Sanchez and Daniel Grolimund for the X-ray fluorescence measurements, and to Urs Staub and Elizabeth Marie Skoropata for helping with the X-ray reflectometry.
I am indebted to Procopios Constantinou, Jamie Bragg, Taylor Stock, juerong li, Steven Schofield and Neil Curson for the δ-layer sample fabrication.
I would also like to thank Markus Müller for helping to elucidate the physics governing our samples and experiments.

This project received funding from the European Research Council under the European Union's Horizon 2020 research and innovation program, within the Hidden, Entangled and Resonating Order (HERO) project with Grant Agreement 810451. Nicolò D'Anna was partially supported by Swiss National Science Foundation Contract 175867.

References

[1] N. D'Anna, D.F. Sanchez, G. Matmon, J. Bragg, P.C. Constantinou, T.J.Z. Stock et al., *Non-destructive x-ray imaging of patterned delta-layer devices in silicon* 2022.

[2] Y. Kawaguchi, H. Kitahara and S. Kawaji, *Angular dependent negative magnetoresistance in si-mos (111) inversion layers*, *Solid State Communications* **26** (1978) 701.

[3] I. Eisele and G. Dorda, *Negative magnetoresistance in n-channel (100) silicon inversion layers*, *Phys. Rev. Lett.* **32** (1974) 1360.

[4] P.W. Anderson, *Absence of diffusion in certain random lattices*, *Phys. Rev.* **109** (1958) 1492.

[5] N. Mott, *Charge transport in non-crystalline semiconductors* in *Festkörper Probleme IX*, pp. 22–45 (1969).

[6] S. Hikami, A.I. Larkin and Y. Nagaoka, *Spin-Orbit Interaction and Magnetoresistance in the Two Dimensional Random System*, *Progress of Theoretical Physics* **63** (1980) 707.

[7] K.E.J. Goh, M.Y. Simmons and A.R. Hamilton, *Electron-electron interactions in highly disordered two-dimensional systems*, *Phys. Rev. B* **77** (2008) 235410.

[8] B. Altshuler and A. Aronov, *Chapter 1 - electron-electron interaction in disordered conductors* in *Electron–Electron Interactions in Disordered Systems*, pp. 1–153 (1985).

[9] L. Oberbeck, N.J. Curson, M.Y. Simmons, R. Brenner, A.R. Hamilton, S.R. Schofield et al., *Encapsulation of phosphorus dopants in silicon for the fabrication of a quantum computer*, *Applied Physics Letters* **81** (2002) 3197.

[10] G. Scappucci, G. Capellini, W.C.T. Lee and M.Y. Simmons, *Ultradense phosphorus in germanium delta-doped layers*, *Applied Physics Letters* **94** (2009) 162106.

[11] R.G. Wheeler, *Magnetoconductance and weak localization in silicon inversion layers*, *Phys. Rev. B* **24** (1981) 4645.

[12] R. Cheung, L. Geerligs, J. Caro, A. Verbruggen, K. Werner and S. Radelaar, *Weak localisation and correlation effects in a two dimensional hole gas in si/si$_{1-x}$ge$_x$ heterostructures*, *Physica B: Condensed Matter* **194-196** (1994) 1225.

[13] G.M. Minkov, A.V. Germanenko and I.V. Gornyi, *Magnetoresistance and dephasing in a two-dimensional electron gas at intermediate conductances*, *Phys. Rev. B* **70** (2004) 245423.

[14] G.M. Minkov, A.V. Germanenko, O.E. Rut, A.A. Sherstobitov, L.E. Golub, B.N. Zvonkov et al., *Weak antilocalization in quantum wells in tilted magnetic fields*, *Phys. Rev. B* **70** (2004) 155323.

[15] G.L. Chen, J. Han, T.T. Huang, S. Datta and D.B. Janes, *Observation of the interfacial-field-induced weak antilocalization in inas quantum structures*, *Phys. Rev. B* **47** (1993) 4084.

[16] P.D. Dresselhaus, C.M.A. Papavassiliou, R.G. Wheeler and R.N. Sacks, *Observation of spin precession in gaas inversion layers using antilocalization*, *Phys. Rev. Lett.* **68** (1992) 106.

[17] M. Lang, L. He, X. Kou, P. Upadhyaya, Y. Fan, H. Chu et al., *Competing weak localization and weak antilocalization in ultrathin topological insulators*, *Nano Letters* **13** (2013) 48.

[18] X. Wu, X. Li, Z. Song, C. Berger and W.A. de Heer, *Weak antilocalization in epitaxial graphene: Evidence for chiral electrons*, *Phys. Rev. Lett.* **98** (2007) 136801.

[19] E. RASHBA, *Properties of semiconductors with an extremum loop. i. cyclotron and combinational resonance in a magnetic field perpendicular to the plane of the loop*, *Sov. Phys.-Solid State* **2** (1960) 1109.

[20] G. Dresselhaus, *Spin-orbit coupling effects in zinc blende structures*, *Phys. Rev.* **100** (1955) 580.

[21] S.V. Iordanskii, Y.B. Lyanda-Geller and G.E. Pikus, *Weak localization in quantum wells with spin-orbit interaction*, *ZhETF Pisma Redaktsiiu* **60** (1994) 199.

[22] J.T. Mlack, K.S. Wickramasinghe, T.D. Mishima, M.B. Santos and C.M. Marcus, *In-plane magnetoconductance mapping of insb quantum wells* 2019.

[23] A.D. Caviglia, M. Gabay, S. Gariglio, N. Reyren, C. Cancellieri and J.-M. Triscone, *Tunable rashba spin-orbit interaction at oxide interfaces*, *Phys. Rev. Lett.* **104** (2010) 126803.

[24] I.B. Berkutov, V.V. Andrievskii, Y.F. Komnik, Y.A. Kolesnichenko, A.I. Berkutova, D.R. Leadley et al., *Interference effects in silicon-germanium heterostructures with quantum wells of different widths*, *Low Temperature Physics* **42** (2016) 111.

[25] J. Hubbard and B.H. Flowers, *Electron correlations in narrow energy bands*, *Proceedings of the Royal Society of London. Series A. Mathematical and Physical Sciences* **276** (1963) 238.

[26] O. Dutta, M. Gajda, P. Hauke, M. Lewenstein, D.-S. Lühmann, B.A. Malomed et al., *Non-standard hubbard models in optical lattices: a review*, *Reports on Progress in Physics* **78** (2015) 066001.

[27] M. Greiner, O. Mandel, T. Esslinger, T.W. Hänsch and I. Bloch, *Quantum phase transition from a superfluid to a mott insulator in a gas of ultracold atoms*, *Nature* **415** (2002) 39.

[28] X.Y. Zhang, M.J. Rozenberg and G. Kotliar, *Mott transition in the d=∞ hubbard model at zero temperature*, *Phys. Rev. Lett.* **70** (1993) 1666.

[29] M. Gall, N. Wurz, J. Samland, C.F. Chan and M. Köhl, *Competing magnetic orders in a bilayer hubbard model with ultracold atoms*, *Nature* **589** (2021) 40.

[30] M. Kiczynski, S.K. Gorman, H. Geng, M.B. Donnelly, Y. Chung, Y. He et al., *Engineering topological states in atom-based semiconductor quantum dots*, *Nature* **606** (2022) 694.

[31] P.A. Lee and T.V. Ramakrishnan, *Magnetoresistance of weakly disordered electrons*, *Phys. Rev. B* **26** (1982) 4009.

[32] B. Shinozaki, K. Hidaka, S. Ezaki, K. Makise, T. Asano, S. Tomai et al., *Electron weak localization and electron-electron interaction effects on magneto-conductivity in in–ga–zn oxide films*, *Thin Solid Films* **551** (2014) 195.

[33] Y. Takahide, Y. Sasama, M. Tanaka, H. Takeya, Y. Takano, T. Kageura et al., *Spin-induced anomalous magnetoresistance at the (100) surface of hydrogen-terminated diamond*, *Physical Review B* **94** (2016) 161301.

[34] D. Simonian, S.V. Kravchenko, M.P. Sarachik and V.M. Pudalov, *h/t scaling of the magnetoconductance near the conductor-insulator transition in two dimensions*, *Phys. Rev. B* **57** (1998) R9420.

[35] B.L. Altshuler, D. Khmel'nitzkii, A.I. Larkin and P.A. Lee, *Magnetoresistance and hall effect in a disordered two-dimensional electron gas*, *Phys. Rev. B* **22** (1980) 5142.

[36] S. Shamim, S. Mahapatra, G. Scappucci, W.M. Klesse, M.Y. Simmons and A. Ghosh, *Spontaneous breaking of time-reversal symmetry in strongly interacting two-dimensional electron layers in silicon and germanium*, *Phys. Rev. Lett.* **112** (2014) 236602.

[37] B.L. Altshuler, A.G. Aronov and P.A. Lee, *Interaction effects in disordered fermi systems in two dimensions*, *Phys. Rev. Lett.* **44** (1980) 1288.

[38] M.J. Uren, R.A. Davies and M. Pepper, *The observation of interaction and localisation effects in a two-dimensional electron gas at low temperatures*, *Journal of Physics C: Solid State Physics* **13** (1980) L985.

[39] E. Abrahams, P.W. Anderson, D.C. Licciardello and T.V. Ramakrishnan, *Scaling theory of localization: Absence of quantum diffusion in two dimensions*, *Phys. Rev. Lett.* **42** (1979) 673.

[40] S.V. Kravchenko, G.V. Kravchenko, J.E. Furneaux, V.M. Pudalov and M. D'Iorio, *Possible metal-insulator transition at b=0 in two dimensions*, *Phys. Rev. B* **50** (1994) 8039.

[41] M.Y. Azbel', *Quantum particle in a random potential: Exact solution and its implications*, *Phys. Rev. B* **45** (1992) 4208.

[42] L.A. Ponomarenko, A.K. Geim, A.A. Zhukov, R. Jalil, S.V. Morozov, K.S. Novoselov et al., *Tunable metal-insulator transition in double-layer graphene heterostructures*, *Nature Physics* **7** (2011) 958.

[43] Y. Zhang, Y. Cao, H. Hu, X. Wang, P. Li, Y. Yang et al., *Flexible metal-insulator transitions based on van der Waals oxide heterostructures*, *ACS Applied Materials & Interfaces* **11** (2019) 8284.

[44] A.A. Shashkin, M.Y. Melnikov, V.T. Dolgopolov, M.M. Radonjić, V. Dobrosavljević, S.-H. Huang et al., *Manifestation of strong correlations in transport in ultraclean SiGe/Si/SiGe quantum wells*, *Phys. Rev. B* **102** (2020) 081119.

[45] E. Ribeiro, R.D. Jäggi, T. Heinzel, K. Ensslin, G. Medeiros-Ribeiro and P.M. Petroff, *Metal-insulator transition in a disordered two-dimensional electron gas in GaAs-AlGaAs at zero magnetic field*, *Phys. Rev. Lett.* **82** (1999) 996.

[46] A. Narjis, A.E. kaaouachi, S. Dlimi, M. Errai, L. Limouny, A. Sybous et al., *The observation of a percolation-induced 2D metal-insulator transition in AlAs*, *Chinese Journal of Physics* **51** (2013) 1305.

[47] Q. Xu, L. Hartmann, H. Schmidt, H. Hochmuth, M. Lorenz, R. Schmidt-Grund et al., *Metal-insulator transition in co-doped* ZnO*: Magnetotransport properties*, *Phys. Rev. B* **73** (2006) 205342.

[48] C. Zhang, S. KC, Y. Nie, C. Liang, W.G. Vandenberghe, R.C. Longo et al., *Charge mediated reversible metal-insulator transition in monolayer* $MoTe_2$ *and* $W_xMo_{1-x}Te_2$ *alloy*, *ACS Nano* **10** (2016) 7370.

[49] A. Shashkin and S. Kravchenko, *Metal-insulator transition and low-density phases in a strongly-interacting two-dimensional electron system*, *Annals of Physics* **435** (2021) 168542.

[50] A. Punnoose and A.M. Finkel'stein, *Dilute electron gas near the metal-insulator transition: Role of valleys in silicon inversion layers*, *Phys. Rev. Lett.* **88** (2001) 016802.

[51] A. Punnoose and A.M. Finkel'stein, *Metal-insulator transition in disordered two-dimensional electron systems*, *Science* **310** (2005) 289.

[52] A.A. Shashkin, S.V. Kravchenko and T.M. Klapwijk, *Metal-insulator transition in a 2d electron gas: Equivalence of two approaches for determining the critical point*, *Phys. Rev. Lett.* **87** (2001) 266402.

[53] M.Y. Melnikov, A.A. Shashkin, V.T. Dolgopolov, A.Y.X. Zhu, S.V. Kravchenko, S.-H. Huang et al., *Quantum phase transition in ultrahigh mobility sige/si/sige two-dimensional electron system*, *Phys. Rev. B* **99** (2019) 081106.

[54] G. Zala, B.N. Narozhny and I.L. Aleiner, *Interaction corrections at intermediate temperatures: Longitudinal conductivity and kinetic equation*, *Phys. Rev. B* **64** (2001) 214204.

[55] S.V. Kravchenko and M.P. Sarachik, *Metal–insulator transition in two-dimensional electron systems*, *Reports on Progress in Physics* **67** (2003) 1.

[56] A. Yildiz, N. Serin, T. Serin and M. Kasap, *Crossover from nearest-neighbor hopping conduction to Efros–Shklovskii variable-range hopping conduction in hydrogenated amorphous silicon films*, *Japanese Journal of Applied Physics* **48** (2009) 111203.

[57] S. Das Sarma and E.H. Hwang, *Two-dimensional metal-insulator transition as a strong localization induced crossover phenomenon*, *Phys. Rev. B* **89** (2014) 235423.

[58] S. Das Sarma, E.H. Hwang and Q. Li, *Two-dimensional metal-insulator transition as a potential fluctuation driven semiclassical transport phenomenon*, *Phys. Rev. B* **88** (2013) 155310.

[59] G. Matmon, E. Ginossar, B.J. Villis, A. Kölker, T. Lim, H. Solanki et al., *Two- to three-dimensional crossover in a dense electron liquid in silicon*, *Phys. Rev. B* **97** (2018) 155306.

[60] C.M. Polley, W.R. Clarke and M.Y. Simmons, *Comparison of nickel silicide and aluminium ohmic contact metallizations for low-temperature quantum transport measurements*, *Nanoscale Research Letters* **6** (2011) 538.

[61] P. Fournier, C. Lobb and R. Greene, *Saturation of the phase coherence length at low temperatures in pr1.95ce0.05cuo4*, *Physica C: Superconductivity* **341-348** (2000) 1941.

[62] T. Ihn, D. Graf, F. Molitor, C. Stampfer and K. Ensslin, *Phase-coherent transport in a mesoscopic few-layer graphite wire*, *Physica E: Low-dimensional Systems and Nanostructures* **40** (2008) 1851.

[63] D.-K. Ki, D. Jeong, J.-H. Choi, H.-J. Lee and K.-S. Park, *Inelastic scattering in a monolayer graphene sheet: A weak-localization study*, *Phys. Rev. B* **78** (2008) 125409.

[64] A. Kapitulnik, S.A. Kivelson and B. Spivak, *Colloquium: Anomalous metals: Failed superconductors*, *Rev. Mod. Phys.* **91** (2019) 011002.

[65] A.A. Shashkin, *Metal–insulator transitions and the effects of electron–electron interactions in two-dimensional electron systems*, *Physics-Uspekhi* **48** (2005) 129.

[66] B. Tanatar and D.M. Ceperley, *Ground state of the two-dimensional electron gas*, *Phys. Rev. B* **39** (1989) 5005.

[67] C. Attaccalite, S. Moroni, P. Gori-Giorgi and G.B. Bachelet, *Correlation energy and spin polarization in the 2d electron gas*, *Phys. Rev. Lett.* **88** (2002) 256601.

[68] V.T. Dolgopolov, *Two-dimensional system of strongly interacting electrons in silicon (100) structures*, *Physics-Uspekhi* **62** (2019) 633.

[69] J. Jaroszyński, D. Popović and T.M. Klapwijk, *Magnetic-field dependence of the anomalous noise behavior in a two-dimensional electron system in silicon*, *Phys. Rev. Lett.* **92** (2004) 226403.

[70] S.c.v. Bogdanovich and D. Popović, *Onset of glassy dynamics in a two-dimensional electron system in silicon*, *Phys. Rev. Lett.* **88** (2002) 236401.

[71] J. Jaroszyński, D. Popović and T.M. Klapwijk, *Universal behavior of the resistance noise across the metal-insulator transition in silicon inversion layers*, *Phys. Rev. Lett.* **89** (2002) 276401.

[72] K. Byczuk, W. Hofstetter and D. Vollhardt, *Mott-hubbard transition versus anderson localization in correlated electron systems with disorder*, *Phys. Rev. Lett.* **94** (2005) 056404.

[73] C. Walsh, P. Sémon, D. Poulin, G. Sordi and A.-M.S. Tremblay, *Thermodynamic and information-theoretic description of the mott transition in the two-dimensional hubbard model*, *Phys. Rev. B* **99** (2019) 075122.

[74] M.E. Barber, E.Y. Ma and Z.-X. Shen, *Microwave impedance microscopy and its application to quantum materials*, *Nature Reviews Physics* **4** (2022) 61.

[75] J. Xiao, Y. Wang, H. Wang, C.D. Pemmaraju, S. Wang, P. Muscher et al., *Berry curvature memory through electrically driven stacking transitions*, *Nature Physics* **16** (2020) 1028.

[76] D.A. Rehn, Y. Li, E. Pop and E.J. Reed, *Theoretical potential for low energy consumption phase change memory utilizing electrostatically-induced structural phase transitions in 2d materials*, *npj Computational Materials* **4** (2018) 2.

[77] X. Qian, J. Liu, L. Fu and J. Li, *Quantum spin hall effect in two-dimensional transition metal dichalcogenides*, *Science* **346** (2014) 1344.

[78] W. Li, X. Qian and J. Li, *Phase transitions in 2d materials*, *Nature Reviews Materials* **6** (2021) 829.

[79] S. Lara-Avila, A. Tzalenchuk, S. Kubatkin, R. Yakimova, T.J.B.M. Janssen, K. Cedergren et al., *Disordered fermi liquid in epitaxial graphene from quantum transport measurements*, *Phys. Rev. Lett.* **107** (2011) 166602.

[80] F. Fallah and M. Esmaeilzadeh, *Energy levels of exciton in a gapped graphene sheet*, *Journal of Applied Physics* **114** (2013) 073702.

[81] O. Warschkow, N.J. Curson, S.R. Schofield, N.A. Marks, H.F. Wilson, M.W. Radny et al., *Reaction paths of phosphine dissociation on silicon (001)*, *The Journal of Chemical Physics* **144** (2016) 014705.

[82] T.J.Z. Stock, O. Warschkow, P.C. Constantinou, J. Li, S. Fearn, E. Crane et al., *Atomic-scale patterning of arsenic in silicon by scanning tunneling microscopy*, *ACS Nano* **14** (2020) 3316.

[83] J.G. Keizer, S. Koelling, P.M. Koenraad and M.Y. Simmons, *Suppressing segregation in highly phosphorus doped silicon monolayers*, *ACS Nano* **9** (2015) 12537.

[84] M.M. Fuechsle, *Precision few-electron silicon quantum dots*, Ph.D. thesis, UNSW Sydney, 2011.

[85] J. Li, N.H. Le, K.L. Litvinenko, S.K. Clowes, H. Engelkamp, S.G. Pavlov et al., *Radii of rydberg states of isolated silicon donors*, *Phys. Rev. B* **98** (2018) 085423.

[86] E.H. Hwang and S. Das Sarma, *Electronic transport in two-dimensional si:p δ-doped layers*, *Phys. Rev. B* **87** (2013) 125411.

[87] J.A. Hagmann, X. Wang, R. Kashid, P. Namboodiri, J. Wyrick, S.W. Schmucker et al., *Electron-electron interactions in low-dimensional si:p delta layers*, *Phys. Rev. B* **101** (2020) 245419.

[88] G. Scappucci, W.M. Klesse, L.A. Yeoh, D.J. Carter, O. Warschkow, N.A. Marks et al., *Bottom-up assembly of metallic germanium*, *Scientific Reports* **5** (2015) 12948.

[89] I.L. Aleiner, B.L. Altshuler and M.E. Gershenson, *Interaction effects and phase relaxation in disordered systems*, *Waves in Random Media* **9** (1999) 201.

[90] G.M. Minkov, A.V. Germanenko, O.E. Rut, A.A. Sherstobitov and B.N. Zvonkov, *Giant suppression of the drude conductivity due to quantum interference in the disordered two-dimensional systemgaas/inxga1-xas/gaas*, *Physical Review B* **75** (2007) .

[91] S. Shamim, S. Mahapatra, G. Scappucci, W.M. Klesse, M.Y. Simmons and A. Ghosh, *Dephasing rates for weak localization and universal conductance fluctuations in two dimensional Si:P and Ge:P δ-layers*, *Scientific Reports* **7** (2017) 46670.

[92] B.E. Kane, *A silicon-based nuclear spin quantum computer*, *Nature* **393** (1998) 133 .

[93] S.R. Schofield, N.J. Curson, M.Y. Simmons, F.J. Rueß, T. Hallam, L. Oberbeck et al., *Atomically precise placement of single dopants in* Si, *Phys. Rev. Lett.* **91** (2003) 136104.

[94] S.R. McKibbin, C.M. Polley, G. Scappucci, J.G. Keizer and M.Y. Simmons, *Low resistivity, super-saturation phosphorus-in-silicon monolayer doping*, *Applied Physics Letters* **104** (2014) 123502.

[95] B. Weber, S. Mahapatra, H. Ryu, S. Lee, A. Fuhrer, T.C.G. Reusch et al., *Ohm's law survives to the atomic scale*, *Science* **335** (2012) 64.

[96] M. Fuechsle, J.A. Miwa, S. Mahapatra, H. Ryu, S. Lee, O. Warschkow et al., *A single-atom transistor*, *Nature Nanotechnology* **7** (2012) 242.

[97] S. Asaad, V. Mourik, B. Joecker, M.A.I. Johnson, A.D. Baczewski, H.R. Firgau et al., *Coherent electrical control of a single high-spin nucleus in silicon*, *Nature* **579** (2020) 205.

[98] Y. He, S.K. Gorman, D. Keith, L. Kranz, J.G. Keizer and M.Y. Simmons, *A two-qubit gate between phosphorus donor electrons in silicon*, *Nature* **571** (2019) 371.

[99] B. Koiller, X. Hu and S. Das Sarma, *Exchange in silicon-based quantum computer architecture*, *Phys. Rev. Lett.* **88** (2001) 027903.

[100] G. Pica and B.W. Lovett, *Quantum gates with donors in germanium*, *Phys. Rev. B* **94** (2016) 205309.

[101] J.A. Ivie, Q. Campbell, J.C. Koepke, M.I. Brickson, P.A. Schultz, R.P. Muller et al., *Impact of incorporation kinetics on device fabrication with atomic precision*, *Phys. Rev. Applied* **16** (2021) 054037.

[102] S. Solmi and D. Nobili, *High concentration diffusivity and clustering of arsenic and phosphorus in silicon*, *Journal of Applied Physics* **83** (1998) 2484.

[103] J.C. Slater, *Atomic radii in crystals*, *The Journal of Chemical Physics* **41** (1964) 3199.

[104] J.A. Stroscio and D.M. Eigler, *Atomic and molecular manipulation with the scanning tunneling microscope*, *Science* **254** (1991) 1319.

[105] M.F. Crommie, C.P. Lutz and D.M. Eigler, *Confinement of electrons to quantum corrals on a metal surface*, *Science* **262** (1993) 218.

[106] F.J. Ruess, L. Oberbeck, M.Y. Simmons, K.E.J. Goh, A.R. Hamilton, T. Hallam et al., *Toward atomic-scale device fabrication in silicon using scanning probe microscopy*, *Nano Letters* **4** (2004) 1969.

[107] M. Fuechsle, J.A. Miwa, S. Mahapatra, H. Ryu, S. Lee, O. Warschkow et al., *Single-atom transistor*, *Nature Nanotechnology* **7** (2012) 242.

[108] W. Jeong, S. Maeda, H. Lee, K. Lee, T. Lee, D. Park et al., *True 7nm platform technology featuring smallest finfet and smallest sram cell by euv, special constructs and 3rd generation single diffusion break* in *2018 IEEE Symposium on VLSI Technology*, pp. 59–60, 2018.

[109] A.S. Chang and L.J. Lauhon, *Atom probe tomography of nanoscale architectures in functional materials for electronic and photonic applications*, *Current Opinion in Solid State and Materials Science* **22** (2018) 171.

[110] H. Werner and P. Boudewijn, *A comparison of* SIMS *with other techniques based on ion-beam solid interactions*, *Vacuum* **34** (1984) 83.

[111] T.U. Schülli and S.J. Leake, *X-ray nanobeam diffraction imaging of materials*, *Current Opinion in Solid State and Materials Science* **22** (2018) 188.

[112] G. Gramse, A. Kölker, T. Škereň, T.J.Z. Stock, G. Aeppli, F. Kienberger et al., *Nanoscale imaging of mobile carriers and trapped charges in delta doped silicon p-n junctions*, *Nature Electronics* **3** (2020) 531.

[113] M. Holler, M. Guizar-Sicairos, E.H.R. Tsai, R. Dinapoli, E. Müller, O. Bunk et al., *High-resolution non-destructive three-dimensional imaging of integrated circuits*, *Nature* **543** (2017) 402.

[114] M.D. de Jonge, C. Holzner, S.B. Baines, B.S. Twining, K. Ignatyev, J. Diaz et al., *Quantitative* 3D *elemental microtomography of* Cyclotella *meneghiniana at 400-nm resolution*, *Proceedings of the National Academy of Sciences* **107** (2010) 15676.

[115] X.-L. Zhou and S.-H. Chen, *Theoretical foundation of x-ray and neutron reflectometry*, *Physics Reports* **257** (1995) 223.

[116] L.G. Parratt, *Surface studies of solids by total reflection of x-rays*, *Phys. Rev.* **95** (1954) 359.

[117] *X-ray and neutron reflectivity*, *Zeitschrift für Kristallographie - Crystalline Materials* **213** (1998) 319.

[118] B. Henke, E. Gullikson and J. Davis, *X-ray interactions: Photoabsorption, scattering, transmission, and reflection at e = 50-30,000 ev, z = 1-92*, *Atomic Data and Nuclear Data Tables* **54** (1993) 181.

[119] M. Björck and G. Andersson, *GenX: an extensible X-ray reflectivity refinement program utilizing differential evolution*, *Journal of Applied Crystallography* **40** (2007) 1174.

[120] M. Elzo, E. Jal, O. Bunau, S. Grenier, Y. Joly, A. Ramos et al., *X-ray resonant magnetic reflectivity of stratified magnetic structures: Eigenwave formalism and application to a w/fe/w trilayer*, *Journal of Magnetism and Magnetic Materials* **324** (2012) 105.

[121] U. Flechsig, F. Nolting, A. Fraile Rodríguez, J. Krempaský, C. Quitmann, T. Schmidt et al., *Performance measurements at the sls sim beamline*, *AIP Conference Proceedings* **1234** (2010) 319.

[122] U. Staub, V. Scagnoli, Y. Bodenthin, M. García-Fernández, R. Wetter, A.M. Mulders et al., *Polarization analysis in soft X-ray diffraction to study magnetic and orbital ordering*, *Journal of Synchrotron Radiation* **15** (2008) 469.

[123] L. Nevot and P. Croce, *Characterization of surfaces by grazing x-ray reflection–application to the study of polishing of some silicate glasses*, *Revue de Physique Applique* **15** (1980) 761.

[124] E. Gullikson, "Multilayer reflectivity."

[125] H.-C. Su, C.-H. Lee, M.-Z. Lin and T.-W. Huang, *A comparison between x-ray reflectivity and atomic force microscopy on the characterization of a surface roughness*, *Chinese Journal of Physics* **50** (2012) 291.

[126] J.M. Freitag and B.M. Clemens, *Nonspecular x-ray reflectivity study of roughness scaling in si/mo multilayers*, *Journal of Applied Physics* **89** (2001) 1101.

[127] O. Durand and N. Morizet, *Fourier-inversion and wavelet-transform methods applied to x-ray reflectometry and hrxrd profiles from complex thin-layered heterostructures*, *Applied Surface Science* **253** (2006) 133.

[128] S. Olhede and A. Walden, *Generalized morse wavelets*, *IEEE Transactions on Signal Processing* **50** (2002) 2661.

[129] Y. Homma, H. Takenaka, F. Toujou, A. Takano, S. Hayashi and R. Shimizu, *Evaluation of the sputtering rate variation in sims ultra-shallow depth profiling using multiple short-period delta layers*, *Surface and Interface Analysis* **35** (2003) 544.

[130] F. Villar, L. Andre, R. Baker, S. Bohic, J.C. da Silva, C. Guilloud et al., *Nanopositioning for the* ESRF ID16A *nano-imaging beamline*, *Synchrotron Radiation News* **31** (2018) 9.

[131] F.A. Zwanenburg, A.S. Dzurak, A. Morello, M.Y. Simmons, L.C.L. Hollenberg, G. Klimeck et al., *Silicon quantum electronics*, *Rev. Mod. Phys.* **85** (2013) 961.

[132] N.G. Orji, M. Badaroglu, B.M. Barnes, C. Beitia, B.D. Bunday, U. Celano et al., *Metrology for the next generation of semiconductor devices*, *Nature Electronics* **1** (2018) 532.

[133] M. Holler, M. Odstrcil, M. Guizar-Sicairos, M. Lebugle, E. Müller, S. Finizio et al., *Three-dimensional imaging of integrated circuits with macro- to nanoscale zoom*, *Nature Electronics* **2** (2019) 464.

[134] K.J. Dwyer, S. Baek, A. Farzaneh, M. Dreyer, J.R. Williams and R.E. Butera, *B-doped δ-layers and nanowires from area-selective deposition of* BCl_3 *on* Si(100), *ACS Applied Materials & Interfaces* **13** (2021) 41275.

[135] K.E.J. Goh, L. Oberbeck, M.Y. Simmons, A.R. Hamilton and M.J. Butcher, *Influence of doping density on electronic transport in degenerate* Si : P *δ-doped layers*, *Phys. Rev. B* **73** (2006) 035401.

[136] M. Koch, J.G. Keizer, P. Pakkiam, D. Keith, M.G. House, E. Peretz et al., *Spin read-out in atomic qubits in an all-epitaxial three-dimensional transistor*, *Nature Nanotechnology* **14** (2019) 137.

[137] H. Büch, M. Fuechsle, W. Baker, M.G. House and M.Y. Simmons, *Quantum dot spectroscopy using a single phosphorus donor*, *Phys. Rev. B* **92** (2015) 235309.

[138] V. Brázdová, D.R. Bowler, K. Sinthiptharakoon, P. Studer, A. Rahnejat, N.J. Curson et al., *Exact location of dopants below the* Si(001) : H *surface from scanning tunneling microscopy and density functional theory*, *Phys. Rev. B* **95** (2017) 075408.

[139] B. Voisin, J. Salfi, R. Rahman and S. Rogge, *Novel characterization of dopant-based qubits*, *MRS Bulletin* **46** (2021) 616.

[140] E. Zschech and A. Diebold, *Metrology and failure analysis for* 3D IC *integration*, *AIP Conference Proceedings* **1395** (2011) 233.

[141] A.M. Katzenmeyer, T.S. Luk, E. Bussmann, S. Young, E.M. Anderson, M.T. Marshall et al., *Assessing atomically thin delta-doping of silicon using mid-infrared ellipsometry*, *Journal of Materials Research* **35** (2020) 2098.

[142] F. Adams, B. Vekemans, G. Silversmit, B. De Samber and L. Vincze, *Microscopic X-ray fluorescence analysis with synchrotron radiation sources* in *Handbook of Nuclear Chemistry*, pp. 1737–1759 (2011).

[143] D. Grolimund, A. Scheidegger, J. van der Veen and R. Abela, *Layout of the* MicroXAS *beamline at* SLS, *PSI Scientific Report* **4** (2002) 139.

[144] V. Solé, E. Papillon, M. Cotte, P. Walter and J. Susini, *A multiplatform code for the analysis of energy-dispersive X-ray fluorescence spectra*, *Spectrochimica Acta Part B: Atomic Spectroscopy* **62** (2007) 63.

[145] "`http://www.nanoxrf.com/?page_id=106`."

[146] F. Döring, A. Robisch, C. Eberl, M. Osterhoff, A. Ruhlandt, T. Liese et al., *Sub-5 nm hard x-ray point focusing by a combined Kirkpatrick-Baez mirror and multilayer zone plate*, *Opt. Express* **21** (2013) 19311.

[147] J. Park, Y. Ahn, J.A. Tilka, K.C. Sampson, D.E. Savage, J.R. Prance et al., *Electrode-stress-induced nanoscale disorder in* Si *quantum electronic devices*, *APL Materials* **4** (2016) 066102.

[148] A. Troian, G. Otnes, X. Zeng, L. Chayanun, V. Dagytė, S. Hammarberg et al., *Nanobeam X-ray fluorescence dopant mapping reveals dynamics of in situ* Zn*-doping in nanowires*, *Nano Letters* **18** (2018) 6461.

[149] P.A. Lee and T.V. Ramakrishnan, *Disordered electronic systems*, *Rev. Mod. Phys.* **57** (1985) 287.

[150] P.M. Mensz and R.G. Wheeler, *Magnetoconductance due to parallel magnetic fields in silicon inversion layers*, *Phys. Rev. B* **35** (1987) 2844.

[151] D.F. Sullivan, B.E. Kane and P.E. Thompson, *Weak localization thickness measurements of* Si : P *delta-layers*, *Applied Physics Letters* **85** (2004) 6362.

[152] M. Odstrcil, M. Holler, J. Raabe, A. Sepe, X. Sheng, S. Vignolini et al., *Ab initio nonrigid x-ray nanotomography*, *Nature Communications* **10** (2019) 2600.

[153] J. Deng, Y. Yao, Y. Jiang, S. Chen, T.M. Mooney, J.A. Klug et al., *High-resolution ptychographic imaging enabled by high-speed multi-pass scanning*, *Opt. Express* **30** (2022) 26027.

[154] X. Wang, J. Wyrick, R.V. Kashid, P. Namboodiri, S.W. Schmucker, A. Murphy et al., *Atomic-scale control of tunneling in donor-based devices*, *Communications Physics* **3** (2020) 82.

[155] P.C. Constantinou, *Fabrication and characterization of metallic, two-dimensional dopant δ-layers in silicon*, Ph.D. thesis, UCL (University College London), 2021.

[156] V. Strocov, *Photoemission response of 2d electron states*, *Journal of Electron Spectroscopy and Related Phenomena* **229** (2018) 100.

[157] M.E. Cage, K. Klitzing, A. Chang, F. Duncan, M. Haldane, R.B. Laughlin et al., *The quantum Hall effect*, Springer Science & Business Media (2012).

[158] M. König, S. Wiedmann, C. Brüne, A. Roth, H. Buhmann, L.W. Molenkamp et al., *Quantum spin Hall insulator state in HgTe quantum wells*, *Science* **318** (2007) 766.

[159] W.P. Kirk, J.N. Randall and J.H. Owen, *2d Quantum Metamaterials: Proceedings Of The 2018 Nist Workshop-2018 Nist Workshop*, World Scientific (2019).

[160] K. Lai, W. Pan, D.C. Tsui and Y.-H. Xie, *Observation of the apparent metal-insulator transition of high-mobility two-dimensional electron system in a Si/Si1-xGex heterostructure*, *Applied Physics Letters* **84** (2004) 302.

[161] E.F. Schubert, *Delta-doping of semiconductors*.

[162] W. Knap, C. Skierbiszewski, A. Zduniak, E. Litwin-Staszewska, D. Bertho, F. Kobbi et al., *Weak antilocalization and spin precession in quantum wells*, *Phys. Rev. B* **53** (1996) 3912.

[163] T.F. Rosenbaum, R.F. Milligan, G.A. Thomas, P.A. Lee, T.V. Ramakrishnan, R.N. Bhatt et al., *Low-temperature magnetoresistance of a disordered metal*, *Phys. Rev. Lett.* **47** (1981) 1758.

[164] J.A. Hagmann, X. Wang, P. Namboodiri, J. Wyrick, R. Murray, M.D. Stewart et al., *High resolution thickness measurements of ultrathin si:p monolayers using weak localization*, *Applied Physics Letters* **112** (2018) 043102.

[165] S. Das Sarma, M.P. Lilly, E.H. Hwang, L.N. Pfeiffer, K.W. West and J.L. Reno, *Two-dimensional metal-insulator transition as a percolation transition in a high-mobility electron system*, *Phys. Rev. Lett.* **94** (2005) 136401.

[166] Y. Meir, *Percolation-type description of the metal-insulator transition in two dimensions*, *Phys. Rev. Lett.* **83** (1999) 3506.

[167] A.V. Germanenko, G.M. Minkov and O.E. Rut, *Weak localization in macroscopically inhomogeneous two-dimensional systems: a simulation approach*, *Phys. Rev. B* **64** (2001) 165404.

[168] M.M. Parish and P.B. Littlewood, *Non-saturating magnetoresistance in heavily disordered semiconductors*, *Nature* **426** (2003) 162.

[169] M.M. Parish and P.B. Littlewood, *Classical magnetotransport of inhomogeneous conductors*, *Phys. Rev. B* **72** (2005) 094417.

[170] K.V. Kavokin, *Anisotropic exchange interaction of localized conduction-band electrons in semiconductors*, *Phys. Rev. B* **64** (2001) 075305.

[171] S. Wolgast, i.m.c.b.u.i.e.i.f. Kurdak, K. Sun, J.W. Allen, D.-J. Kim and Z. Fisk, *Low-temperature surface conduction in the kondo insulator* smb_6, *Phys. Rev. B* **88** (2013) 180405.

[172] Y. Nakajima, P. Syers, X. Wang, R. Wang and J. Paglione, *One-dimensional edge state transport in a topological kondo insulator*, *Nature Physics* **12** (2016) 213.

[173] K.E.J. Goh, L. Oberbeck and M.Y. Simmons, *Relevance of phosphorus incorporation and hydrogen removal for* Si : P *δ-doped layers fabricated using phosphine*, *physica status solidi (a)* **202** (2005) 1002.